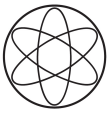

Technische Universität München

TECHNISCHE UNIVERSITÄT MÜNCHEN
Max-Planck-Institut für Extraterrestrische Physik
Garching bei München

High-energy transients with *Fermi*/GBM

David Gruber

Vollständiger Abdruck der von der Fakultät für Physik der Technischen Universität München zur Erlangung des akademischen Grades eines

Doktors der Naturwissenschaften (Dr. rer. nat.)

genehmigten Dissertation.

Vorsitzender:		Univ.-Prof. Dr. Alejandro Ibarra
Prüfer der Dissertation:	1.	Priv.-Doz. Dr. Jochen Greiner
	2.	Univ.-Prof. Dr. Elisa Resconi

Die Dissertation wurde am 31.08.2012 bei der Technischen Universität München eingereicht und durch die Fakultät für Physik am 09.10.2012 angenommen.

Abstract

For most of mankind's history, astronomy was performed on-ground in the optical energy range. It was only when space-based missions, built more than 50 years ago, detected photons with mind-boggling energies that the exploration of the violent Universe really began. These γ-ray photons still provide us with an unprecedented wealth of information for the most energetic processes taking place in the cosmos. Faithful to the olympic slogan "higher, faster, further", an increasing armada of γ-ray satellites was built and launched over the last couple of decades with *Fermi* being the youngest of its kind.

In this thesis, I use data from the Gamma-Ray Burst Monitor (GBM) onboard the *Fermi* satellite. The focus of this work lies on three very different classes of high-energy astrophysical transients: Gamma-Ray Bursts (GRBs), solar flares and Soft Gamma Repeaters (SGRs).

In Chapter 2, I present GRB 091024A, a burst of very long duration in γ-rays where optical data could be acquired well during its active phase. The optical light curve shows very intriguing features which I subsequently interpret as the so called "optical flash", a fundamental property of the "fireball" model. Although predicted by the latter model, only a handful of GRBs show such a behavior, making them interesting transients to study. Furthermore, I present the fundamental temporal and spectral properties of 47 GBM-detected GRBs with known redshifts. As GRBs explode at cosmological distances it is of uttermost importance to study them in their rest-frame to get a better understanding of their emission mechanisms. I confirm several correlations already found in the past together with an intriguing connection between redshift and the peak energy ($E_{\rm peak}$) of GRBs. Although this correlation is heavily influenced by instrumental effects, it is not unexpected from other experimental results, giving it more credibility. Finally, I present the results of the search for untriggered GRBs in GBM data. This project focuses on GRBs which triggered *Swift* but not GBM although the GRBs came from positions above the horizon, with a favorable orientation to at least one GBM detector. The properties of these GRBs are then compared to the full sample of GBM GRBs published in the GBM spectral catalogue.

Although designed mainly for GRB studies, GBM observes solar flares as well. In Chapter 3, I made use of the high temporal quality of GBM data to perform a detailed timing analysis of four solar flares. Contrary to recent claims in the literature, where quasi periodic pulsations (QPPs) have been allegedly identified in the γ-ray data of solar flares, I did not find any statistical significant signatures of such QPPs. When red-noise, an intrinsic source component, is accounted for, most of the claimed QPPs fall below the threshold of a significant detection. Moreover, I developed a new background estimation method for solar flares, called SOBER^2 (SOlar Background Employing Relative Rates). This method uses the count rate of the complementary and shaded BGO detector as an *a priori* information to determine the background fluctuations for the Sun-facing BGO detector. Such a method is especially useful and beneficial for solar flares because they are usually of very long duration and the standard GBM background subtraction fails in such cases.

Finally, in Chapter 4, I present the log-parabolic model which I used to fit the spectra of SGR bursts. Even though the spectra of the latter are usually and preferentially fit by a sum of two blackbodies in the literature, I will show that the log-parabolic model fits the data as least as well as the double blackbody function. Additionally, the log-parabolic model is based on a strong underlying physical mechanism, i.e. second order Fermi acceleration, which gives it even more credibility.

Zusammenfassung

Für den Großteil der menschlichen Geschichte wurde Astronomie nur bodengebunden im optischen Wellenlängenbereich betrieben. Erst als Raumsonden vor 50 Jahren Photonen mit unglaublich hohen Energien detektiert haben, hat die Erforschung des "heftigen Universums" Fahrt aufgenommen. Selbst heute noch geben uns diese Gammastrahlen eine beispiellose Fülle an Informationen über die energiereichsten Prozesse im Kosmos. Getreu dem olympischen Motto "höher, schneller, weiter", wurde in den letzten Jahrzehnten eine stetig wachsende Armada an Gamma-Satelliten gebaut und gestartet, wobei *Fermi* den Jüngsten seiner Art darstellt.

In dieser Arbeit benutze ich Beobachtungsdaten des Gamma-Ray Burst Monitors (GBM), an Bord des *Fermi* Satelliten. Der Schwerpunkt dieser Arbeit liegt auf drei sehr unterschiedlichen Kategorien hochenergetischer, astrophysikalischer Phänomene: Gammablitze (GRBs), Sonneneruptionen und schwache Gammawiederholer (SGRs).

In Kapitel 2 stelle ich GRB 091024A vor, einen Gammablitz von so langer Lebensdauer, dass optische Daten noch während seiner aktiven Phase akkumuliert werden konnten. Die optische Lichtkurve zeigt ein Profil, welches ich als "optischen Blitz" interpretiere, eine fundamentale Eigenschaft des "Feuerball" Models. Obwohl von diesem Modell grundsätzlich vorhergesagt, zeigen nur eine Handvoll GRBs solch ein Verhalten. Darüber hinaus stelle ich die grundlegenden zeitlichen und spektralen Eigenschaften von 47 GBM-detektierten GRBs mit bekannter Rotverschiebung vor. Da GRBs in kosmologischen Entfernungen explodieren, ist es von größter Wichtigkeit, die physikalischen Parameter in ihrem Ruhesystem zu studieren, um ein besseres Verständnis über ihre Emissionsmechanismen zu bekommen. Ich konnte viele der zuvor gefundenen Korrelationen der Ruhesystemeigenschaften bestätigen und habe einen interessanten Zusammenhang zwischen der Rotverschiebung und der Peak-Energie ($E_{\rm peak}$) gefunden. Obwohl diese Korrelation stark von instrumentellen Effekten beeinflusst ist, verleihen ihr andere experimentellen Beobachtungen mehr Glaubwürdigkeit. Schließlich präsentiere ich die Ergebnisse der Suche nach ungetriggerten Gammablitzen in den GBM Daten. Dieses Projekt legte den Schwerpunkt auf die Suche nach GRBs die zwar *Swift*, aber nicht GBM getriggert haben, obwohl sie nicht von der Erde abgeschattet waren und mindestens ein Detektor eine günstige Orientierung zu ihnen hatte. Die Eigenschaften dieser letztgenannten Gammablitze wurden dann mit dem Eigenschaften aller Gammablitze des spektralen Katalogs verglichen.

Obwohl GBM hauptsächlich zur Untersuchung für GRBs konzipiert wurde, kann GBM auch Sonneneruptionen beobachten. In Kapitel 3 führe ich eine detaillierte Zeitreihen-Analyse von 4 Sonneneruptionen durch. Entgegen einiger Arbeiten in der Literatur, die behaupten quasiperiodische Pulsationen (QPPs) in den γ-Lichtkurven von Sonneneruptionen gefunden zu haben, konnte ich keinerlei statistisch signifikante QPPs finden. Sobald die intrinsische Quellkomponente, das "rotes Rauschen", berücksichtigt wird, fallen alle vielversprechenden QPPs unterhalb jener Schwelle, ab welcher eine statistisch signifikanten Detektion vorliegt. Zusätzlich habe ich ein neues Verfahren entwickelt, um die Hintergrundzählrate für Sonneneruption besser abzuschätzen. Die SOBER^2 (SOlar Background Employing Relative Rates) Methode verwendet die Zählrate des komplementären, von der Quelle abgeschatteten, BGO Detektors als eine *a priori* Information, um die Hintergrundzählrate für den zur Sonne zugewandten Detektor zu bestimmen. Ein derartiges Verfahren ist gerade für sehr lange Sonneneruptionen sinnvoll, da die Standard-Hintergrundmethode in solchen Fällen versagt.

Abschließend präsentiere ich in Kapitel 4 das so genannte Log-Parabel-Modell, welches ich verwendet habe, um die Spektren von SGR Explosionen anzupassen. Auch wenn solche Spek-

tren in der Literatur vorzugsweise durch eine Summe von zwei Schwarzkörperstrahlern gefittet werden, konnte ich zeigen, dass das Log-Parabel-Modell die GBM Daten mindestens ebenso gut wie die Schwarzkörperfunktion fittet. Da das Log-Parabel-Modell auf einen physikalischen Mechanismus (Fermi-Beschleunigung zweiter Ordnung) basiert, verleiht es dem Modell zusätzlich Glaubwürdigkeit.

Contents

Chapter 1

Introduction

1.1 γ-ray Astrophysics

Throughout most of human history, our knowledge of the Universe has been restricted to the optical regime of the electromagnetic spectrum. Even though this energy band is relatively small, many ground-breaking discoveries were obtained in the optical. But as soon as we began to broaden our energy window to both lower and higher energy ranges in the mid 1950's, our knowledge and understanding of the Universe increased by many orders of magnitude. Many more, previously unknown, astrophysical phenomena were revealed. For example, radio observations allowed us to measure the cosmic microwave background and studies in the infrared revealed the nature of the dust particles and molecules in and beyond our own Galaxy.

The last energy window to be opened were the γ-rays, lifting the curtain for the "violent Universe" (see Fig. 1.1). Several scientists predicted the existence of high-energy photons even before the first measurements in this regime were obtained in the early 1960's by high-altitude balloons and spacecraft experiments such as the third Orbiting Solar Observatory (OSO-3) and the Vela satellites. The Crab pulsar was brought to light and diffuse γ-ray radiation arising from the central region of the Milky Way was observed (Kniffen and Fichtel, 1970; Browning et al., 1971; Kraushaar et al., 1972). These early experiments were quickly followed by the Cosmic-Ray Satellite (COS-B) and the Small Astronomy Satellite (SAS-2) in the mid 1970's which refined and explored the aforementioned discoveries even further.

However, it was not until April 1991 when the "Compton Gamma-Ray Observatory" (CGRO) was launched when our understanding about the high-energy Universe, quite literally, exploded. For the first time an all sky survey at high energies was available, including ~ 300 new sources. The "Burst and Transient Explorer" BATSE instrument onboard CGRO alone discovered over 2700 Gamma-Ray Bursts (GRBs Meegan et al., 1992), Soft Gamma Repeaters (SGRs Kouveliotou et al., 1998), solar flares (Schwartz et al., 1992) and Terrestrial Gamma-Ray Flashes (TGF Fishman et al., 1994). CGRO was de-orbited in June 2003, but even before that, in 1996, the BeppoSAX (Boella et al., 1997) mission started observing the γ-ray sky. The High-Energy Transient Explorer (HETE-2, see Barraud et al., 2003, and references therein), launched in 2000 (working until 2007) and the *Swift* satellite (Gehrels et al., 2004), launched in 2004 and still operational, followed and continued observations.

Together with *Swift*, there are currently three additional high-energy γ-ray satellites operational in space, i.e. the "INTErnational Gamma-Ray Astrophysics Laboratory" (INTEGRAL, Winkler et al., 2003), the "Astrorivelatore Gamma a Immagini LEggero" (AGILE, Tavani et al., 2008) and *Fermi* (Atwood et al., 2009). The science return of the latter, especially its secondary

instrument, will be the main focus of this thesis.

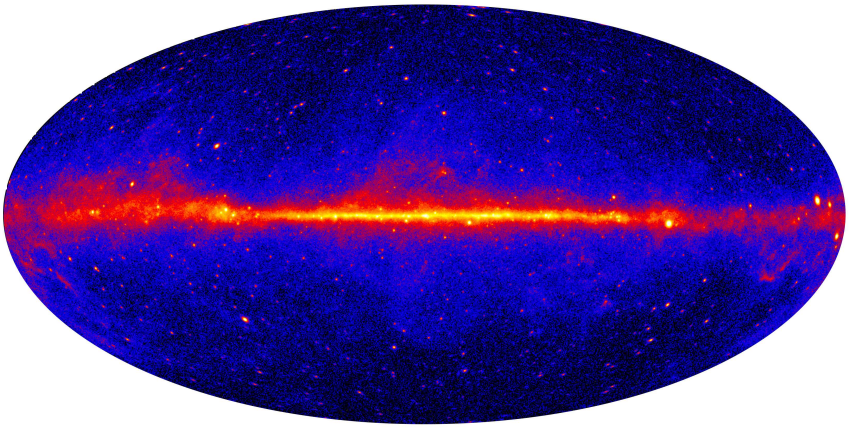

Figure 1.1 The γ-ray sky as seen by *Fermi*. (Picture taken from `http://fermi.sonoma.edu/multimedia/gallery/3YearSkyMap.jpg`)

1.2 The *Fermi* observatory

The *Fermi*[a] satellite (see Fig. 1.2) was launched on 2008 June 11 into a 565 km low Earth orbit (LEO). Its payload comprises two instruments, the Gamma-Ray Burst Monitor (Meegan et al., 2009, GBM) and the Large Area Telescope (Atwood et al., 2009, LAT,). The key scientific objects of *Fermi* and its two instruments are to

(i) explore the most extreme environments in the Universe,

(ii) look for signs and identify the composition of the elusive Dark Matter,

(iii) black hole accretion physics,

(iv) answer unresolved questions about solar flares, pulsars, cosmic-rays and other high-energy astrophysical phenomena and, last but not least,

(v) to study the most powerful explosions in the Universe, known as Gamma-Ray Bursts.

In this chapter, I will present the two main instruments onboard *Fermi*. The main focus will be on the GBM in §1.2.1 and a short overview will be given on the LAT in §1.2.2

1.2.1 The Gamma-Ray Burst Monitor[b]

The *Fermi*/GBM (see Fig. 1.3 and Fig. 1.4) is the secondary instrument on-board the *Fermi* satellite. The goal of GBM is to augment the science return from *Fermi* with its prime objective

[a] formerly known as the *Fermi Gamma-Ray Space Telescope* or GLAST

[b] This section uses information from the GBM instrument paper *The* Fermi *Gamma-Ray burst Monitor* published by Meegan et al. (2009) and from *The* Fermi *GBM Gamma-Ray Burst Catalog: The First Two Years* by Paciesas et al. (2012).

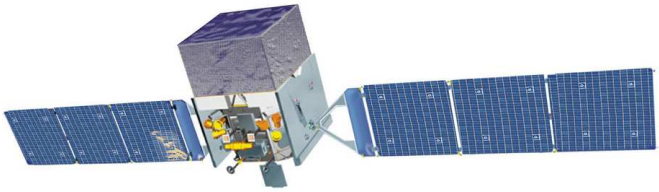

Figure 1.2 The *Fermi* satellite. (Picture taken from `http://www.nasa.gov`)

being joint spectral and timing analyses of GRBs. In addition, GBM provides near real-time burst locations which permit (i) the *Fermi* spacecraft to repoint the LAT towards the observed GRB and (ii) to communicate the position to ground-based observatories. Compared to other high-energy spacecrafts, the great advantage of GBM is its capability to observe the whole unocculted sky at any given time with a Field of View (FoV) of ≥ 8 sr and its very broad energy coverage from 8 keV to 40 MeV. Therefore, GBM offers great capabilities to observe all kinds of high-energy astrophysical phenomena, such as e.g. GRBs (e.g. Paciesas et al., 2012), solar flares (e.g. Gruber et al., 2011c; Ackermann et al., 2012), Soft Gamma Repeaters (SGRs, e.g. von Kienlin et al., 2012) and Terrestrial Gamma-Ray Flashes (TGFs, e.g. Briggs et al., 2011).

Hardware

In order to observe the γ-ray sky, GBM is composed of 12 thallium sodium iodide (NaI(Tl)) scintillation detectors which are sensitive from 8 keV to 1 MeV and 2 bismuth germanate (BGO) detectors (see Fig. 1.5), sensitive from 200 keV to 40 MeV. The NaI crystals have a thickness of 1.27 cm and a diameter of 12.7 cm. Their positions are oriented such that by measuring the relative counting rates in the detectors the position of the GRB can be determined (Fig. 1.4). The BGO crystal, on the other hand, has a diameter and thickness of 12.7 cm and the detectors are located on opposite sides of the spacecraft so that at least one is illuminated from any direction. The energy band of the BGOs overlaps both the NaI and LAT energy range at low and high energies, respectively. In this way a cross-calibration between the 3 different instruments is possible.

Triggering & Data products

GBM continuously observes the whole unocculted sky, with its flight software (FSW) constantly monitoring the count rates recorded in the various detectors. For GBM to trigger on a GRB or any other high-energy transient, two or more detectors must have a statistically significant increase in count rate above the background rate. GBM currently operates on 75 (of 119 supported) different trigger algorithms, each defined by its timescale (from 16 ms to 4 s), offset (value in ms by which the time binning is shifted) and energy range ($25-50$ keV, $50-300$ keV, >100 keV, and >300 keV). Additionally, each trigger algorithm can be operated on different threshold settings from 0.1σ to 25.5σ.

GBM persistently records two different types of science data, called CTIME (fine time resolution, coarse spectral resolution of 8 energy channels) and CSPEC (coarse time resolution, full spectral resolution of 128 energy channels). CTIME (CSPEC) data have a nominal time resolution of 0.256 s (4.096 s) (see Fig. 2.23 in §2.4) which is speeded up to 64 ms (1.024 s) whenever GBM triggers on an event (fore more details on GBM triggers see §2.4). After 600 s in triggered mode, both data types are returned to their non-triggered time resolution. The third

Figure 1.3 The Fermi Gamma-Ray Space Telescope being prepared for launch vehicle integration at Cape Canaveral. On top is the LAT with its reflective covering. Six of the GBM NaI detectors and one BGO detector can be seen on the side of the spacecraft. Photo credit: NASA/Kim Shiflett. Picture and caption taken from Meegan et al. (2009).

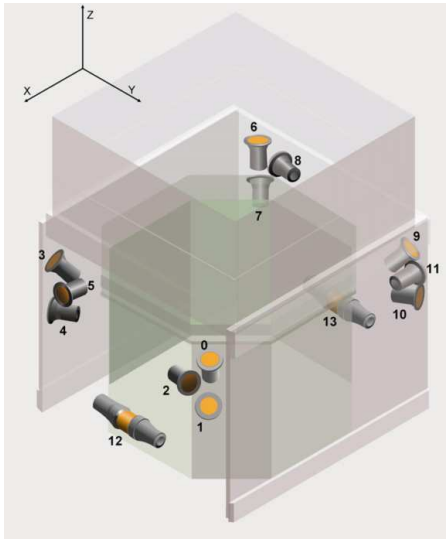

Figure 1.4 The Fermi Gamma-Ray Space Telescope being prepared for launch vehicle integration at Cape Canaveral. On top is the LAT with its reflective covering. Six of the GBM NaI detectors and one BGO detector can be seen on the side of the spacecraft. Photo credit: NASA/Kim Shiflett. Picture and caption taken from Meegan et al. (2009).

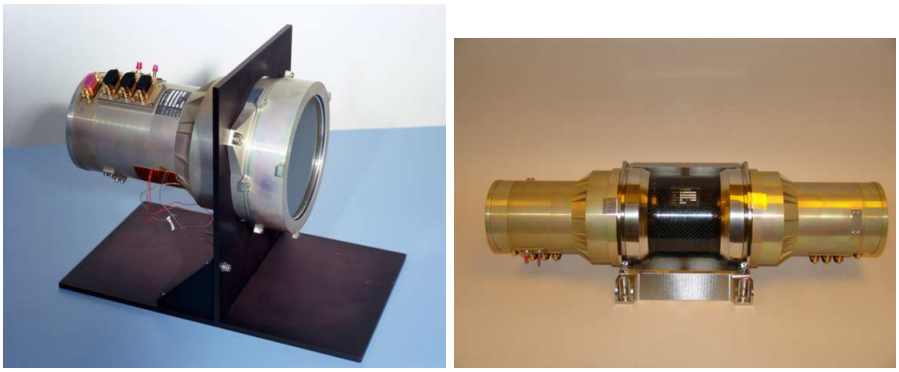

Figure 1.5 *Left panel:* NaI(Tl)-detector flight unit, consisting of a 12.7 cm by 1.27 cm NaI(Tl) crystal viewed by a PMT. *Right panel:* BGO detector, consisting a 12.7 cm diameter by 12.7 cm thick bismuth germanate crystal viewed by two PMTs.) Picture and caption taken from Meegan et al. (2009).

data type are the "Time Tagged Events" (TTE) which consist of individual events, each tagged with arrival time (2 μs resolution), energy (128 channels) and detector number. Un-triggered TTE data are stored for 25-30 s before they are deleted from the buffer. However, when GBM enters into trigger mode the production of TTE data lasts for approximately 300 s.

Temporal and spectral analyses of GBM data is done by using a trial source spectra which is then converted to predicted detector count histograms. The so generated histograms, in turn, are then compared to the actual, observed data. This process is called "forward-folding technique". In order to work properly, this method requires the so called detector response matrices (DRMs). DRMs contain information about the effective area of the detector, effects of the angular dependence of the detector efficiency, partial energy deposition in the detector, energy dispersion and nonlinearity of the detector and, finally, atmospheric and spacecraft scattering of photons into the detector. Therefore, DRMs are functions of photon energy, measured energy, the direction to the source (with respect to the spacecraft) and the orientation of the latter with respect to the Earth. A typical DRM is displayed in Fig. 1.6.

Since the effective area (i.e. detection efficiency) of the NaI detectors decreases rapidly for high incidence angles (Bissaldi et al., 2009) only detectors with source angles $\leq 60°$ are generally used for the temporal and spectral analysis. In addition, even though it is accounted for in the generation of the DRMs, it is checked that none of the included detectors used for the analyses were obstructed by neither the LAT instrument nor the solar panels (see Fig. 1.7).

Data analysis & Background estimation

While there are many advantages for a wide-field instrument such as GBM (i.e. observation of the whole unocculted sky at any time) compared to narrow-field instruments such as *Swift*, there exist also a few drawbacks: Arguably the major difficulty of GBM is obtaining accurate localizations of an event with the typical localization accuracy being in the order of a few degrees. While this limitation is a great concern especially for GRBs and SGRs (von Kienlin et al., 2012), as it makes on-ground follow-up observations difficult if not impossible, it is not a serious weakness for solar flares (this is, simply put, due to the fact that for the solar observer it suffices to know that the observed emission originated from the Sun). The second shortcoming of GBM is that it is relatively difficult to discern between source and background emission, especially if

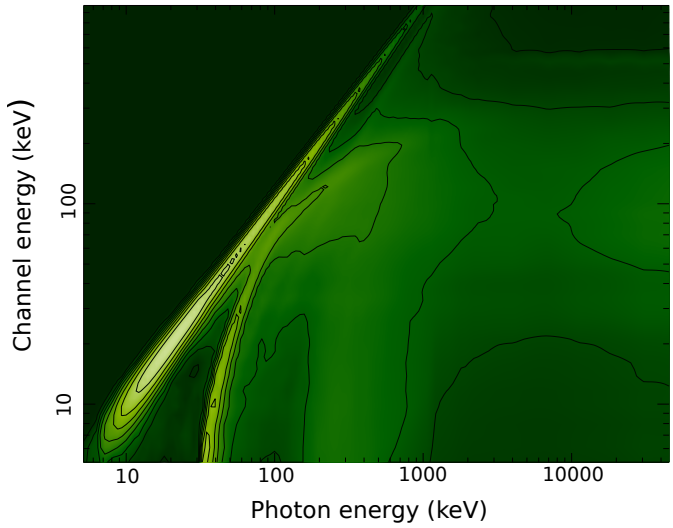

Figure 1.6 A typical CSPEC DRM. The y-axis shows the channel energy in keV whereas the x-axis shows the reconstructed energy. For most of the photons the reconstructed energy is indeed the same as the channel energy. However, there are some non-negligible deviations at low energies, especially at the NaI K-edge at 33.17 keV.

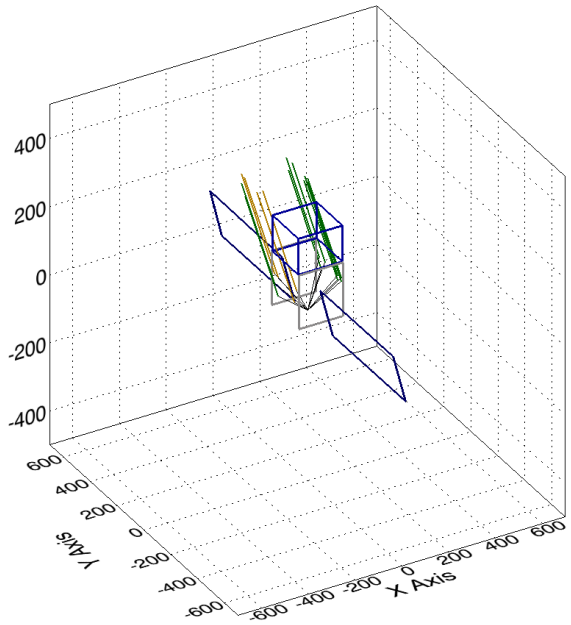

Figure 1.7 Detector source angles towards GRB 120426B. Green solid lines indicate an unhindered view towards the GRB, whereas orange solid lines indicate an obstruction of the GRB through either the solar panels or the LAT. (Figure generated by the `blocktest` routine created by V. Chaplin).

the observed event is either weak or if it is of very long duration. Being in a low Earth orbit the background variation changes dramatically due to the variations of the local particle flux densities. For bright, short events, or events which are well structured and easily distinguishable against the background variations (i.e. most of the GRBs observed by GBM) the background estimation is performed via selecting emission free intervals (*off* intervals) before and after the observed astrophysical event (*on* interval). This selection is then used to fit a polynomial up to 4th order in all energy channels independently. The background fit is then extrapolated across the *on* interval and the spectral fit is subsequently performed on the background subtracted source interval. However, for long events (lasting from 100 to more than 1000 s) a more detailed background analysis is required as the observer cannot know how the background varied during the prompt emission epoch of a long lasting solar flare.

One way to account for long events in the NaI and BGO detectors has been proposed by Fitzpatrick et al. (2011), labeled "Orbital Subtraction Method". In short, they use the background rate of adjacent days, when the satellite has the same geographical footprint. This happens every ± 15 orbits. However, due to the rocking mode observations of *Fermi*/LAT during sky survey, the NaI detectors have the same pointing only every ± 30 orbits. Using the detector rates of these adjacent ~ 2 days they show that this method can indeed be used to estimate the background at the time of interest for GRBs, solar flares and other astrophysical events. The major limitation of this method is that it cannot be used when *Fermi* issues an Autonomous Repoint Request (ARR) which consequently means that the pointing of the GBM detectors is interrupted. In addition, there are still some systematic differences in the background rates when comparing -30 to $+30$ orbits after the activation following an SAA passage of *Fermi*. For energetic solar flares, I present yet another method to estimate the background for the BGO detectors in § **??**.

1.2.2 The Large Area Telescope[c]

For the sake of completeness, the *Fermi* Large Area Telescope (LAT) is shown in this section as it is the primary instrument of *Fermi*. However, since the thesis presented here is heavily, if not solely, based on the science output by the GBM, the following will be only a sketchy overview of the capabilities and the principles of operation of the LAT. For a more detailed overview with an in-depth analysis of the main payload of *Fermi*, I refer to Atwood et al. (2009).

The LAT is, simply put, a pair-conversion telescope, i.e. it measures the track of electrons and positrons that are created when a γ-ray undergoes pair-conversion. The instrument consists of an array of 4×4 so called converter-tracker towers, each of which has several layers of high-Z tungsten foils where such a conversion can take place. The subsequent electromagnetic e^+e^- shower is then measured in the calorimeter which is installed below the trackers to obtain the energy of the incident γ-ray photon. The calorimeter consists of 96 CsI(Tl) crystals, arranged in 8 layers of 12 crystals each. Finally, the tracker towers are surrounded by an anti-coincidence detector (ACD) whose purpose is to reject charged background particles with a detection efficiency of at least 0.9997. The LAT is able to measure photon energies from 20 MeV to 300 GeV with an angular resolution of $0.15°$, $0.6°$ and $3.5°$ at > 10 GeV, 1 GeV and 100 MeV, respectively. Together with the GBM, the *Fermi* observatory covers over more than 7 decades in energy.

The LAT is a state-of-the-art, high-energy γ-ray space telescope: its great advantages are its big FoV (2.4 sr at 1 GeV), large effective area, angular and energy resolution, low dead time (26.5 μs) and its broad energy coverage.

[c]This section uses information from the LAT instrument paper *THE LARGE AREA TELESCOPE ON THE FERMI GAMMA-RAY SPACE TELESCOPE MISSION* published by Atwood et al. (2009).

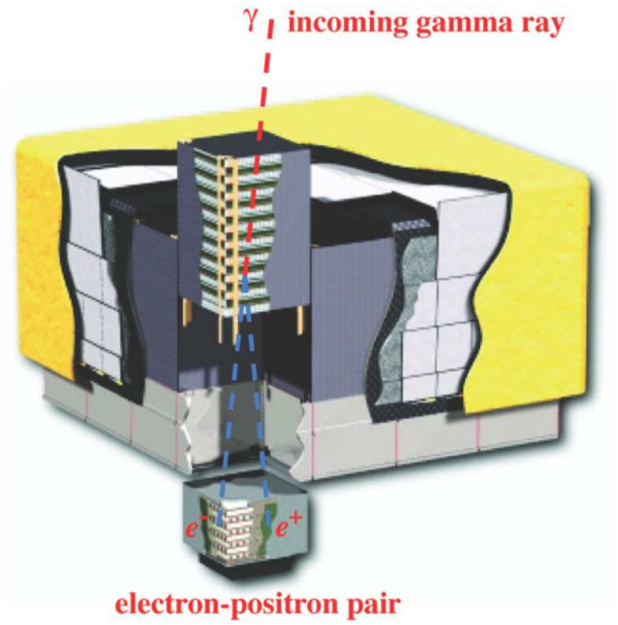

Figure 1.8 Schematic diagram of the LAT. The telescopes dimensions are 1.8 m × 1.8 m × 0.72 m. The power required and the mass are 650 W and 2789 kg, respectively. (Figure and caption taken from Atwood et al., 2009).

Chapter 2

Gamma-Ray Bursts

2.1 Introduction

GRBs were a serendipity discovery in the late 60s and early 70s (Klebesadel et al., 1973) when the data of the U.S. Vela satellites, checking for γ-ray pulses from forbidden nuclear weapon tests in space, recorded extraterrestrial, brief and intense bursts of γ-rays instead. It was soon found out that each GRB was slightly different from the others (see Fig. 2.1).

Even after the launch of the Burst and Transient Explorer (BATSE, Meegan et al., 1992) onboard the Compton Gamma-Ray Observatory (*CGRO*, 1991-2000) the origin and explosion site of these events remained a mystery, although it was discovered that GRBs were isotropically distributed across the Sky (see Fig. 2.2). Only when the BeppoSAX satellite was launched and ground-based follow-up observations identified the redshifts of these events (van Paradijs et al., 1997), it became clear that GRBs explode at cosmological distances. This discovery led to the conclusion that GRBs, with luminosities ranging from 10^{50} to 10^{54} erg s^{-1}, are the most luminous explosions in the Universe.

A large fraction of our knowledge of the prompt emission of GRBs comes from BATSE. One of its many findings is that the duration of GRBs covers more than 5 orders of magnitude. The duration of a GRB is measured as T_{90} which corresponds to the time in which 90% of the GRB's counts (or fluence) have been observed (Kouveliotou et al., 1993). A second important discovery was that GRBs are divided in (at least) two subgroups, labeled short and long GRBs with the cutoff being at a T_{90} of $\sim$ 2 s. These two groups differ from one another not only by their duration but also in their spectral hardness, with short GRBs being harder than long bursts. Although the inner engine of the GRB cannot be observed directly, this bimodal feature of GRBs leads to the conclusion that the two classes are created by two different progenitors. The current idea is that short GRBs arise due to a neutron - neutron star or neutron star - black hole merger (Goodman, 1986; Eichler et al., 1989; Meszaros and Rees, 1992, 1997), whereas long GRBs are powered by the collapse of a massive star into an accreting black hole (Meszaros and Rees, 1993; Medvedev and Loeb, 1999; MacFadyen and Woosley, 1999). This class-separation was subsequently confirmed by other instruments and holds up to this day (see Fig. 2.3).

Another important finding of BATSE was that the spectra of GRBs are non-thermal and can be modeled by a so called Band function (Band et al., 1993) which is a smoothly broken power law joined together at a break energy (see Fig. 2.4). This break in the νF_ν spectrum is defined as the peak energy, $E_{\rm peak}$, and is usually located at a few hundreds of keV with the typical values being $100 < E_{\rm peak} < 400$ keV. This model is a purely empirical description of the GRB spectra and there is currently no physical model which predicts such a spectral shape.

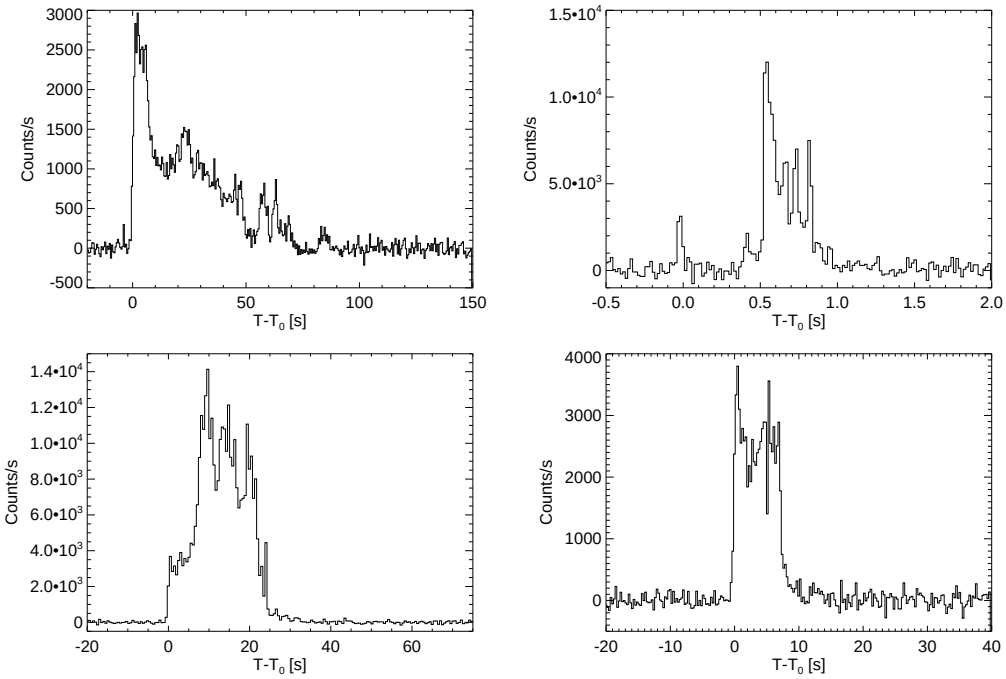

Figure 2.1 The diversity of GRBs. Four light curves GRBs observed by GBM. GRB 080916C (top left, Abdo et al., 2009b), GRB 090510A (top right, Ackermann et al., 2010), GRB 090902B (bottom left, Abdo et al., 2009a), GRB 110731A (bottom right, Ackermann et al. submitted).

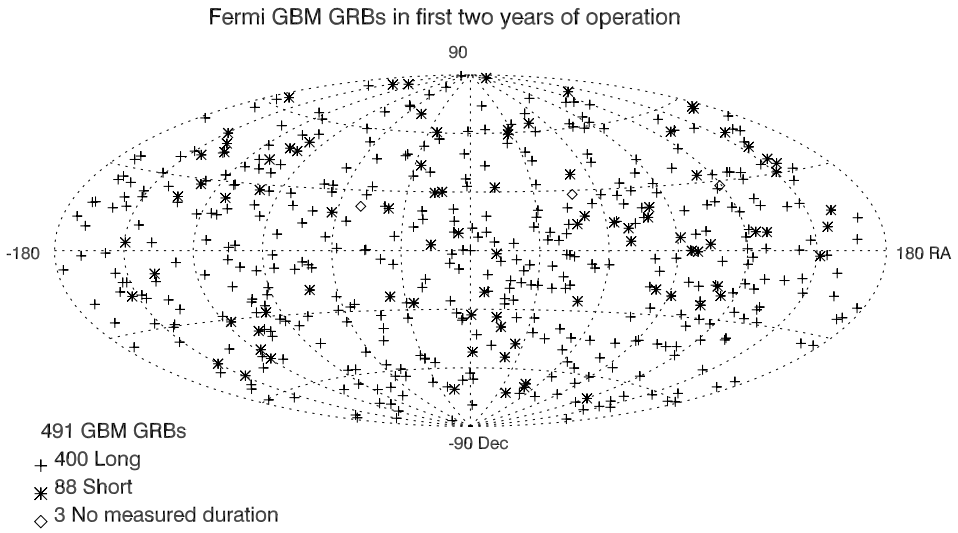

Figure 2.2 Sky distribution of GBM triggered GRBs in celestial coordinates. Crosses indicate long GRBs (T90> 2 s); asterisks indicate short GRBs. [Figure and caption taken from Paciesas et al. (2012)]

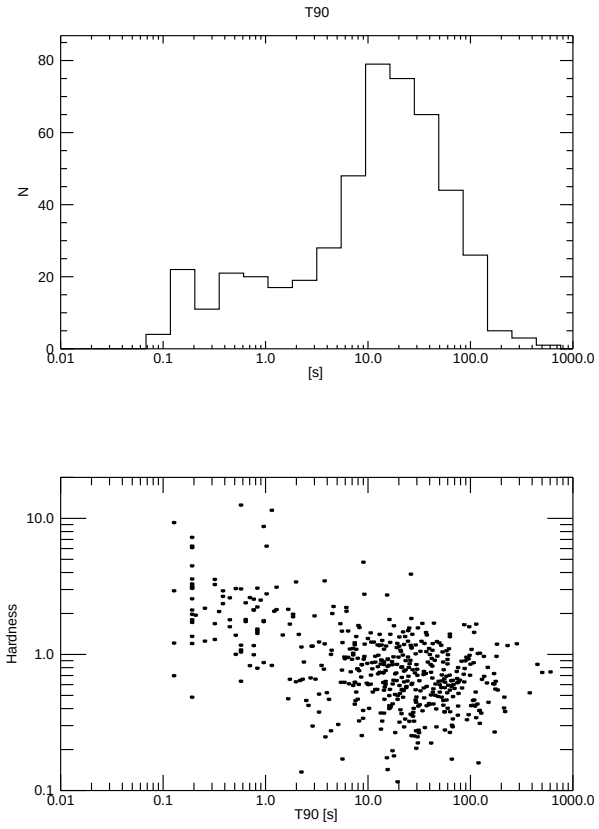

Figure 2.3 *Upper panel:* Distribution of GRB durations in the 50–300 keV energy range. *Lower panel:* Scatter plot of spectral hardness vs. duration are shown for the two duration measures T_{90}. The spectral hardness was obtained from the duration analysis results by summing the deconvolved counts in each detector and time bin in two energy bands (10–50 and 50–300 keV), and further summing each quantity in time over the T_{90} interval. The hardness was calculated separately for each detector as the ratio of the flux density in 50–300 keV to that in 10-50 keV and finally averaged over detectors. For clarity, the estimated errors are not shown but can be quite large for the weak events. Nevertheless, the anti-correlation of spectral hardness with burst duration is evident. [Figure and caption taken from Paciesas et al. (2012)]

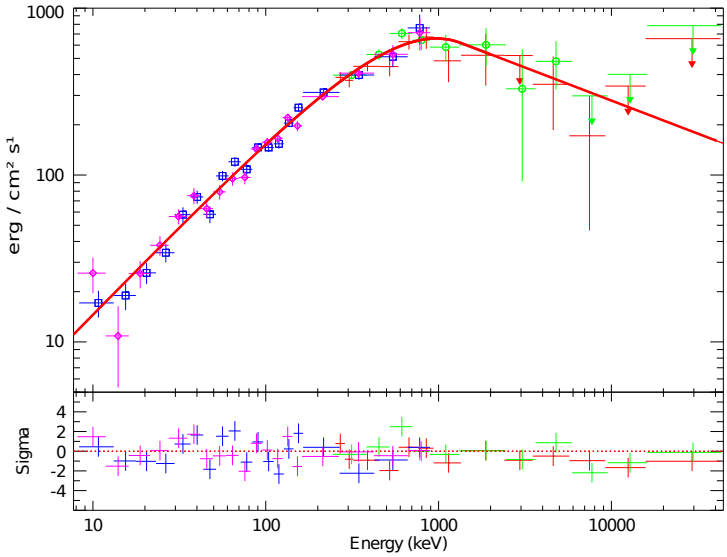

Figure 2.4 Deconvolved spectrum for GRB 120711A as observed by GBM using two NaIs (pink diamonds and blue squares) and two BGOs (green circles and red crosses). The CSPEC energy channels have been re-binned for clarity.

Unfortunately, only a handful of BATSE bursts had a measured redshift because the BATSE error boxes were too large and thus, follow-up observations with X-ray and optical instrumentation were very limited. The lack of distance measurements led to a focus of GRB studies in the observer frame without redshift corrections. Due to the cosmological origin of GRBs, such a correction is necessary to understand the intrinsic nature of these events. With the two dedicated satellites, BeppoSAX and especially *Swift*, the situation has changed. The afterglows of GRBs were identified and thanks to afterglow and host galaxy spectroscopy we have redshifts for more than 288 events by now. Unfortunately, the relatively narrow energy band of BeppoSAX (0.1 keV - 300 keV) and *Swift*/BAT (15 keV - 150 keV) limits the constraints on the prompt emission spectrum because $E_{\rm peak}$ can only be determined for low $E_{\rm peak}$ values and is often unconstrained (Butler et al., 2007; Sakamoto et al., 2009).

In § 2.3 I will take advantage of the broad energy coverage of GBM to study the primary spectral and temporal properties, such as $E_{\rm peak}$, T_{90}, the time interval in which 90% of the burst fluence has been observed, and $E_{\rm iso}$, the isotropic equivalent bolometric energy, in the rest-frame of the progenitors of 47 GRBs with measured redshift.

2.1.1 The fireball model

Major efforts have been undertaken to solve the origin of GRBs and it is now established that they originate from highly relativistic collimated outflows from a compact source with Lorentz factors $\Gamma > 100$. Even though, still today, major aspects of GRBs are not well understood, the common agreement now is that mechanisms that power a GRBs can be explained by the so called "fireball" model (Piran, 1999; Sari and Piran, 1999a). This model suggests that GRBs arise when kinetic energy of an ultra-relativistic flow is dissipated. When shells within the flow collide (so called internal shocks, see e.g. Rees and Meszaros, 1992; Meszaros et al., 1993), they produce, the "prompt emission" of the GRB, i.e. what is observed at γ-ray energies. As soon as this flow

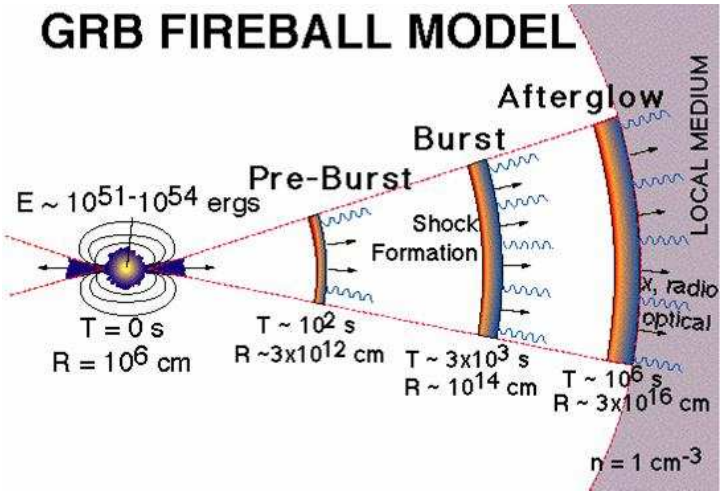

Figure 2.5 Fireball model of GRBs. For details see the main body of this thesis. [Figure taken from `http://www.swift.ac.uk/about/grb.php`]

hits the circumburst medium (either the interstellar medium or the material that was ejected by the progenitor stellar wind), an external shock arises which produces the "afterglow emission" (Waxman, 1997). The afterglow can be observed all across the electromagnetic spectrum (the afterglow radio emission can actually be visible up to years after the actual burst). In some cases, also a reverse shock arises when the external shock not only produces the forward shock into the circumburst medium, but also has a reverse shock component that propagates into the ejected material (Meszaros and Rees, 1993). This reverse shock gives rise to an early optical flash that can be observed if the ground based afterglow observations start soon enough (Shao and Dai, 2005; Gruber et al., 2011b). In § 2.2, I am going to present GRB 091024, where such an optical flash has been observed while the inner engine of the GRB was still active.

Although both emission phases are interesting by themselves, in this chapter I am going to focus mainly on the prompt emission phase as it is the one which can be observed by the GBM instrument.

2.1.2 Yonetoku and Amati relations

There have been various attempts in the past to deduce the burst luminosity (and thus its distance) from the GRB's observables. Currently, there are eight different luminosity relations (Norris et al., 2000; Fenimore and Ramirez-Ruiz, 2000; Amati et al., 2002; Schaefer, 2003; Ghirlanda et al., 2004; Firmani et al., 2006) with varying degrees of accuracy. In this section, I will focus mainly on the "Amati" and "Yonetoku" relations, simply because they are most easily derived from the GRB's prompt spectral properties.

Amati et al. (2002) found a tight relationship between $E_{\rm p,rest}$ and the isotropic equivalent bolometric energy, $E_{\rm iso}$, in the 1 keV to 10 MeV energy range. This correlation only holds for long GRBs with short GRBs being prominent outliers to this relation. Even though the Amati relation stretches over 6 orders of magnitude in $E_{\rm iso}$ and over 4 orders of magnitude in $E_{\rm p,rest}$, the scatter of the long GRBs around the best fit is relatively large. Therefore this correlation cannot be used to calibrate the GRB's luminosity with its observables. Besides this fact, there is still a debate whether this relation only arises due to selection effects.

Yonetoku et al. (2004) found a strong correlation between $E_{\rm p,rest}$ and the 1 s (64 ms) peak luminosity (L_p) in long (short) GRBs. This relation is much tighter than the Amati relation and, contrary to the latter, short GRBs follow the same relation as long GRBs.

2.2 GBM observations of the ultra-long GRB 091024[a]

2.2.1 Introduction

In this section, I examine the γ-ray properties of GRB 091024, a GRB with an extremely long duration of $T_{90} \approx 1020$ s. I present the spectral analysis of all three distinct emission episodes using data from GBM. Because of the long nature of this event, many ground-based optical telescopes slewed to its location within a few minutes and thus were able to observe the GRB during its active period. Using the optical data from the literature, I compare the optical and γ-ray light curves. Furthermore, I estimate a lower limit on the bulk Lorentz factor from the variability and spectrum of the GBM light curve and compare it with that obtained from the peak time of the forward shock of the optical afterglow.

This section is organized as follows. In §2.2.2 and §2.2.3, I describe the GBM observation and data reduction together with the spectral and spectral lag analysis of the three well-defined emission episodes. In §2.2.5, I describe the behavior of the optical afterglow data compared to the prompt γ-ray emission. In §2.2.6, I estimate a lower limit on the initial Lorentz factor using the variability time scale of the prompt emission. I discuss the position of GRB 091024 in the Yonetoku- and Amati relations in §2.2.7. Finally, in §2.2.8, I summarize my findings.

Throughout this chapter I use a flat cosmology with $\Omega_m = 0.32$, $\Omega_\Lambda = 0.68$ and $H_0 = 72 \mathrm{kms}^{-1}\mathrm{Mpc}^{-1}$ (Bennett et al., 2003; Spergel et al., 2003).

2.2.2 Observations

GBM triggered and located GRB 091024 at 08:55:58.47 (t_0) and triggered a second time at 09:06:29.36 UT (Bissaldi and Connaughton, 2009). GRB 091024 was also seen by Konus-Wind (Golenetskii et al., 2009), SPI-ACS (Rau, priv. comm.) and *Swift* (Marshall et al., 2009). However the burst was outside the *Swift*/BAT Field of view (FOV) after $t_0 + 460$ s due to an Earth-limb constraint. *Swift*/XRT determined the position to be $\alpha_{J2000} = 22^h37^m00\overset{s}{.}4$ and $\delta_{J2000} = 56°53'21''$ with an uncertainty of 6 arcsec (Page and Marshall, 2009). Unfortunately, XRT started observing the field of GRB 091024 only about 53 minutes after the BAT trigger. *Fermi* entered the South Atlantic Anomaly (SAA) 2830 s after t_0, at which time GRB emission cannot be distinguished from the background. An autonomous repoint request (ARR) was issued in order to align the burst with the FoV of the LAT at 09:12:14 UT, i.e. 976 s after the first trigger. However, no significant emission was detected in the LAT energy range during any of the time intervals in which the burst was in the LAT field of view (Bouvier et al., 2009).

Not many GRBs have been observed in the optical band while the prompt γ-ray emission was still active (the best example being GRB 990123 and GRB 080319B, see e.g. Akerlof et al., 1999; Racusin et al., 2008). For GRB 091024 optical data were acquired soon after the first trigger, and throughout its active phase. Henden et al. (2009) obtained photometry using the Sonoita Research Observatory (SRO) starting 540 s after the trigger. Ten R_c-band, nine V-band, and one I_c-band exposures were acquired. The 2m - Faulkes Telescope North started observing the field of GRB 091024 207 s after the trigger (Cano et al., 2009). The 0.6m Super LOTIS telescope started observing 58 s after the BAT trigger (Updike et al., 2009).

Optical spectra of the afterglow were obtained with the Low Resolution Imaging Spectrometer mounted on the 10-m Keck I telescope and the GMOS-N spectrograph at Gemini North, revealing a redshift of $z = 1.09$ (Cenko et al., 2009; Cucchiara et al., 2009)

[a]The main part of this work has been published by Gruber et. al (2011), *Astronomy & Astrophysics*, 533, 61G entitled *Fermi*/GBM observations of the ultra-long GRB 091024". Except for §2.2.4 and §2.2.5 all sections have been written by the author of this manuscript.

2.2.3 GBM data analysis

Using all 12 NaI detectors, I created the background subtracted light curve shown in Fig. 2.6. It shows three distinct emission periods, separated by two periods of quiescence. The first emission episode consists of at least two FRED (Fast Rise, Exponential Decay) like pulses (hereafter episode I). The time in which 90% of the fluence is observed is $T_{90,I} = 72.6 \pm 1.8$ s. Another emission episode starts 630 s after t_0. This emission period, which actually triggered GBM a second time, consists of an initial pulse ($T_{90,II} = 44.5 \pm 5.4$ s, hereafter episode II). A multi-peaked episode starts 200 s later (corresponding to 840 s after t_0) and continues for 350 s with $T_{90,III} = 150 \pm 10$ s (hereafter episode III).

Due to the highly variable background, caused by *Fermi*'s "rocking angle" observing mode, it is impossible to detect an excess in count rate during the two epochs between episode I and II and between II and III in the GBM data. I conclude that the GRB signal during these intervals, if any, is below background level. Thus, I define these two epochs as phases of quiescence.

With its very long duration of $T_{90} \approx 1020$ s, GRB 091024 is the longest burst detected by GBM and also one of the longest bursts ever seen (see Table 2.1). Among the longest events, only GRB 020410 and GRB 970315D show a multi-peaked behavior whereas the others have a long lasting FRED-like pulse.

Table 2.1 Longest bursts known to date. T_{90} of GRB 970315D was taken from the current BATSE 5B catalogue `http://gammaray.nsstc.nasa.gov`. [1] Giblin et al. (2002); Pal'Shin et al. (2008), [2] Campana et al. (2006); [3] Nicastro et al. (2004)

	$T_{90}[s]$	z	Observatories	Refs.
GRB 971208	≈ 2500	-	*BATSE*, Konus-Wind	[1]
GRB 060218	2100	0.033	*Swift*/BAT	[2]
GRB 020410	≈ 1550	-	BeppoSAX, Konus-Wind	[3]
GRB 970315D	1307		*BATSE*	unpublished
GRB 091024	1020	1.09	*Fermi*/GBM, Konus-Wind	this thesis

Spectral analysis

Photons are detected up to ~ 500 keV during all three emission episodes. For the spectral analysis, I used the method explained in § 1.2.1.

For the purposes of my spectral analysis, I used CSPEC data, from 8 keV to 40 MeV, with a temporal resolution of 1.024 s. The spectral analysis was performed with the software package RMFIT (version 3.3rc8) and the GBM Response Matrices v1.8.

Three model fits were applied, a single power-law (PL), a power-law function with an exponential high-energy cutoff (COMP) and the Band function. The best model fit is the function which provides the lowest Castor C-STAT[b] value (Cash 1979). The profile of the Cash statistics was used to estimate the 1σ asymmetric error.

[b] http://heasarc.nasa.gov/lheasoft/xanadu/xspec/manual/XSappendixCash.html

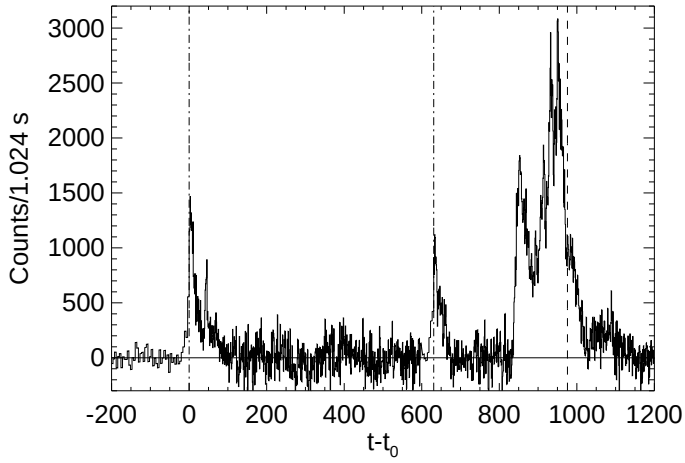

Figure 2.6 Background corrected light curve of GRB091024 in the energy range 8 - 1000 keV. The vertical dash-dotted lines show the times of the two triggers and the dashed line the beginning of the ARR.

Emission episodes I and II.

Detectors NaI 7 (53°), NaI 8 (8°) and NaI 11 (55°) had an unobstructed view of episode I. Although the GRB illuminated the spacecraft from the side, thus irradiating the BGOs through the photomultipliers, I included BGO 1 for the spectral analysis since the detector response matrix (DRM) accounts for this effect. Even though the BGO detector shows little signal throughout the duration of the burst, it was included to get an upper limit at high energies. The spectral fit was performed over the $T_{90,I}$ interval, i.e. from -3.8 s to 67.8 s. The COMP model, with $E_{\rm peak} = 412^{+69}_{-53}$ keV and energy index -0.92 ± 0.07 provides the best fit to the data.

Episode II shows a single emission period. Different detectors, i.e. NaI 6 (27°), NaI 7 (50°) and NaI 9 (32°) and BGO 1, fulfilled the selection criteria and were used for the spectral analysis. A COMP model with $E_{\rm peak} = 371^{+111}_{-71}$ keV and an index of -1.17 ± 0.07 fits episode II best.

The spectral parameters of both precursors are listed in Table 2.2.

Episode III

For episode III, starting around 830 s after trigger time, NaI 0 (13°), NaI 1 (36°), NaI 3 (53°) and BGO 0 are not occulted by the spacecraft. Due to the location of the NaI detectors on the spacecraft, detector NaI 0 blocks detector NaI 1, resulting in a significant reduction of effective area. Therefore, I excluded NaI 1 from the spectral analysis. Episode III is best fit by a COMP model with index $\alpha = -1.38 \pm 0.02$ and an exponential high energy cutoff located at $E_{\rm peak} = 278^{+22}_{-18}$ keV (see Fig. 2.7).

Interpretation

There is no indication of the first emission episodes to be systematically softer than episode III. If one adopts the definition of precursors as in Burlon et al. (2008), I conclude that

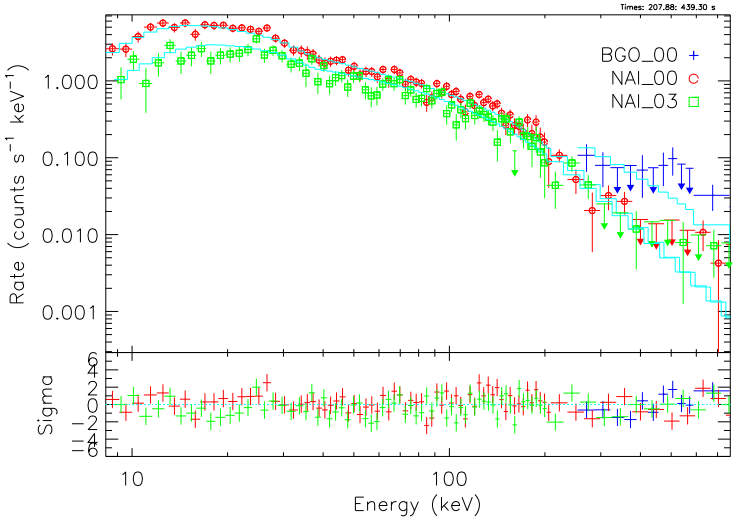

Figure 2.7 Count spectrum of episode III, best fit by a COMP model with index $\alpha = -1.38 \pm 0.02$ and a high-exponential cutoff located at $E_{\rm peak} = 278^{+22}_{-18}$ keV.

episodes I and II are likely to be produced by the same engine that produced the main GRB emission (for details see Burlon et al., 2008).

In all cases, $E_{\rm peak}$ is at about the upper end of the detected photon energies. This explains why the high energy index β of the Band function is only poorly constrained.

Fig. 2.8 shows the evolution of the Hardness Ratio (HR), defined as the ratio of the energy flux in the 100 keV - 300 keV and 10 keV - 100 keV range along the duration of the burst. There is a hard-to-soft evolution which is represented also in the evolution from higher to lower $E_{\rm peak}$ of the three emission episodes. A similar behavior is seen in other long GRBs (Kocevski and Liang, 2003; Hafizi and Mochkovitch, 2007). It is interesting to note that the overall HR-evolution over the burst duration is much larger than the canonical HR-intensity correlation between the 3 emission episodes - see the particularly soft HR of episode III despite its high intensity.

Table 2.2 Best fitting spectral parameters for the three emission episodes in GRB 091024.

T-T$_0$ [s]	model	E_p [keV]	α / index	C-Stat/DOF	Fluence [10^{-5} erg/cm^2]
-3.8 : 67.8	COMP	412^{+69}_{-53}	-0.92 ± 0.07	740/479	1.81 ± 0.07
622.7 : 664.7	COMP	371^{+111}_{-71}	-1.17 ± 0.07	798/477	0.79 ± 0.04
838.8 : 1070.2	COMP	278^{+22}_{-18}	-1.38 ± 0.02	1685/360	6.73 ± 0.09

2.2.4 Spectral lag analysis

The spectral lag of a GRB is defined as the time delay between the arrival of high-energy with respect to low-energy γ-ray photons. Typically, long-duration GRBs exhibit a hard-to-soft spectral evolution due to the decay of the peak spectral energy of the prompt emission over time (Ford et al., 1995; Kocevski and Liang, 2003; Hafizi and Mochkovitch, 2007). This is observed in the energy-resolved GRB light curves as the earlier arrival of emission of a high-energy band relative to a low-energy band. Long GRBs present a large range of spectral lags, with a typical value of 100 ms (Hakkila et al., 2007). An anti-correlation between the spectral lags of long GRBs and their peak isotropic luminosities was discovered by Norris et al. (2000), using a small sample of BATSE/BeppoSAX GRBs and subsequently confirmed with a large sample of *Swift* bursts, albeit with a significant scatter (Ukwatta et al., 2010) (see Fig. 2.9). In an extensive study of BATSE GRBs, Hakkila et al. (2008) found that the spectral lag is a property of GRB pulses rather than of the burst itself and can vary significantly for separate pulses of a GRB. The physical origin of the lag is not yet clear. However, it may be a purely kinematic effect, caused by lower-energy high-latitude emission being delayed relative to the line of sight of the observer (e.g. Salmonson, 2000; Ioka and Nakamura, 2001).

The spectral lag of a GRB is measured by cross-correlating two light curves in different energy bands as a function of temporal lag (e.g. Norris et al., 2000; Foley et al., 2008). The maximum of the cross-correlation function (CCF) then corresponds to the spectral lag of the GRB. In order to avoid spurious lag measurements due to short-timescale noise variations in the CCF, a function is fit to the CCF and the maximum of the fit to the CCF is taken as the true lag value. Statistical errors on the lag are estimated using a bootstrap method as described in Norris et al. (2000). This involves simulating 100 light curves of the GRB by adding Poissonian noise based on the observed count rates to the original light curves and recomputing the lag.

Spectral lags were measured for GRB 091024 between light curves in the 25–50 keV and 100–300 keV energy bands and in the same time intervals as those selected for the spectral analysis. High-time-resolution time-tagged event (TTE) data were used for the first two intervals. TTE data were unavailable for the final emission interval and so CTIME data were used. In each case the lag was computed at a temporal binning of 64 ms. The results are shown in Table 2.3.

The lag is seen to vary throughout the burst. The positive spectral lag for episode I of GRB 091024 indicates the hard emission leading the soft. Several authors (e.g. Kocevski and Liang, 2003; Mochkovitch et al., 2008) showed that spectral lags are directly linked to the spectral evolution of GRBs. As argued above, emission episode I should therefore show a hard-to-soft evolution. This is in line with the results of the HR analysis (see Fig. 2.8) and typical for GRB pulses. The lags of episode II and III are not well constrained. However, both are consistent with zero, i.e. no spectral evolution which is in agreement with Fig. 2.8.

In Fig. 2.9, I present the position of the 3 episodes in the lag-luminosity diagram, first presented by Norris et al. (2000). According to Norris et al. I determined the peak luminosity in the 50 keV to 300 keV energy range and find the position to be consistent with the locations of previous GRBs. Since the spectral lag of episode II is consistent with zero, I do not plot episode II in a log-log diagram.

2.2.5 Afterglow and optical flash

Using the data from Henden et al. (2009); Cano et al. (2009); Updike et al. (2009) the gross behavior of the optical afterglow light curve is shown in Fig. 2.10.

The light curve has been fitted with the superposition of two different components. Each of these components is represented by a smoothly broken power law (Beuermann et al., 1999).

Table 2.3 Results of the spectral lag analysis in the in the 25–50 keV and 100–300 keV energy bands. A positive spectral lag indicates the earlier arrival of high-energy photons with respect to low-energy photons.

	$t - t_0$[s]	Spectral Lag [s]
Episode I	-3.8 - 67.8	0.54 ± 0.13
Episode II	622.7 - 664.7	$0.38^{+0.38}_{-0.58}$
Episode III	838.8 - 1070.2	$0.10^{+0.03}_{-0.13}$

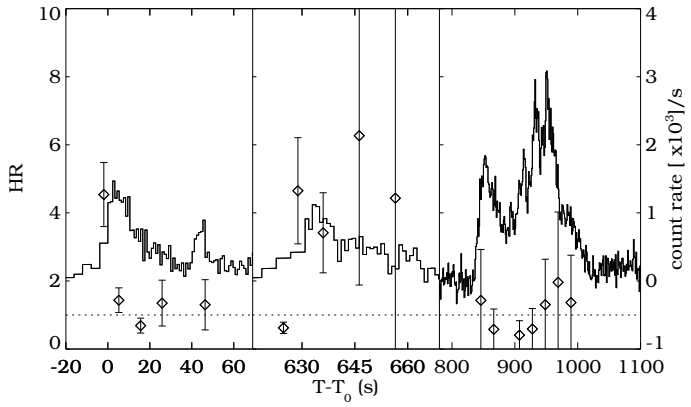

Figure 2.8 Hardness ratio (HR) of energy bands from (100 keV - 300 keV)/(10 keV - 100 keV). The solid line shows the count light curve of GRB 091024 with a time resolution of 4.096 s immediately before the two GBM triggers and a 1.024 s resolution post-trigger.

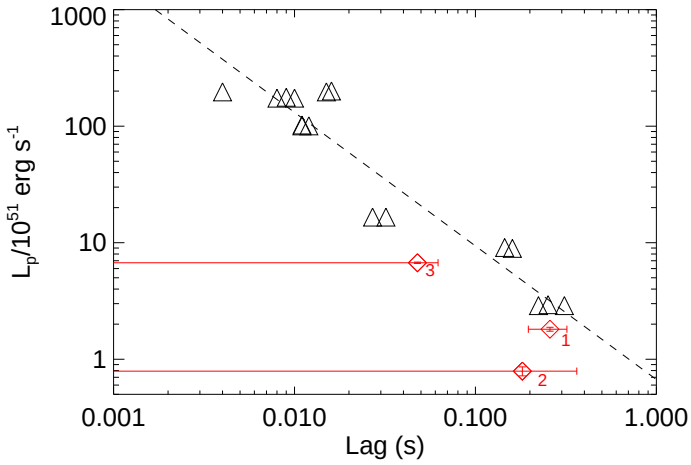

Figure 2.9 Spectral lag versus peak luminosity (50 keV - 300 keV). Red diamonds indicate the position of the 3 emission episodes of GRB 091024. Black triangles show pulses of other long GRBs presented in Norris et al. (2000).

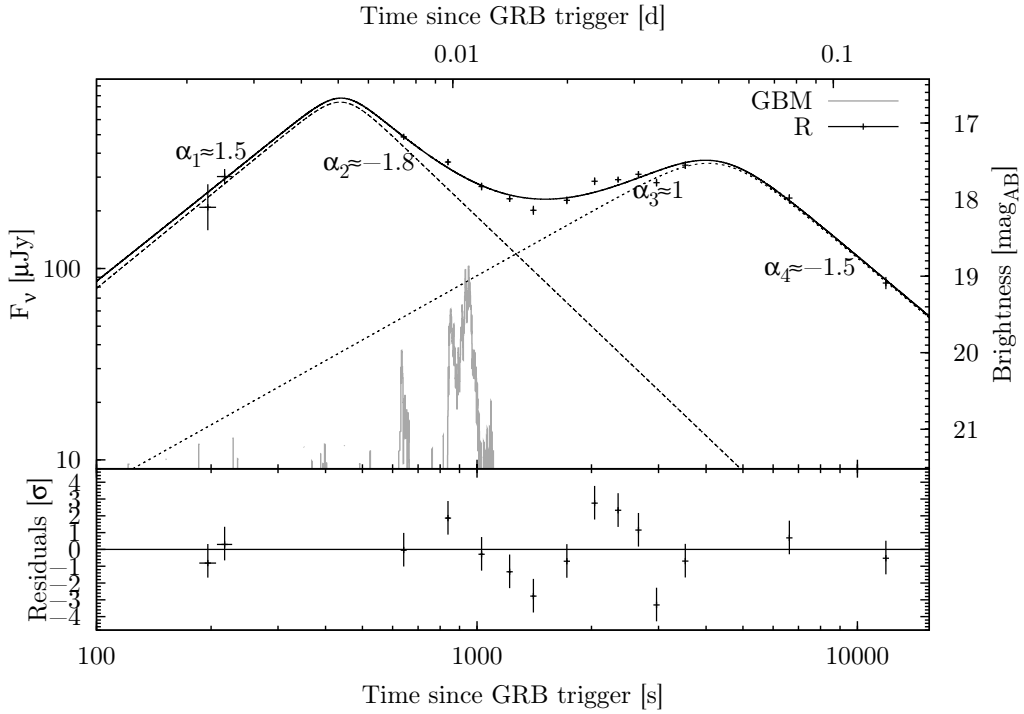

Figure 2.10 Combined r-band light curve using data points from Henden et al. (2009); Cano et al. (2009); Updike et al. (2009). The dashed line shows a reverse shock/forward shock modeling. The GBM light curve is presented in counts/s to guide the eye. *Swift*/XRT started observing 3000 s after the GBM trigger.

Given the sparsely sampled data at $t < 600$ s, and the strong variability in the light curve there is considerable degeneracy between all fit parameters. I do reach, however, the following firm conclusions: The early optical light curve initially rises and peaks at around 450 s. Forcing the first peak to be simultaneous to the second emission episode in the GBM light curve $F_\nu \propto t^\alpha$ at ~ 630 s results in a worse fit, and would require some fine-tuning of the parameters. Given that previous observations have shown the optical prompt emission to be quasi-simultaneous or somewhat later than the γ-ray photons (Vestrand et al., 2005; Page et al., 2007; Krühler et al., 2009b), the first optical peak is therefore very likely unrelated to the emission seen in the GBM at 630 s. The initial afterglow rise-index α_1 is not well constrained by the data with a value of $\alpha_1 \approx 1.0 - 2.0$, which is compatible with what has been measured for previous rising afterglow light curves (e.g. Molinari et al., 2007; Panaitescu and Vestrand, 2008; Krühler et al., 2009a; Oates et al., 2009). After the first peak, the first light curve component declines with an index of $\alpha_2 \approx -1.8$. This decay would be remarkably steep for a typical pre-jet break afterglow forward shock, but is consistent with the expectation for the decline of a reverse shock (Kobayashi, 2000). I point out the possibility that such a steep decline could also be caused by a standard afterglow in a wind-like medium if assuming $p \approx 2.7$. Under the assumption that p remains constant throughout the afterglow, I use the *Swift*/XRT X-ray spectrum (Evans et al., 2007, 2009) between T0+3300 s and T0+50000 s, finding a spectral index of $\beta_\mathrm{X} = 0.6 \pm 0.2$. Using the standard equations (see e.g. Zhang et al., 2006) I infer a value of $p = 2.2 \pm 0.4$ (for $\nu_m < \nu_\mathrm{X} < \nu_c$) which is consistent with a wind-like medium within 90%. The second peak in the light curve could then be caused for example by a refreshed shock, i.e. a late energy injection into the forward shockwave (e.g. Rees and Meszaros, 1998), or by patchy shells which represent inhomogeneities in the angular energy distribution of the jet (e.g. Kumar and Piran, 2000). However, the interpretation for a wind-like medium would require a much shallower rise ($\alpha \approx 0.5$, see Panaitescu and Vestrand, 2008) than the one actually observed ($\alpha = 1.5$, see Fig. 2.10). Although I cannot rule out the possibility of a forward shock in a wind-like circumburst medium, the light curve evolution argues against this scenario.

After the steep decay, the light curve reaches a temporary minimum at around 1200 s after which it rises again to a second peak at around 4000-5000 s. The light curve coverage is sparse around and after the second peak, but in any case the light curve peaks at a moment when there was no detection of further γ-ray emission (*Fermi* was in the SAA at this time. However, *Swift*/BAT observed the field of GRB 091024 approximately 3000 s after the trigger and reported no detection). The second afterglow peak therefore is also unrelated to the prompt γ-rays. Although sparsely sampled, the rise and the decay indices are consistent with the decay index of a typical afterglow forward shock.

Due to the lack of correlation between the optical and prompt γ-ray emission, two different processes must have produced the two emission episodes. This is well expected in the internal-external shock model of GRB emission where an external reverse shock arises due to the interaction of the ejecta and the surrounding material. The reverse shock then crosses the emitted shell, thereby accelerating the electrons which then cool adiabatically (Sari and Piran, 1999b). This shock occurs only once, hence emitting a single burst.

I extrapolated the spectrum of the prompt γ emission of the three emission epochs to calculate the monochromatic flux at a wavelength in the R_c-band (≈ 550 nm), using

$$F(\nu_0) = \frac{F_{obs}^{[\nu_1,\nu_2]}}{\nu_0^\beta} \frac{1-\beta}{\nu_2^{1-\beta} - \nu_1^{1-\beta}} \tag{2.1}$$

where F_{obs} is the energy flux in the frequency range between ν_1 and ν_2, ν_0 is the frequency at 626 nm and β is the power law index of

$$F(\nu_0) = k\nu_0^{\beta}, \tag{2.2}$$

i.e. the low-energy photon index of the spectrum, α , minus 1. For the emission episodes I and II I used 10 keV and 300 keV for ν_1 and ν_2, respectively. 10 keV to 200 keV was used for episode III because the peak energy of the time integrated spectrum is well below 300 keV. My estimate of the extrapolated monochromatic flux is conservative in the sense that I took also into consideration the error in $E_{\rm peak}$, i.e. I am using the actual value of $E_{\rm peak}$ minus the 1 sigma error and the shallowest photon index, i.e. α minus 1 sigma for the lower estimate of the monochromatic flux and $E_{\rm peak} + 1\sigma$ and the steepest photon index for the upper limit. The so obtained values for the monochromatic flux density are $40 < F(\nu_0)[\mu Jy] < 175$, $470 < F(\nu_0)[\mu Jy] < 2100$ and $14950 < F(\nu_0)[\mu Jy] < 22450$ for the emission episodes I, II and III, respectively. Before these estimates can be compared directly to the measured flux densities of the afterglow, the latter need to be corrected for Galactic foreground extinction. With $E(B-V) = 0.98$ mag and $R(V) = 3.1$, yielding $A(V) = 3.04$, the R_c band has a corrected magnitude of $A(V) \times 0.807 = 2.34$ mag. Consequently, the intrinsic monochromatic flux of the afterglow is ~ 10 times *brighter* than the observed one shown in Fig. 2.10. This, in turn, means that the flux densities derived from the extrapolation of the γ-ray spectrum are considerably lower than the intrinsic afterglow flux densities. Therefore, I can exclude a common prompt γ-ray and afterglow origin at the times of emission episodes I and II.

2.2.6 Constraints on the initial Lorentz factor

I estimate the Lorentz factor at the deceleration time scale using the afterglow peak time following Eq. 1 in Molinari et al. (2007). This implicitly assumes that the optical afterglow peak is caused by the fireball forward shock model (Sari and Piran, 1999b; Mészáros, 2006). The Lorentz factor, for a homogeneous surrounding medium with particle density $n = n_0\,{\rm cm}^{-3}$, at the time of deceleration is then

$$\Gamma_{\rm dec}(t_{\rm peak}) = \left(\frac{3E_\gamma(1+z)^3}{32\pi n m_p c^5 \eta t_{\rm peak}^3}\right)^{1/8} \approx 160 \left(\frac{E_{\gamma,53}(1+z)^3}{\eta_{0.2} n_0 t_{\rm peak,2}^3}\right)^{1/8}, \tag{2.3}$$

where $E_\gamma = 10^{53} E_{\gamma,53}$ erg is the isotropic-equivalent energy released by the GRB in the 1 keV to 10 MeV energy band, $\eta = 0.2\eta_{0.2}$ the radiative efficiency, $t_{\rm peak,2} = t_{\rm peak}/(100{\rm s})$, m_p the proton mass, c the speed of light and z the redshift. Molinari et al. (2007) also provide an estimate for a wind environment with

$$\Gamma_{\rm dec}(t_{\rm peak}) = \left(\frac{E_\gamma(1+z)}{8\pi A m_p c^3 \eta t_{\rm peak}}\right)^{1/4}, \tag{2.4}$$

where A is a constant defined as $n(r) = Ar^{-2}$ and in this case $A^* = A/(3\times10^{35}{\rm cm}^{-1}) = 1$. The initial Lorentz factor is then estimated by simply multiplying Γ_{dec} by 2 (Mészáros, 2006; Panaitescu and Kumar, 2000). The afterglow light curve peaks twice (Fig. 2.10): the first time at ~ 400 s and a second time at ~ 4000 s, respectively. Assuming that the first peak is caused by the forward shock ($t_{\rm peak} = 400$ s), the Lorentz factor in a homogeneous medium is $\Gamma_0 \approx 290$ and $\Gamma_0 \approx 150$ in a wind environment. However, if one interprets this peak as the optical flash of the reverse shock, as I prefer to do (see §2.2.5) and uses the peak time of the second optical peak ($t_{\rm peak} = 4000$ s), one gets $\Gamma_0 \approx 120$ for the homogeneous medium and $\Gamma_0 \approx 80$ for the wind environment.

Table 2.4 Parameters and lower limit of Γ_0 obtained using Eqs. 4 and 8 from Lithwick and Sari (2001). The photon flux was determined in the energy range from 500 keV to 1 MeV.

β	flux F_{ph} [ph/cm^2/s]	f [ph/cm^2/s/MeV$^{1-\beta}$]	$\Gamma_{0,\min}$
$2.57^{-0.39}_{+1.20}$	0.056 ± 0.007	0.044 ± 0.006	195^{+90}_{-110}

According to Lithwick and Sari (2001) one can estimate a lower limit of the initial Lorentz factor, Γ_0, from the spectral properties and the variability timescales of the prompt γ-ray emission from the GRB. I used

$$\Gamma_0 > (180/11)^{1/(2\beta+6)}\, \tau^{1/(\beta+3)}\, (1+z)^{(\beta-1)/(\beta+3)}\,, \text{where} \tag{2.5}$$

$$\tau = \frac{\sigma_T\, d_L^2\, (m_e c^2)^{1-\beta}\, f}{c^2\, \delta t\, (\beta - 1)}. \tag{2.6}$$

In the above equations δt is the smallest detectable variability and f is the normalization constant of the observed photon flux, defined as $N(E) = f\, E^{-\beta}$. Unfortunately, few photons with energies greater than 500 keV were detected. Assuming that the spectrum extends to higher energies I used the high-energy photon index β and extrapolated the power-law slope starting at 500 keV into the high-energy domain up to 1 MeV. The shortest variability time scale which can be detected in the GBM data changes between the three pulses. Episode I has $\delta t = 64$ ms, episode II $\delta t = 96$ ms and episode III $\delta t = 32$ ms. However, only episode I has a constrained high-energy photon index β. Therefore, only for this episode an actual value for $\Gamma_{0,\min}$ be deduced (intercept between red vertical line and dash-dotted line in Fig. 2.11) and reported in Table 2.4. In Fig. 2.11, I plot the lower limits of the initial Lorentz factors for all three emission episodes as a function of β.

2.2.7 Correlations

The peak luminosity is calculated with $L_p = 4\pi d_l^2 F_p$, where d_l is the luminosity distance and F_p the peak energy flux. I determined L_p, in the energy range between 1 keV and 10 MeV in the rest frame of the GRB for each pulse (though I had to extrapolate above $\sim$ 500 keV up to 10 MeV). Interestingly, my values are all below the Yonetoku relation, well outside the 1σ scatter, as is clearly shown by the black dots in Fig. 2.19.

In order to determine the position of GRB 091024 in the Amati relation, I estimated a time *integrated* $E_{\rm peak}$ value by making a time-weighted $E_{\rm peak}$-average of the 3 emission episodes which results in $E_{\rm peak} = 315^{+43}_{-32}$. Summing up E_{iso} gives 3.5×10^{53} erg. I present the position of GRB 091024 in the $E_{\rm p,rest}$-$E_{\rm iso}$ plane in Fig. 2.18. Additionally, I show the positions of the three emission episodes separately. Similar to GRB 980425 (Galama et al., 1998) and GRB 031203 (Malesani et al., 2004), emission episodes I and II are both outliers to the relation. This shows that, in principle, outliers of the Amati relation could be caused by the sensitivity of the instrument or visibility constraints. If the GRB was active for a longer period than it could actually be observed, it would end up as an outlier on the Amati relation. However, this might then not be due to an intrinsic, physical property of the GRB. Take as an example GRB 091024: *Swift*/BAT only observed the first emission episode because of an Earth-limb constraint. If no

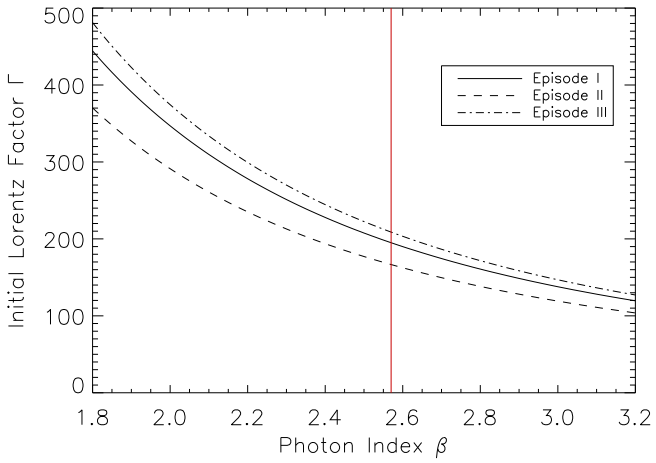

Figure 2.11 Deduced lower limit of Γ_0 as a function of the photon index β using Lithwick and Sari (2001) for episode I at t_0 (continuous line), episode II at t_0+630 s (dashed line) and episode III at t_0+830 s (dashed-dotted line). The red vertical line indicates the photon index of the Band model of the first emission epoch.

Table 2.5 Rest-frame $E_{\rm peak}$, peak fluxes and peak luminosities of GRB 091024.Peak fluxes, F_p, are in units of [10^{-7} erg/cm^2/s] and peak luminosities, L_p, in units of [10^{51} erg/s] .

	$E_{\rm p,rest}$ [keV]	F_p [1 keV - 10 MeV]	L_p [1 keV - 10 MeV]
Episode I	860^{+140}_{-110}	7.0 ± 1.0	5.3 ± 0.7
Episode II	780^{+290}_{-150}	6.2 ± 3.5	4.6 ± 2.6
Episode III	580^{+50}_{-40}	14.0 ± 3.0	10.5 ± 2.2

other mission would have detected this burst, episode I would likely have been interpreted as the complete GRB resulting in a $> 2\sigma$ outlier of the Amati relation.

2.2.8 Conclusions

GRB 0910124 was a very long burst which lasted for $T_{90} \approx 1020$ s. I found that the optical light curve is highly anti-correlated to the prompt γ-ray emission, with the optical emission reaching the maximum during an epoch of quiescence in the prompt emission. I interpreted this behavior as the reverse shock (optical flash), expected in the internal-external shock model of GRB emission but observed only in a handful of GRBs so far. The second optical peak, at t_0+4000 s, is then due to the forward shock.

Using GBM data, I performed a spectral and spectral lag analysis of the three distinct emission episodes in γ-rays. I note that despite its unusually long duration, this burst is similar to other long GRBs, i.e. there is spectral evolution (both the peak energy and the spectral index

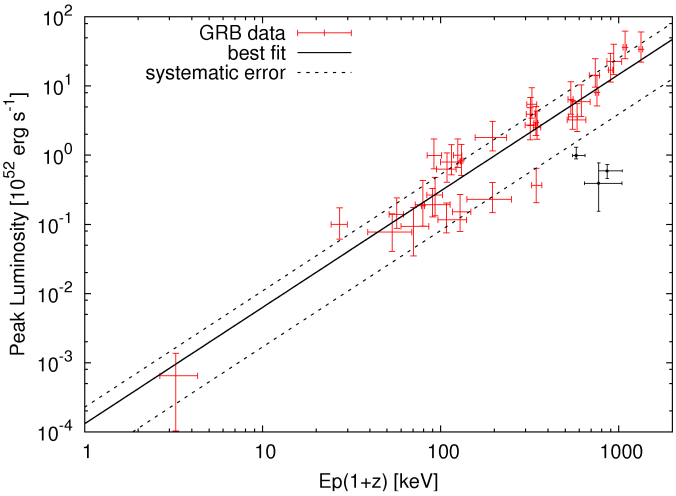

Figure 2.12 Peak luminosity, L_p, and rest frame peak energy, $E_{\rm p,rest}$. Figure adapted from Kodama et al. (2008). Red dots show 33 GRBs with $z < 1.62$. The solid line shows the fit to the red data points, the dashed lines show the systematic error. Black dots are the values for the three emission epochs in GRB 091024.

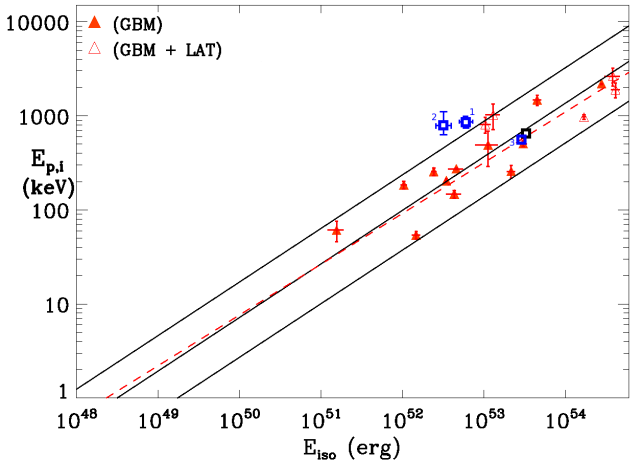

Figure 2.13 The three emission episodes indicated as blue squares in the $E_{\rm p,rest}$-$E_{\rm iso}$ plane. The black square shows the "summed" position of GRB 091024, obtained using time-integrated quantities (see text for details). Red triangles indicate long GBM GRBs as presented in Amati (2010) together with the best fit to this data (dashed red line). The black solid line shows the best-fit power-law, known as the "Amati relation" together with the $\pm 2\sigma$ c.l. region (Amati et al., 2008).

vary with time) and spectral lags are measured.

Additionally, from the smallest detectable variability time scale, I estimated the lower limit on the bulk Lorentz factor using the Eqs. from Lithwick and Sari (2001) and found it to be $\Gamma_{0,\mathrm{min}} = 195^{+90}_{-110}$. From the peak time of the forward shock, i.e. the time when the blast wave has decelerated, I determined the Lorentz factor to be $\Gamma_0 \approx 120$ according to Molinari et al. (2007) for a homogeneous ISM which is perfectly consistent with the lower limit mentioned above and with Lorentz factors of other long bursts. GRB 091024 is one of the few bursts where Γ could be estimated using two different methods.

GRB 091024, while being consistent with the Amati relation, is a $> 1\sigma$ outlier to the Yonetoku relation.

2.3 Rest-frame properties of 32 Gamma-Ray Bursts observed by the *F*ermi Gamma-Ray Burst Monitor[c]

2.3.1 Introduction

In this chapter, I study the main spectral and temporal properties of GRBs observed by GBM. I investigate these key properties of GRBs in the rest-frame of the progenitor and test for possible intra-parameter correlations to better understand the intrinsic nature of these events. My sample comprises 47 GRBs with measured redshift that were observed by GBM until May 2012. 39 of them belong to the long-duration population and 8 events were classified as short/hard bursts. For all of these events I derive, where possible, the intrinsic peak energy in the νF_ν spectrum ($E_{\rm p,rest}$), the duration in the rest-frame, defined as the time in which 90% of the burst fluence was observed ($T_{90,\rm rest}$) and the isotropic equivalent bolometric energy ($E_{\rm iso}$).

2.3.2 GRB sample and analysis

The selection criterion for my sample is solely based on the redshift determination. I form a sample of 47 bursts detected by GBM between July 2008 (first GBM GRB detection) up to May 2012 with known redshift (determined either spectroscopically or photometrically from the afterglow. These redshifts are taken from the literature).

My sample contains 8 short and 39 long GRBs, see Table 2.7. The redshift distribution of the GBM GRBs is shown in Fig. 2.14 together with a histogram of all 239 GRBs with redshift determinations to date[d]. A two-tailed Kolmogorov-Smirnov (KS) test between the full sample and the GBM-only sample shows that the two distributions are very similar ($P = 84$ %). In conclusion, the GBM-only sample is representative of the full GRB sample with redshift.

The peak energy ($E_{\rm peak}$)

For the $E_{\rm peak}$ determination, the data of the GBM spectral catalogue (Goldstein et al., 2012) were taken, if available. If the GRBs were observed after July 2010, the data analysis was carried out according to, and consistent with, the GBM spectral catalogue. Before an intrinsic $E_{\rm peak}$ distribution could be created or any conclusions on the intrinsic $E_{\rm peak}$ properties could be drawn, a first important issue which needed to be addressed is whether the observed $E_{\rm peak}$ distribution by GBM is drawn from the same $E_{\rm peak}$ distribution as the bursts which were observed by BATSE. Because of the broader sensitivity of GBM to higher energies, there could be a significant deviation towards higher $E_{\rm peak}$ values. To answer this question, I used the BATSE catalogue[e] from which I extracted the $E_{\rm peak}$ values which were obtained from the time averaged spectra (fluence spectral fits). Ignoring the power-law (PL) and Gaussian Log fits, I elected to the COMP model, smoothly broken power law (SBPL) and Band function for the purpose of this test. For all models with a peak energy it was required that $\Delta E_{\rm p}/E_{\rm p} \leq 0.4$. The SBPL was preferred over the Band model only when the difference in χ^2 was larger than 6 between these two models. For both models it was required that the high-energy power law index $\sigma_\beta \leq 0.75$. The break energy obtained from the SBPL model was transformed to the

[c]The main part of this work has been published in Gruber et al. (2011a) *Astronomy & Astrophysics*, 531, 20 entitled *Rest-frame properties of 32 Gamma-Ray Bursts observed by the* F*ermi Gamma-Ray Burst Monitor* and has been updated with the most recent numbers from Gruber and for the Fermi/GBM collaboration (2012a) "Gamma-Ray Bursts 2012", Munich, May 7–11, 2012, eds. A. Rau and J. Greiner, PoS(GRB 2012)007 entitled *Rest-frame properties of Gamma-Ray bursts observed by the Fermi Gamma-Ray Burst Monitor*

[d]`www.mpe.mpg.de/~jcg/grbgen.html`

[e]`www.batse.msfc.nasa.gov/~goldstein/`

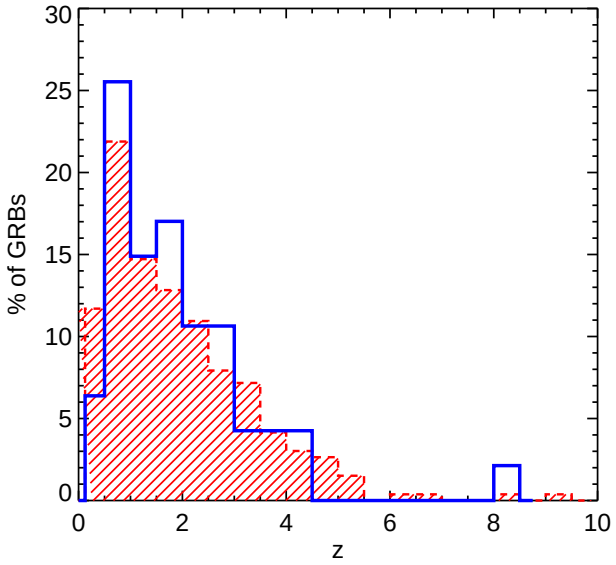

Figure 2.14 Redshift distribution in % of GBM GRBs (blue solid line) compared to all GRBs with measured redshift to date (red dashed line). Both samples contain long and short bursts.

$E_{\rm peak}$ value according to Kaneko et al. (2006) and Goldstein et al. (2012). If neither of the aforementioned models fulfilled the requirements, the COMP model was the preferred model if the χ^2 of the latter is smaller than the one for the simple power law model. Both long and short GRBs were included in this analysis. The so obtained $E_{\rm peak}$ distribution is shown in Fig. 2.15.

The same selection cut was applied to the 2-year GBM spectral catalogue. The blue histogram in Fig. 2.15 shows this distribution. All distributions have a median $E_{\rm peak}$ of ≈ 210 keV and show the same standard deviation. A KS test proved that the difference between the GBM and BATSE $E_{\rm peak}$ samples is not statistically meaningful ($P = 9\%$). This means that the two histograms are drawn from the same distribution, in agreement with Nava et al. (2010). I note that Bissaldi et al. (2011) showed that the $E_{\rm peak}$ distribution of some GBM-GRBs extends to higher energies compared to BATSE (Kaneko et al., 2006). However, this is of no surprise as Amati et al. (2002) demonstrated that bursts with higher fluence, i.e. higher $E_{\rm iso}$, have, on average, higher $E_{\rm peak}$ (see also §2.3.3). Since Bissaldi et al. (2011) only used bright GRBs, it is to be expected that their $E_{\rm peak}$ distribution is shifted to higher energies. I conclude that GBM, although being sensitive up to 40 MeV, did not find a previously undiscovered population of high-$E_{\rm peak}$ GRBs.

The KS test was then applied to both the $E_{\rm peak}$ distributions between the whole sample of GBM bursts and the 40 GBM bursts with measured redshift (for 7 bursts a PL model fits the data best) and also to the $E_{\rm peak}$ distribution of BATSE bursts and the $E_{\rm peak}$ distribution of GBM bursts with measured redshift. In neither case the differences were statistically meaningful ($P = 85\%$ and $P = 89\%$, respectively). Thus, all 3 histograms are very likely drawn from the same distribution. In conclusion, the sample of GBM GRBs with measured redshift presented here is representative for the whole population of GRBs which were ever observed by BATSE and GBM.

There is one caveat, however: GBM cannot measure $E_{\rm peak}$ values which are lower (or higher) than a certain limiting threshold, i.e. $E_{\rm peak}$ can only reliably measured if it is within the energy

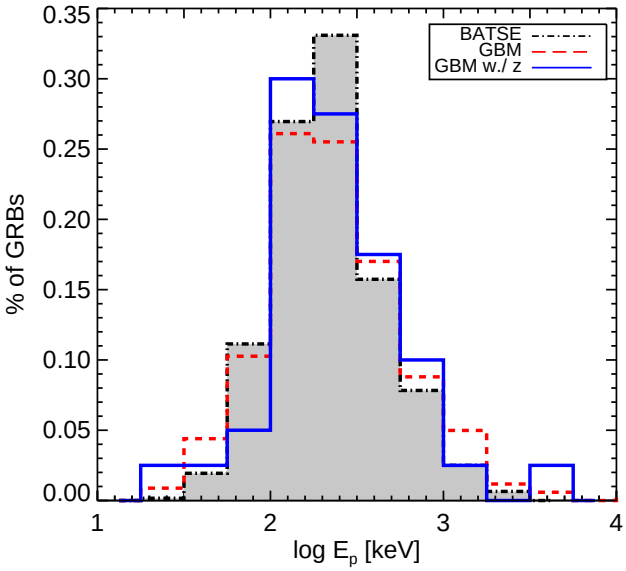

Figure 2.15 $E_{\rm peak}$ values of 1244 BATSE/CGRO GRBs (light grey filled histogram), 341 GBM GRBs (red dashed histogram) and 40 GBM GRBs with redshift measurement (blue solid histogram). A KS test suggested that all three samples were drawn from the same distribution.

range of the detectors. It is well known that $E_{\rm peak}$ values of GRBs can go as low as a few keV. Pélangeon et al. (2008) for example found $E_{\rm peak}$ values as low as $\sim$ 2 keV in GRBs that were observed by *HETE-2*. These low energetic events have been classified as X-ray flashes (XRF) or X-ray rich bursts (XRB) (see e.g. Heise and in 't Zand, 2001; Sakamoto et al., 2005). However, it is very likely that XRFs and XRBs are nothing else than weak and long GRBs (see Kippen et al., 2004, and references therein).

The borderline $E_{\rm peak}$ value is obviously located somewhere near the low-energy sensitivity of the NaIs. Thus, in order to determine a potential bias in the $E_{\rm p,rest}$ distribution shown in Fig. 2.16, it is important to understand and quantify the limits of the GBM to measure $E_{\rm peak}$ (be it either from the COMP model or Band function).

For this purpose, I created a set of simulated bursts with different initial spectral and temporal starting values. I input the source lifetime (t_S, 1 s, 5 s, 10 s, 100 s) and the photon flux (f) in the 10 keV to 1 MeV range (1, 3 and 10 ph cm^{-2} s^{-1}). For the simulation, the Band function was chosen as the photon model with varying $E_{\rm peak}$ (15,17, 25, 50, 100 keV) but fixed $\alpha = -0.8$ and $\beta = -2.4$. I simulated these bursts overlaid on real background data by using detector NaI 7 of GRB 090926A[f]. This resulted in 60 different burst models. For each model, I created 1000 bursts to account for Poissonian noise. This resulted in 60000 spectra, each of which was then fitted with the Band function using the detector response matrix (DRM) of detector NaI 7 created for the location of GRB 090926A.

After the fitting procedure, I rejected those bursts which have $\Delta E_{\rm p}/E_{\rm p} \geq 0.3$ and $\sigma_\alpha \leq 0.4$. These rejected spectra are then defined as unconstrained. I did not apply this criterion to the high-energy power law index β. A spectral fit that has a constrained $E_{\rm peak}$ and α but an

[f]The choice of NaI 7 and the choice for this specific GRB is completely arbitrary. I could have chosen any other detector that observed any other real GRB.

unconstrained β was simply considered a COMP model. In Table 2.6, I report the mean and standard deviation of the output spectral parameters, $E_{\rm peak}$ and α, of the simulated bursts.

The conclusions of this exercise are:

1. GBM can recover $E_{\rm peak}$ values as low as ≈ 15 keV. The fact that the observed $E_{\rm peak}$ distribution is indeed biased is in clear contradiction to e.g. Brainerd et al. (2000). They argued that the observed $E_{\rm peak}$ distribution (by BATSE in this case) is actually the intrinsic one.

2. the input $E_{\rm peak}$ parameter can be recovered from the simulated spectra within the 2 σ errors for almost all simulated flux levels and source lifetimes.

3. GRBs with low fluxes, low $E_{\rm peak}$ and short t_s are more likely to be rejected than GRBs with higher fluxes, higher $E_{\rm peak}$ or longer t_s

4. the low-energy power law index α tends to get softer, i.e. to have lower values, for low $E_{\rm peak}$ and low fluxes. This last point is particularly noteworthy. Crider et al. (1997), Lloyd-Ronning and Petrosian (2002) and later Kaneko et al. (2006) found a significant correlation between $E_{\rm peak}$ and α in the time-resolved spectra of several GRBs. Supported by my simulations, I point out the possibility that a parameter reconstruction effect is at work in addition to any intrinsic correlation between $E_{\rm peak}$ and α. This effect has already been brought forward by Preece et al. (1998); Lloyd and Petrosian (2000) and Lloyd-Ronning and Petrosian (2002). In short, it depends on how quickly α can reach its asymptotic value and how close $E_{\rm peak}$ is located to the low-energy limit of the instrument's energy bandpass. The closer $E_{\rm peak}$ is situated to the detector's sensitivity limit, the fewer is the number of photons in the low-energy portion of the spectrum. This makes it increasingly difficult to determine the asymptotic value of α. Instead, a more negative value of the low-energy power law index will be measured which is what is observed here.

In Fig. 2.16, I present a histogram of $E_{\rm p,rest}$ of my sample of GBM GRBs where a $E_{\rm peak}$ measurement was possible. The distribution of all bursts has mean and median values of 0.9 MeV and 0.7 MeV, respectively. In the canonical scenario of GRB jets, turbulent magnetic fields build up behind the internal shock, and electrons produce a synchrotron power law spectrum. The typical rest-frame frequency $\nu_{\rm rest}$ in the internal shock dissipation is $\nu_{\rm rest} \propto 0.2\, L_{52}^{1/2}\, r_{13}^{-1}$MeV (Zhang and Mészáros, 2002), where L_{52} is the luminosity in 10^{52} erg/s and r_{13} the dissipation radius in units of 10^{13} cm. The measurement of the rest-frame peak energy therefore leads to a constraint of $L_{52}^{1/2}\, r_{13}^{-1} \approx 3.5$ (in the above units).

Recently, Collazzi et al. (2011) reported that the width of the $E_{\rm p,rest}$ distribution must be close to zero with the peak value located close to the rest-mass energy of electrons at 511 keV. This effectively implies that all GRBs must be thermostated by some unknown physical mechanism. I tested this claim by determining the width of the $E_{\rm p,rest}$ distribution ($\sigma_{\log E_p(1+z)} = 0.45$) together with all the individual errors that add to the uncertainty of the $E_{\rm peak}$ measurement in log-space, using eq. 1 in Collazzi et al. 2011:

$$\sigma^2_{\rm Total} = \sigma^2_{\rm Poisson} + \sigma^2_{\rm Det} + \sigma^2_{\rm Choice} + \sigma^2_{\rm Def}. \tag{2.7}$$

$\sigma_{\rm Choice}$ describes the different choices made by different analysts. Since all the bursts in this thesis were analyzed consistently (selection of the time interval, energy range, etc.), I could set $\sigma_{\rm Choice} = 0$. $\sigma_{\rm Det}$ is the error which results in not knowing the detector response perfectly. However, according to Collazzi et al., $\sigma_{\rm Det}$ is negligibly small, meaning that the calibrations of the detectors are usually well understood. $\sigma_{\rm Def}$ describes the differences that are obtained in $E_{\rm peak}$ when using different photon models. As it was shown already by e.g. Band et al.

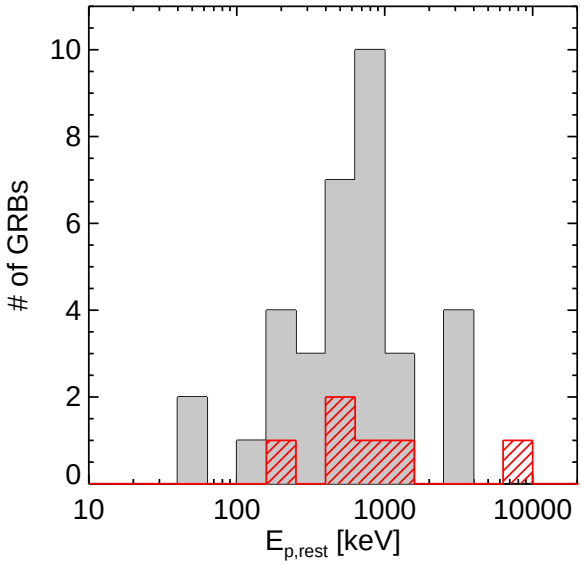

Figure 2.16 Rest-frame distribution of $E_{\rm peak}$ for 6 short (red hatched histogram) and 34 long (grey filled histogram) GBM-GRBs. The two distributions have mean values of 0.4 MeV and 0.3 MeV and median values of 0.7 MeV and 0.4 MeV, respectively.

(1993) and Kaneko et al. (2006) the COMP model results in higher $E_{\rm peak}$ values than the Band function. Collazzi et al. use $\sigma_{\rm Model} = 0.12$ to account for this difference. Here, I determine this value using constrained $E_{\rm peak}$ values of both the COMP and Band model taken from Goldstein et al. (2012), which yields $\sigma_{\rm Model} = \sigma_{\rm Def} = 0.15$. The Poissonian errors are $\sigma_{\rm Poisson} \approx 0.10$ in log-space. Thus $\sigma_{\rm Total} = \sqrt{0.12^2 + 0.1^2} = 0.18$.

Inserting the just found values in

$$\sigma^2_{E_p{\rm int}} = \sigma^2_{\log E_p(1+z)} - \sigma^2_{\rm Total}, \tag{2.8}$$

yields $\sigma_{\log E_p{\rm int}} = 0.41$ keV. However, a zero width in the $E_{\rm peak}$ distribution is synonymous with $\sigma_{E_p{\rm int}} = 0$. The conclusion is that the $E_{\rm p,rest}$ distribution does not have a zero width. This finding is in conflict with the implications and conclusions discussed in Collazzi et al.

The GRB duration (T_{90})

For determining the duration of a GRB, I applied the method first introduced by Kouveliotou et al. (1993). They defined the burst duration as the time in which 90% of the burst counts is collected (T_{90}). Here, I adopted the same definition. However, whereas the burst's fluence was used in Gruber et al. (2011a), here I referred again to the burst's counts. The T_{90} value depends highly on the detector and on the energy interval in which it is determined (see e.g. Bissaldi et al., 2011). Additionally, since I was interested in durations in the rest-frame of the GRB, it was not sufficient to simply account for the time dilation due to cosmic expansion by dividing the measured durations by $(1 + z)$. The energy band in which the T_{90} is determined needed to be redshift corrected as well. I determined the burst duration in fluence space in the

rest-frame energy interval from 100 keV to 500 keV, i.e. in the observer frame energy interval from $100/(1+z)$ keV to $500/(1+z)$ keV.

In Fig. 2.17, I present the rest-frame distribution of T_{90} of my sample of 47 GBM GRBs. The number of short bursts is still too small to unambiguously recover a bimodal distinction of short and long events in the rest-frame. Henceforth, a distinction was made between the short and long class of GRBs using an ad-hoc definition of $T_{90,\mathrm{rest}} \leq 2$ s for short bursts and $T_{90,\mathrm{rest}} > 2$ s for long bursts, although I did have neither observational nor physical evidence to support such a distinction in the GRB sample presented here. All GRBs in my sample that were defined as short in the observer-frame, also remained short with the here adopted definition. I note that GRB 100816A is peculiar in that it is classified as a short burst by GBM data ($T_{90} = 1.16 \pm 0.06$ s), but it had a $T_{90} = 2.9 \pm 0.6$ in the 15 keV - 350 keV energy range in *Swift* data with a low-level emission out to about T0+100 (Markwardt et al., 2010).

The mean value of the whole $T_{90,\mathrm{rest}}$ distribution is 27.6 s and the median value is 11.9 s.

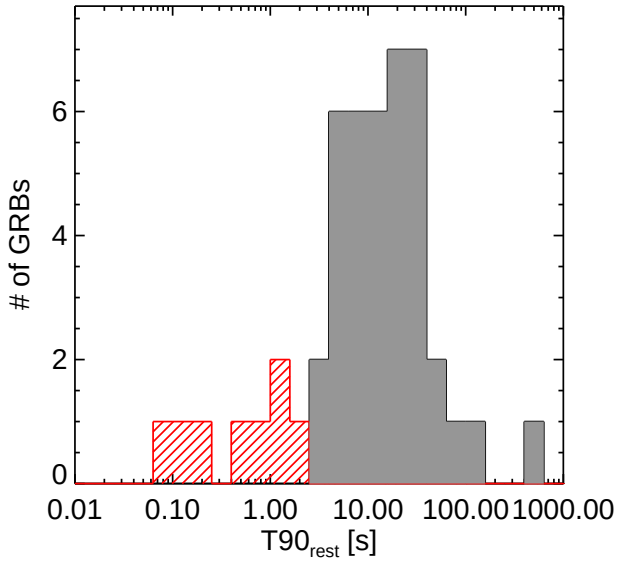

Figure 2.17 $T_{90,\mathrm{rest}}$ distribution of 8 short (red hatched histogram) and 39 long (grey histogram) GBM GRBs in the redshift corrected energy interval from 100 keV to 300 keV.

Table 2.7: Redshift, E_{peak} and T_{90} (all observer-frame) of the 47 GRBs used in this section.

GRB ID	**z**	E_{peak} **[keV]**	T_{90} **[s]**
GRB 120119A	1.728	174.9 ± 6.7	58.5 ± 2.6
GRB 111228A	0.714	20.85 ± 1.0	49.2 ± 0.5
GRB 111107A	2.893	218.1 ± 55.7	32.8 ± 2.1
GRB 110818A	3.36	171.5 ± 47.1	82.2 ± 7.3

Continued on next page

Table 2.7: Redshift, $E_{\rm peak}$ and T_{90} (all observer-frame) of the 47 GRBs used in this section.

GRB ID	**z**	$E_{\rm peak}$ **[keV]**	T_{90} **[s]**
GRB 110801A	1.858	47.02 ± 18.9	380.9 ± 16.7
GRB 110731A	2.83	324.0 ± 17.6	7.5 ± 0.2
GRB 110213A	1.46	57.49 ± 7.5	30.3 ± 0.6
GRB 110128A	2.339	–	14.8 ± 3.6
GRB 110106B	0.618	138.7 ± 28.0	20.4 ± 0.5
GRB 101219B	0.55	–	44.9 ± 2.1
GRB 100906A	1.727	146.3 ± 19.9	103.1 ± 0.8
GRB 100816A	0.8049	133.0 ± 6.9	2.1 ± 0.1
GRB 100814A	1.44	127.7 ± 8.8	148.7 ± 0.6
GRB 100414A	1.368	$663.7 \pm 16.$	121.4 ± 0.1
GRB 100206A	0.407	454.2 ± 93.3	0.11 ± 0.02
GRB 100117A	0.920	322.5 ± 68.7	0.29 ± 0.2
GRB 091208B	1.063	44.6 ± 7.3	11.8 ± 0.5
GRB 091127	0.490	35.5 ± 1.5	7.9 ± 0.2
GRB 091029A	2.752	47.47 ± 17.6	61.4 ± 20.9
GRB 091024	1.092	189.8 ± 17.7	≈ 1020
GRB 091020	1.710	246.2 ± 35.8	23.2 ± 0.7
GRB 091003	0.897	366.4 ± 26.7	20.2 ± 0.2
GRB 090927	1.370	–	0.59 ± 0.02
GRB 090926B	1.240	82.5 ± 3.0	47.5 ± 1.9
GRB 090926	2.106	336.4 ± 5.6	13.6 ± 0.1
GRB 090902B	1.822	1044.3 ± 17.1	19.6 ± 0.1
GRB 090618	0.540	85.9 ± 4.5	106.5 ± 0.2
GRB 090519	3.850	1754.1 ± 986.5	37.8 ± 1.2
GRB 090516	4.109	142.0 ± 26.4	91.1 ± 0.4
GRB 090510	0.903	4300.3 ± 483.5	0.88 ± 0.02
GRB 090424	0.544	154.1 ± 3.8	4.5 ± 0.1
GRB 090423	8.260	–	10.8 ± 1.8
GRB 090328	0.736	1457.7 ± 74.4	52.5 ± 0.2
GRB 090323	3.570	639.3 ± 41.9	132.8 ± 0.4
GRB 090102	1.547	416.5 ± 17.6	23.0 ± 0.7
GRB 081222	2.770	142.3 ± 9.5	18.43 ± 1.9
GRB 081121	2.512	160.8 ± 16.5	55.9 ± 2.8
GRB 081008	1.969	166.1 ± 36.3	132.4 ± 1.4
GRB 081007	0.530	–	5.8 ± 0.5
GRB 0809286	1.692	–	11.8 ± 0.5
GRB 080916C	4.350	662.1 ± 45.2	63.9 ± 0.3
GRB 080916A	0.689	107.4 ± 19.4	23.8 ± 1.2

Continued on next page

Table 2.7: Redshift, $E_{\rm peak}$ and T_{90} (all observer-frame) of the 47 GRBs used in this section.

GRB ID	**z**	$E_{\rm peak}$ **[keV]**	T_{90} **[s]**
GRB 080906	2.1	205.9 ± 37.6	81.9 ± 9.2
GRB 080905B	2.374	179.2 ± 59.9	100.5 ± 3.5
GRB 080905	0.122	313.1 ± 87.1	0.91 ± 0.02
GRB 080810	3.350	833.9 ± 124.9	102.6 ± 4.1
GRB 080804	2.205	218.0 ± 24.5	41.6 ± 1.2

Isotropic energy ($E_{\rm iso}$)

$E_{\rm iso}$ is calculated by

$$E_{\rm iso} = \frac{4\pi d_L^2}{1+z} S_\gamma, \tag{2.9}$$

where d_L is the luminosity distance and S_γ the fluence in the $1/(1+z)$ keV to $10/(1+z)$ MeV frame. I determined S_γ using the energy flux provided by the best-fit spectral parameters and multiplying it with the total time interval over which the fit was performed. Since I performed the fit for time intervals where the count rate exceeded a S/N ratio of 3.5, it happened that some time intervals of some bursts were not included in the fit (e.g. phases of quiescence where the count rate dropped back to the background level). These time intervals were not used to calculate the fluence.

2.3.3 Correlations

Amati relation

The "Amati relation" is shown in Fig. 2.18 for 40 GBM GRBs with measured $E_{\rm p,rest}$ and $E_{\rm iso}$. There is an evident correlation between these two quantities for long GRBs (Spearman's rank correlation of $\rho = 0.67$ with a chance probability of 1.73×10^{-5}). Using the bisector of an ordinary least-squares fit (bOLS), I found

$$E_{\rm p,rest} = 441^{+1840}_{-360} \times \left(\frac{E_{\rm iso}}{1.07 \times 10^{53}\,{\rm erg}} \right)^{0.55 \pm 0.05} \ {\rm keV} \tag{2.10}$$

which is in agreement with the indices obtained by e.g. Amati (2010); Ghirlanda et al. (2009, 2010) (errors refer to the 95 % CL). However, the extrinsic scatter is larger by a factor of ~ 2 in log-space compared to Amati (2010). This finding is consistent with Gruber et al. (2011b) and Virgili et al. (2011). As has been shown by other authors in the past (see e.g. Amati, 2010; Ghirlanda et al., 2009; Amati et al., 2008) short bursts do not follow the relation, being situated well outside the 2 σ scatter around the best-fit. This is true also for the power-law fit derived here (see Fig. 2.18) except for GRB 100816A and GRB 110731A. However, the former burst may actually fall in an intermediate or hybrid class of short GRBs with extended emission (see e.g. Norris and Bonnell, 2006; Zhang et al., 2009) while the latter is short only in the rest-frame.

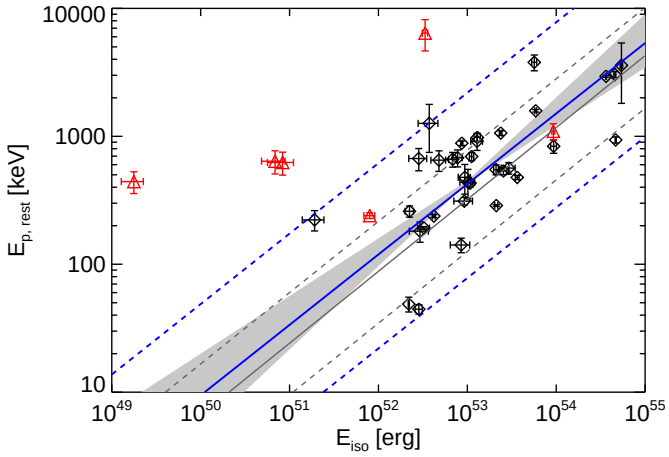

Figure 2.18 Amati relation for 6 short (red open triangles) and 34 long (black open diamonds) GBM GRBs. Also shown is the best power-law fit to the data (blue solid line), the extrinsic scatter (95% CL; blue dashed lines) and the intrinsic scatter using the errors of the fit parameters (95% CL, grey-shaded region). The best power-law fit published by Amati (2010) (light-grey solid line) with the 2σ scatter (light-grey dashed line) are also shown.

Yonetoku relation

L_p and the time resolved $E_{\rm p,rest}$ were calculated for the brightest 1024 ms and 0.064 ms time bin for long and short GRBs, respectively. I was able to determine the time resolved $E_{\rm p,rest}$ for 26 (5 short and 21 long) GRBs and I present this relation in Fig. 2.19. Using again a bOLS, omitting short GRB 080905A from the fit (see below), I found

$$E_{\rm p,rest} = 667^{+295}_{-310} \times \left(\frac{L_p}{4.97 \times 10^{53}\,{\rm erg\,s^{-1}}} \right)^{0.48\pm0.01} \quad {\rm keV}, \tag{2.11}$$

with the errors referring to the 68 % CL.

The Spearman's rank correlation gives $\rho = 0.8$ with a chance probability of 9×10^{-8}. My findings are in good agreement with Ghirlanda et al. (2009, 2010) and Yonetoku et al. (2004). I note that short GRB 080905A is a peculiar outlier to the Yonetoku relation. The redshift for this GRB was obtained via its claimed host galaxy at $z = 0.1218$ (Rowlinson et al., 2010), making it the closest short GRB to date. It could be that this GRB has some peculiar properties compared to other GRBs or that its redshift is wrong. (A redshift of $z \sim 0.9$ would make GRB 080905A consistent with the Yonetoku relation.)

$T_{90,\rm rest}$ vs redshift

I did not find any evidence in the GBM data for any dependence of $T_{90,\rm rest}$ on z. My results confirm the analysis with *Swift* detected GRBs (Greiner, 2011). However, several authors (e.g. Kocevski and Petrosian, 2011) reported that, due to the detector sensitivity the observed duration can actually decrease with increasing redshift as only the brightest portion of a high redshift GRB's light curve become accessible to the detector. Consequently, this would mean that probably all estimates of duration and subsequently energetics for high redshift GRBs are

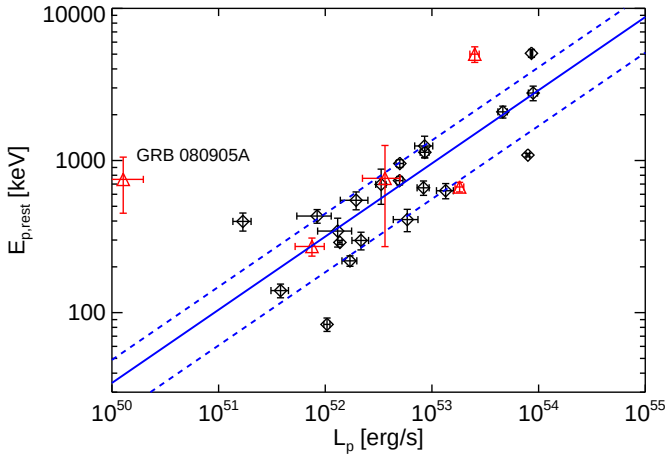

Figure 2.19 Yonetoku relation for 5 short (red open triangles) and 21 long (black open diamonds) GBM GRBs. Also shown is the best power-law fit to the data (blue solid line) together with the 1σ scatter (blue dashed line).

only lower limits to their true intrinsic values. Indeed, Pélangeon et al. (2008) found such a negative correlation between $T_{90,\mathrm{rest}}$ and z.

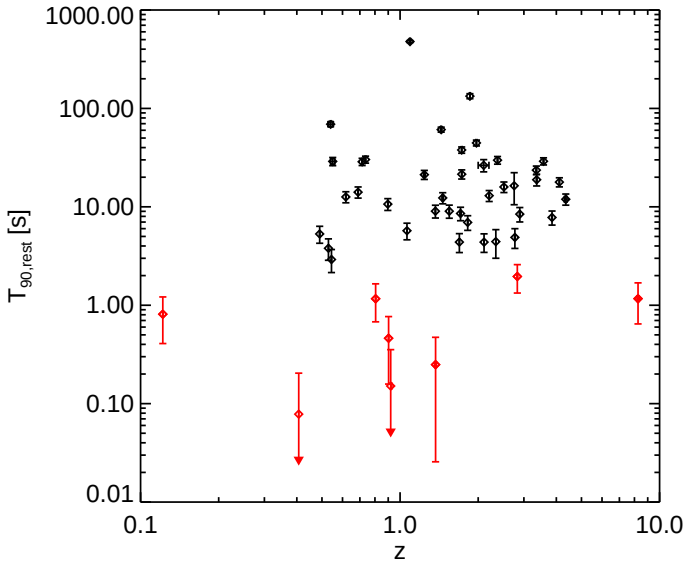

Figure 2.20 Testing the cosmic evolution of $T_{90,\mathrm{rest}}$. No correlation is evident.

$E_{\rm p,rest}$ vs redshift

In order to explain the detection rate of GRBs at high-z, Salvaterra and Chincarini (2007) concluded that high-z GRBs must be more common (e.g. Daigne et al., 2006; Wang and Dai, 2011) and/or intrinsically more luminous (Salvaterra et al., 2009) than bursts at low-z (but see Butler et al., 2010). As already mentioned above, Yonetoku et al. (2004) found a tight correlation between the 1-s peak-luminosity (L_p) and $E_{\rm p,rest}$ in GRBs. Assuming that the luminosity function of GRBs indeed evolves with redshift and that the Yonetoku relation is valid, I would also expect a positive correlation of $E_{\rm p,rest}$ with z.

In Fig. 2.21, I present $E_{\rm p,rest}$ vs z. As was shown in §2.3.2 and in Table 2.6, GBM can reliably measure $E_{\rm peak}$ down to ~ 15 keV. The solid line indicates this redshift-corrected lower limit. A Spearman's rank correlation test of $E_{\rm p,rest}$ and z, using only the long GRBs, resulted in $\rho = 0.67$ with a chance probability of $P = 1.3 \times 10^{-5}$. When including the short GRBs, the correlation coefficient effectively remained unchanged, whereas the chance probability increased to $P = 4 \times 10^{-3}$, making a correlation slightly less likely.

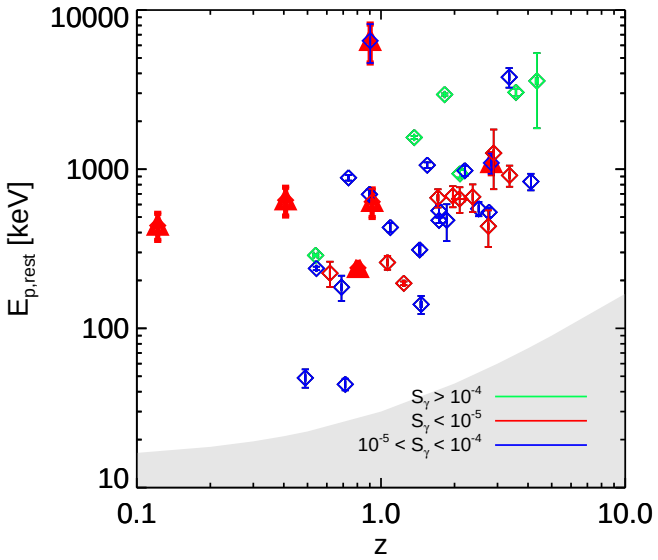

Figure 2.21 Testing the cosmic evolution of $E_{\rm p,rest}$ for long (diamonds) and short (triangles) GRBs. The grey-shaded region indicates the area of $E_{\rm p,rest}$ which cannot be probed by GBM. Bursts with high (green), intermediate (blue) and low (red) fluence (in erg cm^{-2}) are labeled.

However, this correlation can probably be explained entirely by selection effects: GRBs do not populate the empty area in Fig. 2.21 (low $E_{\rm p,rest}$ and $z > 1$) because they simply can not be detected by GBM. Even though GBM *could* recover a low $E_{\rm peak}$ value of such GRBs, as was shown above, the detection of such events is very challenging because of the low photon fluxes of these events. As one can see in Fig. 2.21 the lower boundary of the apparent correlation is composed of the bursts that have relatively low or intermediate fluence. This is already an indication that these events reside at the lower fluence limit for GBM to both trigger on these events.

In Gruber et al. (2011a) it was tested up to which maximum redshift, $z_{\rm max}$ the 32 bursts

of their sample could have been detected, i.e. for which GBM would have triggered. GBM has many trigger algorithms (various trigger time scales for various energy ranges). For the purpose of this test, they focussed on the 50 keV to 300 range which is the classical trigger energy range for a GRB and a timescale of a maximum of 4.096 s for long GRBs and 1.024 s for short GRBs. In order to shift a GRB to a higher redshift, three observables change:

1. The duration $T_{90}(z_{\max}) = T_{90}(z_0)\frac{1+z_{\max}}{1+z_0}$
2. The peak energy $E_{\rm p}(z_{\max}) = E_{\rm p}(z_0)\frac{1+z_0}{1+z_{\max}}$
3. The flux of the GRB.

While it was straightforward to account for the changes of $E_{\rm peak}$ and T_{90}, the proper treatment of the flux was more complex. RMFIT outputs the spectral parameters, including the normalization (N_0 in ph cm^{-2} s^{-1} keV^{-1}) of the spectrum, which can be recognized as a proxy for the flux of a GRB. Therefore, in order to decrease the flux when shifting the GRB to ever higher redshifts, the normalization has to be decreased accordingly. This was done as follows:

The photon luminosity of a GRB, in the energy band from E_1 to E_2 is defined as follows

$$L = 4\pi d_{L,z_0}^2 \int_{E_1/(1+z_0)}^{E_2/(1+z_0)} N_0 \Phi_1(E)\, dE, \tag{2.12}$$

where d_L is the luminosity distance and z_0 the redshift of the burst. The integral describes the photon flux of the burst in the E_1 to E_2 energy range at the rest-frame of the burst. N_0 is the normalization of the spectrum and $\Phi_1(E)$ is the shape of the spectrum (Band or COMP) with $E_p = E_p(z_0)$, i.e. $\Phi_2 = \Phi_2(E, E_p(z_0))$. The luminosity of a burst is independent of redshift. This, in turn, means that the above equation is valid also when exchanging z_0 with $z_{\max}$. One gets

$$L = 4\pi d_{L,z_{\max}}^2 \int_{E_1/(1+z_{\max})}^{E_2/(1+z_{\max})} N_{z_{\max}} \Phi_2(E)\, dE, \tag{2.13}$$

where $\Phi_2 = \Phi_2(E, E_p(z_{\max}))$.

Setting the two equations equal and solving for $N_{z_{\max}}$ one is left with

$$N_{z_{\max}} = N_0 \times \frac{d_{L,z_0}^2}{d_{L,z_{\max}}^2} \times \frac{\int_{E_1/(1+z_0)}^{E_2/(1+z_0)} \Phi_1(E, E_p(z_0))\, dE}{\int_{E_1/(1+z_{\max})}^{E_2/(1+z_{\max})} \Phi_2(E, E_p(z_{\max}))\, dE}. \tag{2.14}$$

It can be shown, for both the COMP model and the Band function, that the fraction of the two integrals is nothing else than

$$\frac{\int_{E_1/(1+z_0)}^{E_2/(1+z_0)} \Phi_1(E, E_p(z_0))\, dE}{\int_{E_1/(1+z_{\max})}^{E_2/(1+z_{\max})} \Phi_2(E, E_p(z_{\max}))\, dE} = \frac{(1+z_{\max})^{\alpha+1}}{(1+z)^{\alpha+1}}, \tag{2.15}$$

where α is the low-energy power law index.

Thus,

$$N_{z_{\max}} = N_0 \times \frac{d_{L,z_0}^2}{d_{L,z_{\max}}^2} \times \frac{(1+z_{\max})^{\alpha+1}}{(1+z)^{\alpha+1}}. \tag{2.16}$$

For GBM to trigger, two detectors need to be above the trigger threshold. Therefore, real background information of the second brightest detector of every burst was used. With this

background data, each bursts was shifted in steps of $\Delta z = 0.25$ to higher redshifts and 1000 bursts were simulated for each redshift step (changing the source lifetime, input $E_{\rm peak}$ and normalization as described above, additionally adding Poissonian noise to the best-fit parameters) by forward folding the photon model through the detector response matrix, created at the time and location of the real GRBs. To determine if GBM would have triggered, the signal-to-noise ratio (SNR) was determined with

$$\mathrm{SNR} = \frac{\Delta \mathrm{t} \cdot \mathrm{c_s} - \Delta \mathrm{t} \cdot \mathrm{c_b}}{\sqrt{\Delta \mathrm{t} \cdot \mathrm{c_b}}}, \tag{2.17}$$

where, Δt is the trigger time scale ($\Delta t = 4.096$ s for long GRBs and $\Delta t = 1.024$ s for short GRBs), c_s and c_b are the counts/s of the source and background, respectively. If more than 90% of the simulated bursts have SNR ≥ 4.5 it can safely be assumed that the burst would have been detected at this redshift. I plot $E_{\rm p,rest}$, which obviously remains constant at all redshifts, vs the range of the actually measured to maximum redshift in Fig. 2.22. I already know that the here presented sample of GRBs is representative of all bursts detected by GBM (see §2.3.2). Therefore, I note that the determination of the lowest measurable $E_{\rm peak}$ value is not as crucial as the determination of the detector sensitivity. None of the bursts in my sample populates the empty region at $2 \leq z \leq 8$ and $50 \leq E_{p,\rm rest}$ [keV] ≤ 500 even when shifting them at their maximum detectable redshift. I conclude that most of the correlation between $E_{\rm p,rest}$ and z can be explained by the sensitivity limitations of the instrument.

2.3.4 Conclusions

GBM observed 47 bursts which have a measured redshift. For this sample, I performed a rest-frame study, focusing on both the temporal and spectral properties, as well as on intra-parameter relations within these quantities. In addition, I investigated for possible biases in the $E_{\rm peak}$ distribution of the full GBM-GRB sample, finding that (i) GBM can reliably measure $E_{\rm peak}$ down to ~ 15 keV and (ii) there is no population of high-$E_{\rm peak}$ GRBs.

A first important finding is that the width of the $E_{\rm p,rest}$ distribution is, in fact, not close to zero. Such a claim has recently been brought forward by Collazzi et al. (2011) who argued that all GRBs are thermostated and thus, have the same $E_{\rm p,rest}$. If true, this would require an unknown physical mechanism that holds GRBs at a constant $E_{\rm p,rest}$ value. However, it could be shown here that such a mechanism is not required because our sample has an $E_{\rm p,rest}$ distribution that ranges over several decades in energy.

I confirm the $E_{\rm p,rest}$- $E_{\rm iso}$ correlation and find a power law index of 0.55, consistent with the values reported in the literature but with a significantly larger scatter around the best-fit. I also confirm a strong correlation between the peak luminosity of the burst and its $E_{\rm p,rest}$ with a best-fit power law index of 0.57. I looked for additional correlations between the parameters. Although there is no observed redshift evolution of $T_{90,\rm rest}$, there might be some indication that $E_{\rm p,rest}$ of long GRBs is higher at higher redshifts. This result, although not completely unexpected from theoretical considerations is, however, heavily influenced by selection effects which need to be taken properly into account before making any conclusive statement about this effect.

I also find that short GRB 080905A is a striking outlier to the Yonetoku relation. This might be due to the fact that it is a GRB with peculiar properties compared to other long and short GRBs, or because the identified redshift is wrong.

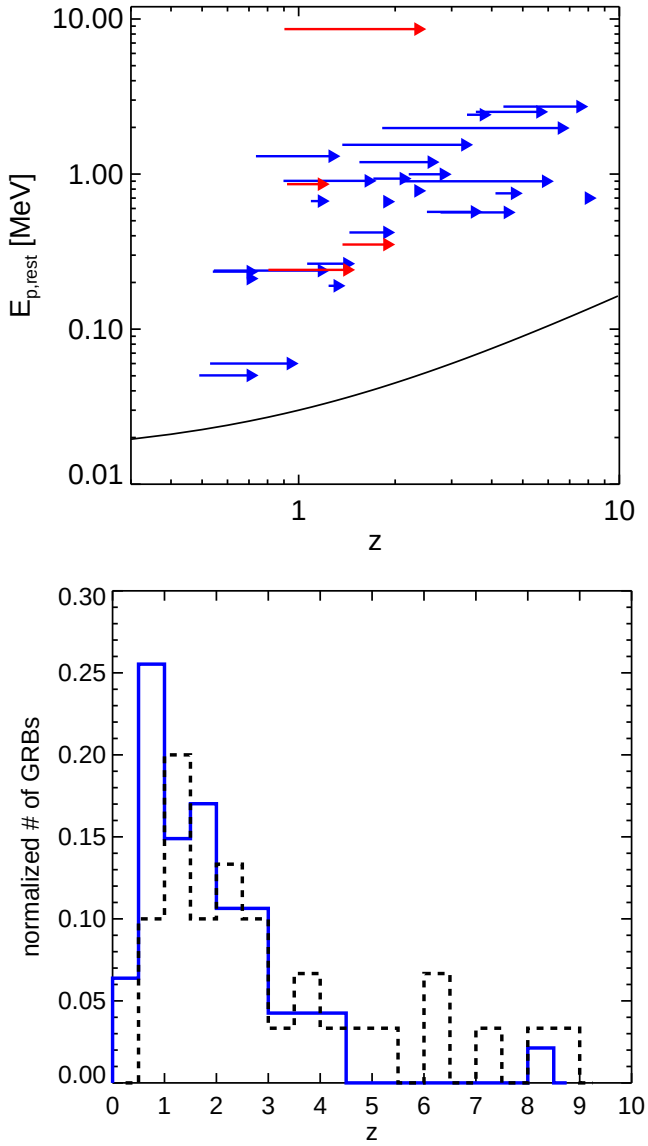

Figure 2.22 *Upper panel:* Same as Fig. 2.21 but with a line indicating the maximum possible redshift, $z_{\rm max}$ that these 30 GRBs can have to still be detectable by GBM. *Lower panel:* Observed redshift distribution of GBM detected GRBs (blue solid histogram) and redshift distribution of these GRBs at their maximum detectable redshift (black dashed histogram).

Table 2.6 Mean and standard deviation of the output spectral parameters of the simulated bursts.

t_S	$E_{\rm p,in}$	f	$E_{\rm p,out}$	α_{out}	rej
10	15	10	$15.0^{+1.5}_{-1.4}$	-1.53 ± 0.36	98
100	15	1	$21.7^{+4.0}_{-3.4}$	-1.55 ± 0.16	99
100	15	3	$15.4^{+1.9}_{-1.7}$	-1.39 ± 0.30	92
100	15	10	$14.1^{+0.5}_{-0.5}$	-0.79 ± 0.16	46
1	17	3	$22.6^{+3.2}_{-2.8}$	-1.48 ± 0.25	96
1	17	10	$23.5^{+4.8}_{-4.0}$	-1.48 ± 0.20	97
5	17	3	$25.8^{+5.8}_{-4.7}$	-1.49 ± 0.18	99
5	17	10	$18.2^{+2.4}_{-2.1}$	-1.44 ± 0.23	88
10	17	3	$21.2^{+6.5}_{-5.0}$	-1.55 ± 0.17	93
10	17	10	$17.6^{+1.7}_{-1.6}$	-1.26 ± 0.27	79
100	17	1	$22.5^{+2.1}_{-1.9}$	-1.33 ± 0.23	96
100	17	3	$16.9^{+1.7}_{-1.6}$	-1.28 ± 0.25	39
100	17	10	$17.0^{+0.4}_{-0.4}$	-0.80 ± 0.12	0
1	25	10	$30.6^{+5.1}_{-4.4}$	-1.30 ± 0.28	86
5	25	3	$33.9^{+6.8}_{-5.6}$	-1.44 ± 0.24	96
5	25	10	$26.2^{+2.0}_{-1.9}$	-0.92 ± 0.29	39
10	25	3	$30.3^{+4.4}_{-3.8}$	-1.29 ± 0.27	80
10	25	10	$25.4^{+1.7}_{-1.6}$	-0.89 ± 0.25	4
100	25	1	$29.4^{+3.7}_{-3.3}$	-1.24 ± 0.27	73
100	25	3	$25.3^{+1.6}_{-1.5}$	-0.85 ± 0.24	1
100	25	10	$25.1^{+0.6}_{-0.6}$	-0.82 ± 0.11	0
1	50	10	$53.3^{+8.4}_{-7.2}$	-0.88 ± 0.28	52
5	50	3	$57.1^{+9.0}_{-7.8}$	-0.96 ± 0.27	62
5	50	10	$49.9^{+5.8}_{-5.2}$	-0.78 ± 0.22	0
10	50	3	$51.9^{+7.3}_{-6.4}$	-0.82 ± 0.29	37
10	50	10	$50.0^{+4.1}_{-3.8}$	-0.78 ± 0.16	0
100	50	1	$50.3^{+7.2}_{-6.3}$	-0.80 ± 0.28	21
100	50	3	$49.9^{+3.5}_{-3.3}$	-0.78 ± 0.14	0
100	50	10	$50.0^{+1.3}_{-1.3}$	-0.80 ± 0.05	0
1	100	3	$121.0^{+5.4}_{-5.2}$	-0.82 ± 0.13	99
1	100	10	$92.0^{+18.9}_{-15.7}$	-0.71 ± 0.25	16
5	100	3	$98.7^{+21.5}_{-17.7}$	-0.74 ± 0.26	21
5	100	10	$98.6^{+11.2}_{-10.1}$	-0.78 ± 0.13	0
10	100	3	$95.0^{+19.3}_{-16.0}$	-0.73 ± 0.23	4
10	100	10	$99.0^{+8.4}_{-7.7}$	-0.79 ± 0.09	0
100	100	1	$92.4^{+17.3}_{-14.6}$	-0.71 ± 0.23	8
100	100	3	$99.9^{+7.1}_{-6.6}$	-0.80 ± 0.08	0
100	100	10	$99.9^{+2.4}_{-2.4}$	-0.80 ± 0.03	0

2.4 Untriggered *Swift*-GRBs in GBM data[g]

2.4.1 Introduction

Motivated by the pursuit of faint Gamma-Ray Bursts (e.g. the elusive class of postulated low-luminosity GRBs), here I present the preliminary results of an on-ground search in CTIME data for GRBs which were detected by the *Swift* satellite but did not trigger GBM, although having a favorable orientation to the GBM detectors. To this end, I will demonstrate the methods and algorithms which have been developed by the GBM team. The spectral properties of these GRBs are then compared to the full sample of GBM GRBs published in the GBM spectral catalogue.

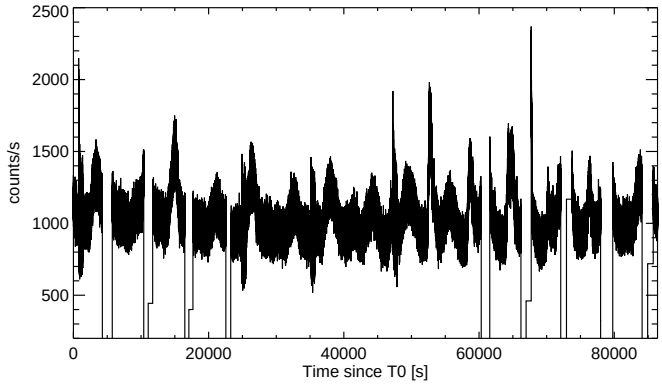

Figure 2.23 Typical CTIME light curve of one NaI detector over a full day in the energy interval from $10-1000$ keV. One can clearly identify the overall background variations and SAA passages during which the detectors are switched-off.

2.4.2 Methods

From 2008 August 22 to 2012 January 06, *Swift* observed 299 GRBs[h]. 107 (36 %) of these also triggered GBM. 30 (10%) *Swift*-GRBs happened while GBM was flying through the South Atlantic Anomaly (SAA) during which the high-voltage of the detectors is switched off. 88 (29%) of the GRBs were either shadowed by the Earth when they triggered *Swift* or had source angles to all detectors which were larger than 60°, making a GBM detection unlikely because of the rapidly dropping effective area of the NaI detectors at such high incidence angles. Using these geometrical and orientational arguments, the remaining 74 (25%) *Swift*-GRBs could have been observed by GBM.

The newly developed on-ground trigger algorithm looks for these GRBs by employing a routine which is similar to the FSW. For a trigger, an excess count rate (above background) in CTIME data in two detectors must be observed with a statistical significance of 4σ and 3.8σ, respectively. The search is restricted to the energy range between $50-300$ keV which is the energy range in which GRBs typically trigger GBM (Paciesas et al., 2012). The trigger time

[g]The main part of this work has been published by Gruber and for the Fermi/GBM collaboration (2012b) in "Gamma-Ray Bursts 2012", Munich, May 7–11, 2012, eds. A. Rau and J. Greiner, PoS(GRB 2012)036 entitled *Untriggered* Swift-*GRBs in* Fermi*/GBM data*

[h]`http://swift.gsfc.nasa.gov/docs/swift/archive/grb_table.html/`

scales vary from 0.256 s to 8.192 s. The greatest advantage, compared to the FSW triggering, comes from the fact that the background can be handled better on-ground because I have knowledge about the background variation over the whole day which is simply modeled using a spline function. In addition to this, the rise and set times of 92 known γ-ray sources over the Earth's horizon with respect to GBM are calculated. Usually, these rises/sets result in an abrupt change in count rate in the NaI detectors, best described as "occultation steps" (Wilson-Hodge et al., 2012). In order to account for this effect in the NaI detectors, the source's photon spectrum is used which is then folded through the detector response to calculate the expected change in count rate.

2.4.3 Conclusions

17 untriggered GRBs (1 short and 16 long) were identified (see Table 2.8). A spectral analysis of all the long GRBs, using CSPEC data, was performed. The model selection comprised a simple power law (PL), a power law with an exponential cutoff (COMP) and the Band function (BAND). The spectral analysis reveals no fundamental differences or peculiarities (see Fig. 2.24) compared to the full GBM-GRB sample Goldstein et al. (2012). As is expected, these events are populating the lower end of the photon flux distribution with fluxes ranging between $0.6 - 1.5$ ph cm^{-2} s^{-1} in the $10 - 1000$ keV energy range. Along with being faint, most of the events are also relatively soft, having $E_{\rm peak}$ values which are located at the lower tail of the $E_{\rm peak}$ distribution of the complete GBM-GRB sample Goldstein et al. (2012). No spectral analysis could be performed for the short GRB 090305A (time resolution of CSPEC data is too long compared to the actual duration, $T_{90} \sim 0.3$ s, of the GRB). The remaining 57 events which could have been detected by GBM (see Section 2.4.2) are probably to weak to be seen in GBM and are only observed by *Swift* due to its better sensitivity.

Considering that the Field-of-View (FoV) of *Swift* is roughly 4 times smaller than GBM's FoV, one can estimate that the GBM on-board trigger algorithm misses ~ 1.6 GRBs per month.

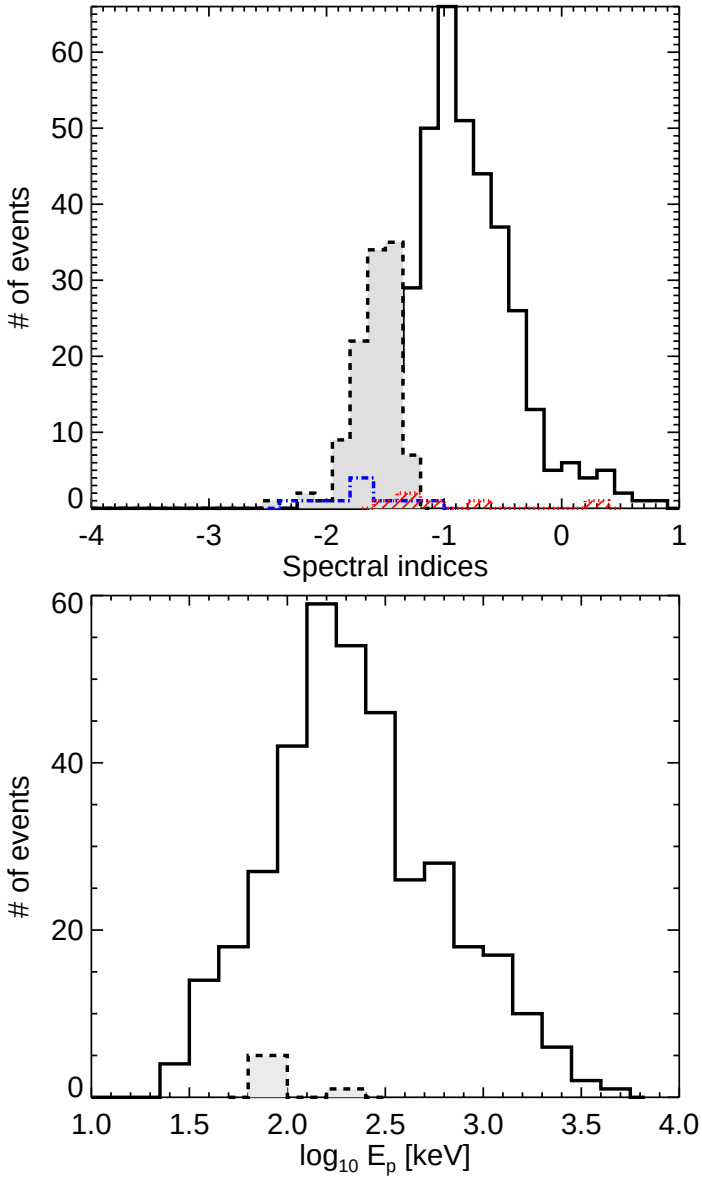

Figure 2.24 *Upper panel:* Distribution of the low-energy power-law indices. The index of the PL model for the untriggered sample (blue dash-dotted histogram) and all GBM-GRBs (light-grey dashed histogram). The histogram for COMP and Band model for the untriggered sample (red hatched histogram) and the full GBM-GRB sample (black solid histogram) are indicated. *Lower panel:* Distribution of the $E_{\rm peak}$ values for the 6 bursts which were fitted by COMP or Band for the untriggered sample (light-grey dashed histogram) and the full GBM-GRB sample (black solid histogram). The values for all triggered GBM-GRBs are taken from Goldstein et al. (2012).

GRB ID	model	$E_{\rm peak}$ [keV]	α	β	flux [ph cm^{-2} s^{-1}]
111212A	PL	–	-1.62 ± 0.04	–	0.78 ± 0.04
110801A	PL	–	-1.61 ± 0.04	–	1.10 ± 0.04
	PL	–	-1.86 ± 0.07	–	1.07 ± 0.06
110719A	COMP	73.5 ± 5.0	$+0.36 \pm 0.30$	–	0.63 ± 0.04
110414A	BAND	67.8 ± 8.8	-0.66 ± 0.21	-2.23 ± 0.2	0.86 ± 0.03
110411A	COMP	64.2 ± 5.3	-1.29 ± 0.11	–	1.04 ± 0.03
110315A	COMP	66.5 ± 8.9	-1.58 ± 0.10	–	1.28 ± 0.04
110312A	PL	–	-2.35 ± 0.11	–	0.89 ± 0.06
100902A	COMP	94.9 ± 17.2	-1.31 ± 0.14	–	0.73 ± 0.03
100305A	PL	–	-1.25 ± 0.07	–	0.79 ± 0.07
091029A	PL	–	-1.83 ± 0.04	–	1.51 ± 0.05
090728A	PL	–	-1.60 ± 0.05	–	1.12 ± 0.06
090520A	PL	–	-1.14 ± 0.08	–	0.74 ± 0.08
090404A	PL	–	-2.20 ± 0.05	–	1.31 ± 0.05
090305AS	–	–	–	–	–
090123A	PL	–	-1.68 ± 0.04	–	0.73 ± 0.03
080906A	COMP	244.0 ± 48.0	-1.19 ± 0.10	–	0.92 ± 0.04
080916B	PL	–	-1.55 ± 0.12	–	0.95 ± 0.15

Table 2.8 *Swift*-GRBs found in untriggered GBM data. The results of the spectral analysis, peak energy $E_{\rm peak}$, low-energy power law index α, high-energy power law index β and photon flux, are shown. Please note that GRB 110801A was a very long GRB with two distinctive emission episodes and that a spectral fit was not possible for short GRB 090305A.

Chapter 3

Solar flares

3.1 Introduction

Solar flares are the most energetic events in our Solar System, releasing up to $\sim 10^{32}$ erg on timescales from a few to tens of minutes. Using the most simplistic terms, solar flares are defined as enormous explosion on the surface of the Sun which can accelerate particles (protons, neutrons electrons, ions) to enormous speeds. The common consensus is that solar flares are the result from a sudden release of energy which is stored in the magnetic fields around active regions of the Sun (indicated by sunspots), which vary according to the well known 11-year activity cycle of the Sun.

Solar flares were first discovered in the optical region by Carrington (1859) who observed sunspots when a solar flare erupted. After that, thanks to to the fast improvement of measurement techniques, solar flares were quickly observed all across the electromagnetic spectrum. The first radio and X-ray observations of solar flares were obtained in the first half of the 20th century by Dellinger (1935); Hey et al. (1948) and Friedman et al. (1951), respectively. These measurements were soon followed by observations in the γ-ray regime by Peterson and Winckler (1959) and Chupp et al. (1973). Today, solar flares are classified according to their $1-8$ $\mathring{A}$ energy flux observed by the Geostationary Operational Environmental Satellites (GOES) in 5 major classes (see Table 3.1 and Fig. 3.1).

GOES class	$1-8$ $\mathring{A}$ peak [W/m^2]	events/year max/min
A	$> 10^{-8}$	$--$
B	$> 10^{-7}$	$--$
C	$> 10^{-6}$	$> 2000/300$
M	$> 10^{-5}$	300/20
X	$> 10^{-4}$	10/1
$--$	$> 10^{-3}$	few?/none?

Table 3.1 Solar flare classification. (Vogel, 2012)

Solar flares release their energy in three different phases (Fig. 3.2 shows all these signatures across the whole electromagnetic spectrum):

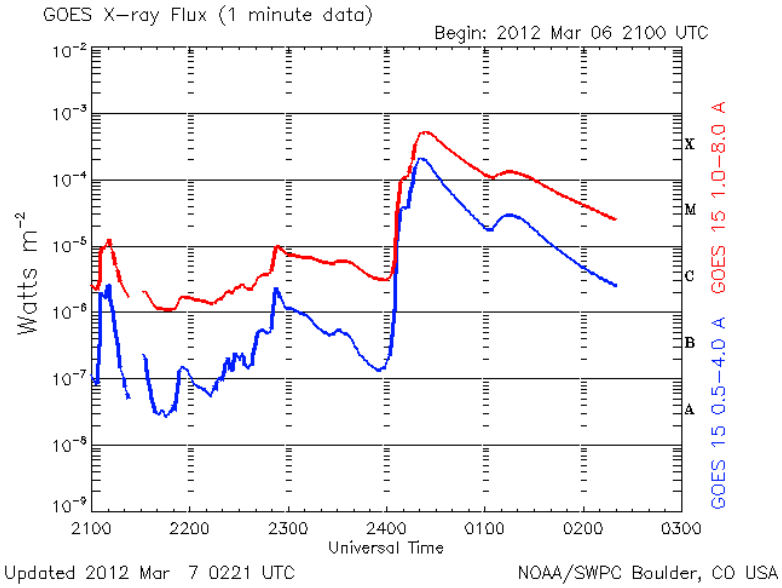

Figure 3.1 X-ray data of the GOES satellite. The data show the $0.5-4$ $\mathring{A}$ (blue solid line) and the $1.0-8.0$ $\mathring{A}$ (red solid line) energy flux of the Sun for March 6th, 2012. An X5 class solar flare was observed on March 7th, 2012 at $\sim$ 00:20 UT which was followed by a less intense X1 class flare at $\sim$ 01:10 UT. [Figure taken from the Space Weather prediction Center at `www.swpc.noaa.gov`]

(i) the "pre-flare stage" in which the soft X-ray emission gradually rises, but little or no X- or γ-rays are observed,

(ii) the "impulsive" phase, where a burst of intense γ-rays is observed on timescales of a few seconds with several emission spikes, showing strong non-thermal effects. Finally,

(iii) the "gradual phase" where the γ-rays decay exponentially and cease to exist whereas the soft X-ray component continues to rise peaking several hours after the impulsive phase.

For obvious reasons, the most interesting of the above phases for GBM is the impulsive phase. During this phase the spectrum in the GBM and LAT energy range of the most interesting solar flares shows a superposition of various physical components such as e.g. bremsstrahlung radiation, γ-ray line emission (which arise from nuclear interactions of accelerated protons or heavier ions with the ambient solar medium. These nuclear de-excitation lines have been observed for nitrogen, carbon and oxygen and using their relative fluxes it is possible to infer the composition of the accelerated particles and the target nuclei on the Sun), accelerated neutrons (which produce the so called "neutron capture" line at 2.23 MeV when captured by the protons to form the heavier deuteron), the positron annihilation line at 511 keV and even pion-decay emission can observed in rare cases (e.g. Ackermann et al., 2012). Fig. 3.3 shows a photon spectrum for an M2 soft X-ray solar flare observed by the GBM and LAT on June 12, 2010 where all these model components can be identified easily.

In the following, I am going to present recent results which were obtained by performing an extensive timing analysis on the impulsive solar flare phase of four solar flares observed by GBM in §3.2. In §3.3, I will show a new method to estimate the background rates in GBM for very long solar flares where the standard data reduction fails.

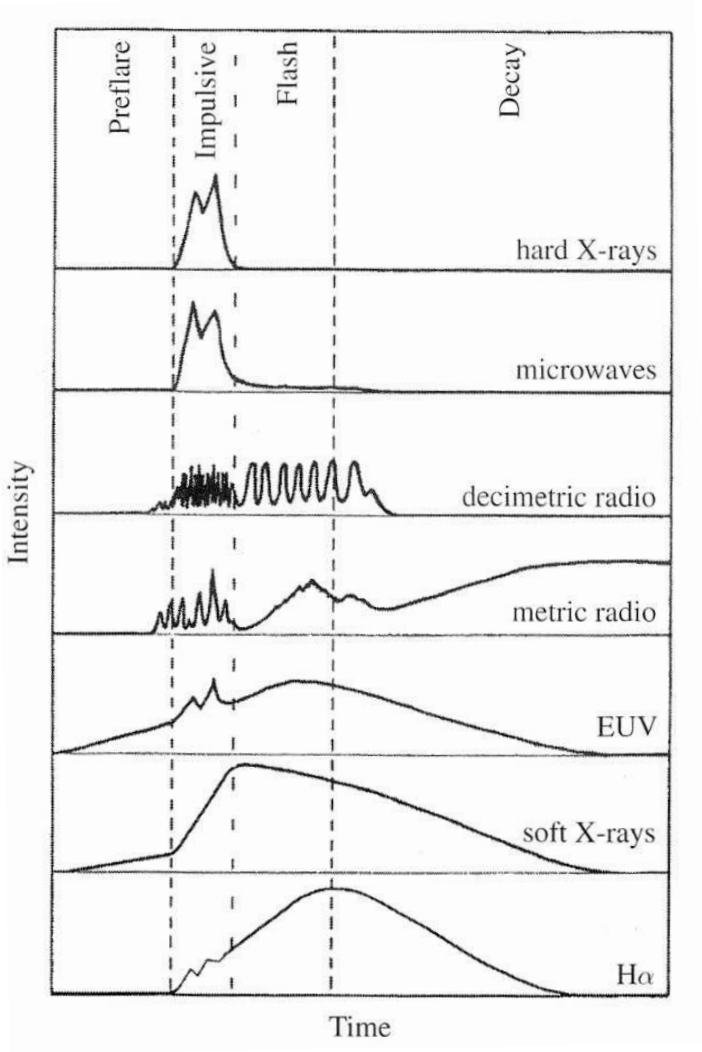

Figure 3.2 Evolution of solar flare emission in different wavelengths (Figure taken from Benz, 2002; Vogel, 2012).

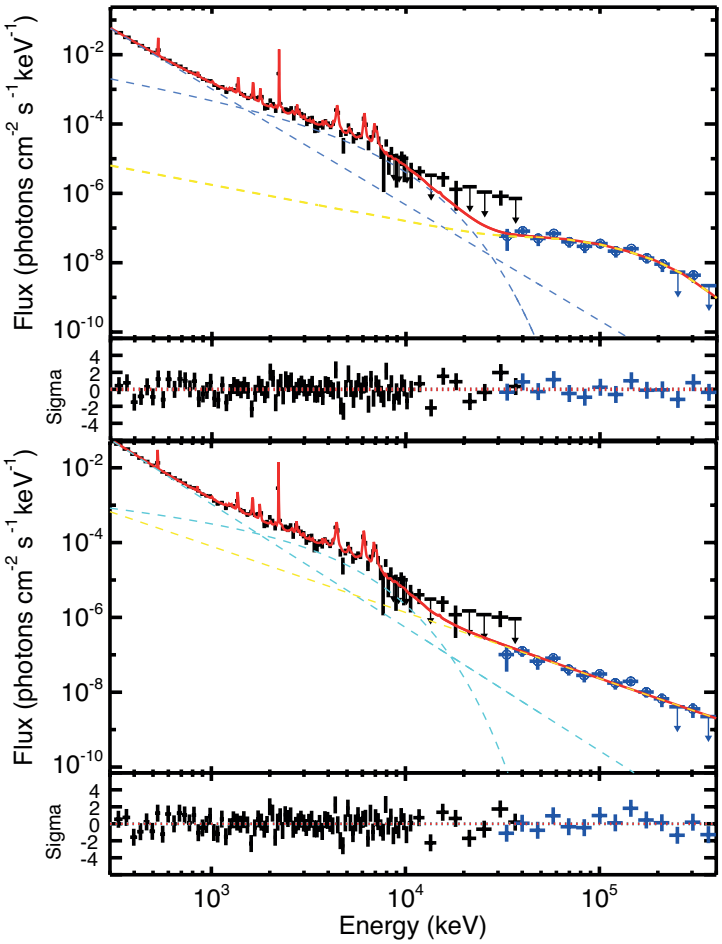

Figure 3.3 Combined GBM (black crosses) and LAT (blue open circles) photon spectrum showing the best total fit (red solid line) to the M2 soft X-ray solar flare observed on 2010 June 12. For the fit, a simple power law model (blue dashed line), a flatter power law with exponential cutoff (cyan dashed line) to model bremsstrahlung by electrons, a nuclear de-excitation component plus 0.511 and 2.223 MeV lines (model components omitted for clarity) were used. The upper panel uses a pion-decay (dashed orange line) component to fit the LAT data whereas the lower panel uses a third power law fit which represents a third electron bremsstrahlung component. (Ackermann et al., 2012, Figure and parts of the caption taken from).

3.2 Quasi-periodic pulsations in solar flares: new clues from the *Fermi* Gamma-Ray Burst Monitor:[a]

3.2.1 Introduction

Over the past 40 years, quasi-periodic pulsations (QPP) in solar flares have been reported from observations across the electromagnetic spectrum, i.e. from radio waves to the highly energetic γ-rays, on timescales from sub-second intervals up to several minutes (e.g. Parks and Winckler, 1969; Ofman and Sui, 2006; Li and Gan, 2008; Nakariakov and Melnikov, 2009; Nakariakov et al., 2010a). While there seems to be an overwhelming amount of observational data, the underlying physical mechanism that could generate such QPPs still remains a mystery. Possible processes that are considered are modulation of electron dynamics by magnetohydrodynamic (MHD) oscillations (Zaitsev and Stepanov, 1982), periodic triggering of energy releases by MHD waves (Foullon et al., 2005; Nakariakov et al., 2006), MHD flow overstabilities (Ofman and Sui, 2006), and oscillatory regimes of magnetic reconnection (Kliem et al., 2000).

The analysis and interpretation of the power spectral density (PSD) of solar flares is, in general, difficult. A variety of astrophysical sources (such as X-ray binaries, Seyfert galaxies (e.g. Lawrence et al., 1987; Markowitz et al., 2003) and GRBs (Ukwatta et al., 2009; Cenko et al., 2010), show erratic, aperiodic brightness changes. Solar flares exhibit similar aperiodic variations with the general time profile being a sharp impulsive phase followed by a slower decay phase. Solar flares, together with many other astrophysical sources, thus have very steep power spectra in the low-frequency region. This type of variability is known as red-noise (e.g. Groth, 1975; Deeter and Boynton, 1982; Israel and Stella, 1996; Vaughan, 2005). When determining the significance of possible periodicities in the PSD, the red-noise has to be accounted for in order not to severely overestimate the significance of identified frequencies (Lachowicz et al., 2009). In this chapter, I account for the red-noise properties when performing a periodogram analysis.

This chapter is organized as follows. In §3.2.2, I briefly present the methodology of the time-series analysis. I provide an overview of the red-noise properties in astrophysical sources and demonstrate the importance of the red-noise when estimating significances. In §3.2.3, I present the light curves and periodograms of solar flares that were observed by GBM. Finally, in §3.2.4, I summarize this study and present the conclusions.

3.2.2 Analysis of data governed by red-noise

As already pointed out by Mandelbrot and Wallis (1969) and Press (1978), the human eye has a tendency to identify periodicities from purely random time series, i.e. where sinusoidal variations are not statistically real. According to Press (1978), the strongest eye-apparent period in (actually non-periodic) data will be about one-third the length of the data sample. According to these authors "three-cycle" quasiperiods should be taken with a grain of salt.

Solar flares fall into the group of astrophysical sources whose red-noise is important. Red-noise has nothing to do with measurement errors or the systematics of the detectors, which are also called noise. Red-noise is an *intrinsic* property of the observed source and is due to erratic, aperiodic brightness changes. In contrast to white noise, which displays a flat spectrum in a PSD, i.e. is power independent of frequency, red-noise is characterized by a power law of the form

[a]The main part of this work has been published in Gruber et. al (2011), *Astronomy & Astrophysics*, 528, 15 entitled *Quasi-periodic pulsations in solar flares: new clues from the* Fermi *Gamma-Ray Burst Monitor*

of $P = Nf^{-\alpha}$. As a first order approximation, red-noise is the realization of a linear stochastic and weakly non-stationary process. This red-noise component makes the interpretation of the significance of a peak in the PSD more complex.

One way to estimate the significance of induced frequencies on top of an underlying red-noise continuum in a PSD, was presented by Vaughan (2005).

In short, Vaughan suggests calculating the periodogram normalized so that the units of power are $(\text{rms/mean})^2\text{Hz}^{-1}$ (e.g. Schuster, 1898; Press and Rybicki, 1989). Then, the periodogram is converted to log-space in both frequency and power. For such a log-periodogram, one can then clearly identify the power-law component in the low-frequency range and a "cutoff" where white noise or an additional noise component takes over (e.g. Ukwatta et al., 2009). One can easily determine the power-law parameters by fitting a linear function to the low-frequency periodogram bins using the least squares method. In this chapter, the method of Vaughan (2005) was slightly modified in that I use a broken power law (BPL) to fit the PSD instead of a single power law.

Red-noise simulation

It is common practice (Inglis et al., 2008; Nakariakov et al., 2010a) to suppress the low-frequency component by de-trending the light curves of solar flares. This can be achieved by smoothing the light curve with a moving average or by applying a Gaussian filter and performing the periodogram analysis on the residual emission, i.e. the smoothed version is subtracted from the original data-set. This can give rise to misleading results as I show in the following.

By randomizing the phase as well as the amplitudes, Timmer and Koenig (1995) introduced an algorithm to generate a purely random time series that displays a $1/f^{\alpha}$ dependence in the PSD. I created a time series consisting of 200 data points, evenly spaced by 1 s with a $f^{-1.8}$ periodogram shape. From this light curve, I subtracted a simple moving average of 50 s (see Fig. 3.4). I then calculated the PSD (Lomb, 1976; Scargle, 1982; Press and Rybicki, 1989) of the residuals. The result is remarkable. Although I started with a purely random, red-noise dominated time-series, I obtained a PSD with three frequencies whose power exceeds the 3σ confidence limit (calculated according to Scargle 1982). This approach in signal processing clearly returned false-positive frequencies with periods of $P \approx 33$ s, $P \approx 55$ s, and $P \approx 100$ s, respectively. However, the spectral peaks remained well below the 3σ threshold if the periodogram was calculated using the method introduced by Vaughan (2005).

Therefore, shown by the example above, I strongly discourage subtracting smoothed versions of raw light curves when looking for intrinsic frequencies in the red-noise dominated PSD.

Detour: QPPs in GRBs

The same procedure of light curve reprocessing with a subsequent PSD analysis has also been applied to GRBs. In 2009, the *Swift* satellite observed GRB 090709A (Morris et al., 2009). Soon after this detection, Markwardt et al. (2009) claimed that the GRB had displayed very unusual behavior, not observed in any other GRB so far, namely a QPP-like behavior with a periodicity of $P \approx 8.1$ s at the 12σ level of significance. This QPP was subsequently confirmed and found to be in phase with the data of the Anti-Coincidence System (ACS) of the spectrometer SPI on board the INTEGRAL satellite (Götz et al., 2009), the Konus-WIND instrument (Golenetskii et al., 2009), and the Suzaku Wide-band All-sky Monitor (WAM) (Ohno et al., 2009). These latter instruments operate in the energy ranges 80 keV-10 MeV, 20 keV-1150 keV, and 50 keV-5 MeV, respectively. In contrast, *Swift*/BAT is sensitive to the energy range 15 keV-150 keV.

However, soon thereafter, Cenko et al. (2010) showed that the interpretation of this QPP

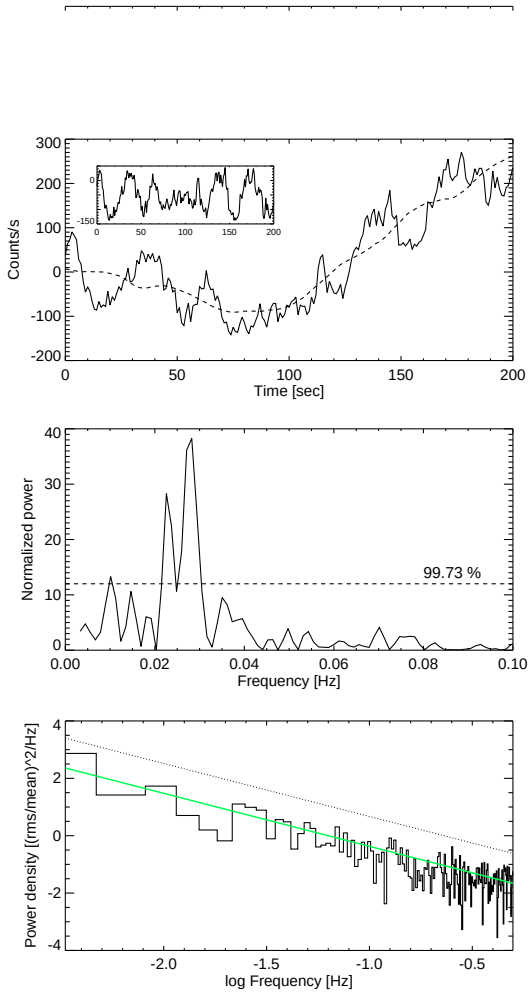

Figure 3.4 *Upper panel:* Synthetic red-noise time series with a power law index of $\alpha = -1.8$. Simple (boxcar) moving average is over-plotted (dashed line). The inset presents the residual signal. *Middle panel:* Lomb-Scargle Periodogram of the residual light curve. The 3σ CL has been denoted by a dashed line. *Lower panel:* PSD with the best fit power law (solid green line) and the 3σ significance level (dotted line).

depends strongly on the assumptions made about the underlying continuum. If the latter is accounted for, the significance of the claimed periodicity drops below the 3σ confidence limit. This analysis was independently repeated by Iwakiri et al. (2010) and de Luca et al. (2010), who also took into account the red-noise component in the PSD, and only found a marginally significant periodicity at the 3σ confidence limit.

In conclusion to this detour, I emphasize once more the importance of accounting for the red-noise component in the PSD. In addition, I highlight that a potential quasi-periodic signal is not necessarily significant even if it is identified in several instruments with different (but overlapping) energy ranges and observed to be in phase across these bands.

Method testing

The Reuven Ramaty High-Energy Solar Spectroscopic Imager (RHESSI, Lin et al. 2002) rotates about its spin axis which is always directed towards the Sun. The period of this rotation is $P \approx 4$ s and a PSD analysis of the RHESSI light curves is expected to detect this instrumental signal. I applied the Vaughan (2005) test to a solar flare that was observed by RHESSI on January 1st, 2005 and where QPPs have been reported (Nakariakov et al., 2010a). This solar flare peaked at 00:31 UT at a GOES level X1.7, from the NOAA active region 10715 located on disk at N03E47. I used RHESSI data in the energy range 50 keV-100 keV and a fine time resolution of 0.1 s (see upper panel of Fig. 3.5) and performed two periodogram analyses on this light curve in the range between 1660 s and 1820 s. The first periodogram analysis was performed using the classical approach introduced by Lomb (1976) and Scargle (1982). As commonly performed in the past (e.g. Inglis and Nakariakov, 2009), a periodogram was calculated on the residual emission after a simple moving average of 50 s was subtracted from the raw data (see middle panel of Fig. 3.5). With this method, several peaks were found above the 3σ threshold. The peak with the highest value of normalized power is located at $f \sim 0.025$ Hz, corresponding to the periodicity reported by Nakariakov et al. (2010a). Another peak worth mentioning is located at $f \sim 0.24$ Hz, which is the expected rotational frequency of RHESSI around its spin axis.

As I now demonstrate, the significance of the peak at $f \sim 0.025$ Hz is highly overestimated by the latter method. I show a PSD that was calculated using the raw and undetrended light curve applying the technique by Vaughan (2005) in the bottom panel of Fig. 3.5. In analogy to the Lomb and Scargle periodogram analysis, I found a significant spectral feature at ≈ 0.24 Hz, which is the expected rotation period of the RHESSI instrument. However, this PSD is lacking any other frequency above the 3σ confidence limit. The discrepancy between the two methods is easily explained. Firstly, the whole raw light curve was used without performing any artificially detrending beforehand. Secondly, the method of Lomb and Scargle assumes a white noise continuum and does not take into consideration the red noise component of the solar flare. However, the latter is taken into account by the method of Vaughan. In conclusion, I could not confirm the reported QPP in this solar flare. I am I confident that this latter method can be used for the subsequent analysis because I believe that it is more appropriate for sources that are dominated by red-noise and for which the inherent rotational frequency of the instrument is found to be significant.

An additional check was performed using SPI-ACS data of the outburst of SGR 1806-20 observed on 2004 December 27 in the energy range from 80 keV to 8 MeV (Mereghetti et al., 2005). SGR 1806-20 is known to have a rotational period of 7.56 s and the methodology adopted here should be able to recovered this periodicity. I removed the very bright initial pulse and focused on the emission from ≈ 50 s to 175 s (see Fig. 3.6). I unambiguously recover the main pulsation period ($P \approx 7.56$ s) together with the first, second, third, and fifth harmonic.

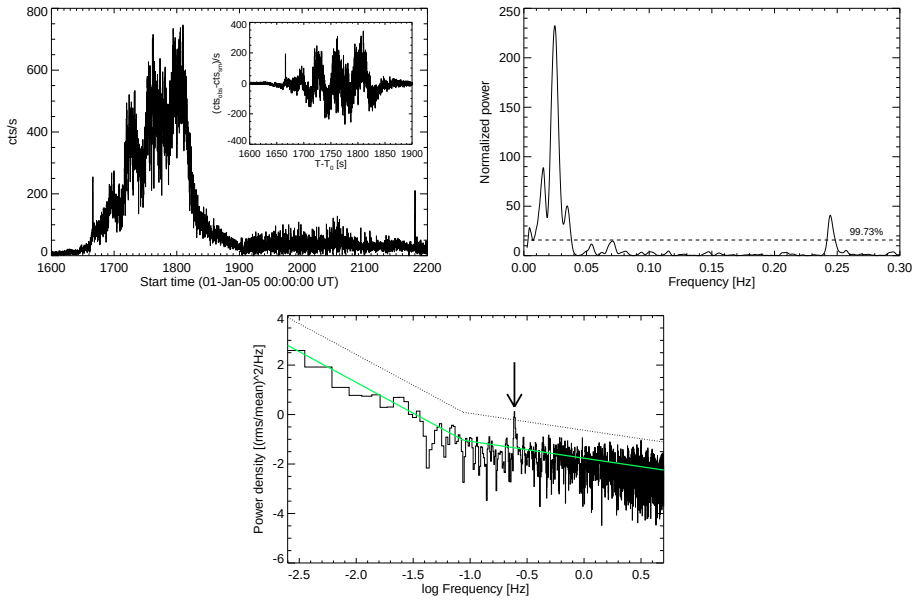

Figure 3.5 *Upper panel:* Summed and background subtracted light curve of the solar flare observed by RHESSI on 2005 January. The inset shows the residual emission after subtracting a simple (boxcar) moving average. *Middle panel:* Periodogram analysis performed on the residual emission. *Lower panel:* PSD with best fit broken power-law (solid green line) and the 3σ significance level (dotted line) indicated. The arrow points to the significant frequency at $f \approx 0.244$ Hz.

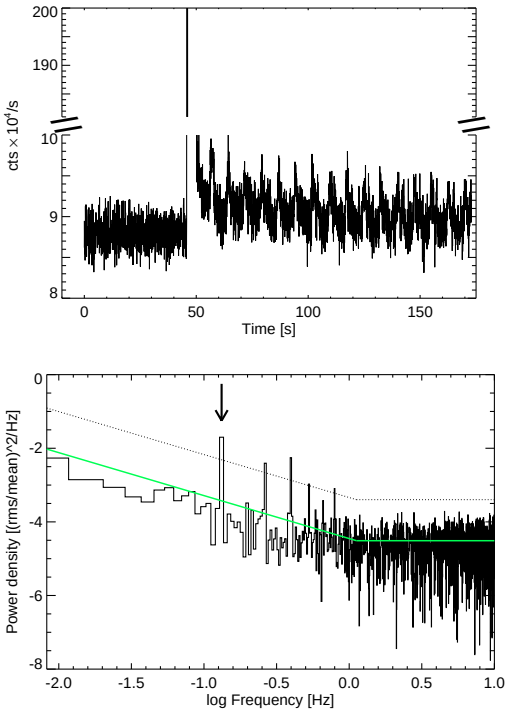

Figure 3.6 *Upper panel:* Light curve of the giant flare of SGR 1806-20 observed by SPI-ACS. *Lower panel:* PSD of the SGR 1806-20 light curve. Best fit broken power-law to the PSD continuum (solid green line) and the 3σ significance level (dotted line) are indicated. The arrow indicates the recovered rotation period of $P \approx 7.56$ s. Other peaks above the 3σ levels are harmonics.

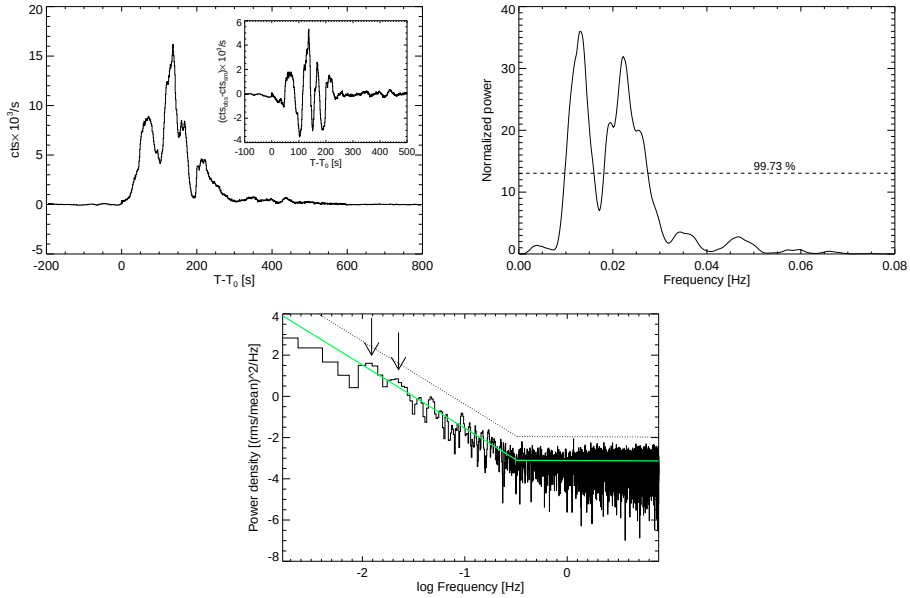

Figure 3.7 *Upper left panel*: Summed and background subtracted light curve of the solar flare observed by GBM on 2011 February 24. The inset shows the residual emission after subtracting a simple (boxcar) moving average. *Upper right panel:* Periodogram analysis performed on the residual emission. Two peaks are above the 3σ confidence limit (dashed line). *Lower panel:* PSD of the same solar flare. Best fit broken power-law to the PSD continuum (solid green line) and the 3σ significance level (dotted line) are indicated. The arrow denotes the wrongly identified frequencies of the PSD applied on the residual emission.

I conclude that the methodology applied here is appropriate and reliable for the following analysis.

3.2.3 Solar flares observed by GBM

Solar flare on February 24, 2011 at 07:29:20.71 UT

For the analysis, I used CSPEC and CTIME data of detectors NaI 3, NaI 4, and NaI 5 with a time resolution of 1.024 s (4.096 s pre-trigger) and 0.064 s (0.256 s pre-trigger), respectively. In the energy range from 50 keV to 1 MeV, this solar flare lasted for about 500 s. The light curve (Fig. 3.7) consists of several peaks and a compellingly looking quasi-periodic behavior lasting until $\approx$ 500 s. After de-trending the raw light curve with a simple moving average (50 s), the QPP pattern becomes more visible (see inset of Fig. 3.7). Applying a standard periodogram analysis (Lomb, 1976; Scargle, 1982) to the *detrended* light curve, several peaks are above the 3σ confidence limit as can be seen in the middle panel of Fig. 3.7.

However, applying the previously introduced method (Vaughan, 2005) to the original light curve, thus taking into account the red-noise properties of the source, I did not find any significant QPP during the solar flare life-time, as pointed out in the lower panel of Fig. 3.7. I performed this analysis making use of the CTIME data with a time resolution of 64 ms. The PSD was calculated for the signal spanning from $(T_0 - 10)$ s to $(T_0 + 600$ s), where T_0 denotes the time of trigger.

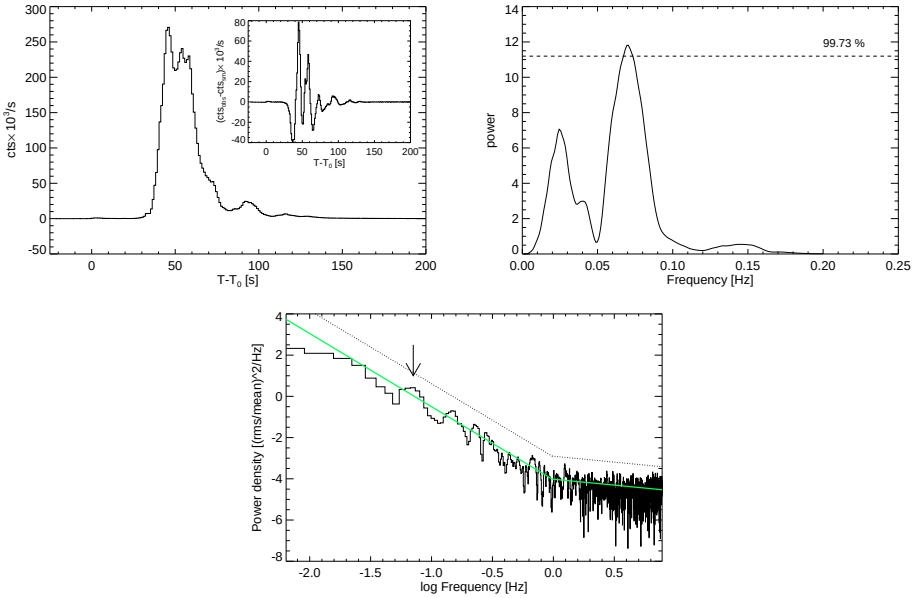

Figure 3.8 *Upper left panel:* Same as Fig. 3.7 for the solar flare observed on 2010 June 12. *Upper right panel:* Same as Fig. 3.7. *Lower panel:* Same as Fig. 3.7.

Solar flare on June 12, 2010 at 00:55:05 UT

For the analysis, I again used CSPEC and CTIME data of detectors NaI 0 through NaI 5. The count rate did not increase significantly during the first 30 s in the 50 keV to 1 MeV energy range. After this time, there is a sharp increase in the flare brightness, which then decays again very rapidly after 60 s. The whole duration of the solar flare in this energy range is approximately 120 s. Overlaid on top of the observed light curve, one can again clearly identify a QPP behavior with a period of ~ 15 s (see upper panel of Fig. 3.8). This periodicity appears to be quite significant when applying a standard Lomb-Scargle periodogram (see middle panel of Fig. 3.8) to the detrended light curve. The smoothing length was 15 s.

However, the PSD, which I computed using CTIME data with a time resolution of 64 ms in the interval from$(T_0 - 25)$ s to $(T_0 + 150)$ s and applying the method of to Vaughan (2005), does not display any significant periodicity.

Solar flare on March 14, 2011 at 19:50:17.3 UT

For the analysis, I used the same data type, energy range, and time resolution as for the previous solar flare. The total duration of the solar flare is approximately 150 s (see Fig. 3.9). In contrast to the Lomb-Scargle periodogram, which identifies a significant periodicity in the detrended light curve (smoothing length of 10 s), the PSD, determined for the time interval between $(T_0 - 25)$ s and $(T_0 + 150)$ s using the method of Vaughan (2005), did not identify any significant QPP.

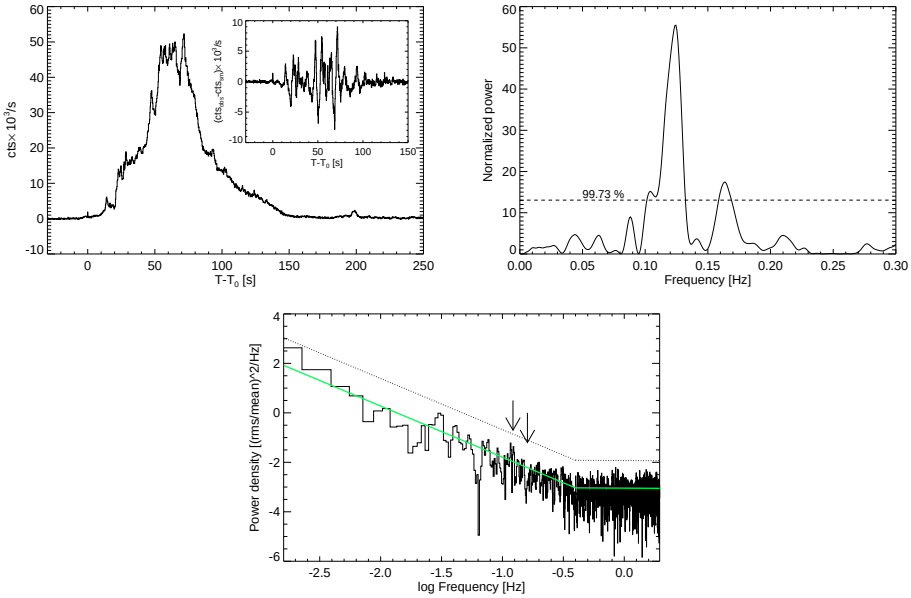

Figure 3.9 *Upper left panel:* Same as Fig. 3.7 for the solar flare observed on 2011 March 14. *Upper right panel:* Same as Fig. 3.7. *Lower panel:* Same as Fig. 3.7.

Solar flare on March 15, 2011 at 00:21:15.69 UT

For this analysis, I adopted CTIME data of detectors NaI 0 through NaI 5 in an energy range covering 50 keV to 1 MeV with a time resolution of 0.256 s. The total duration of the solar flare in this energy range is approximately 50 s (see Fig. 3.10). For the Lomb-Scargle periodogram analysis (see middle panel of Fig. 3.10), the light curve was detrended with a simple moving average of 5 s. After repeating the PSD analysis of the original data set between $(T_0 - 30)$ s and $(T_0 + 100)$ s using the method of Vaughan (2005), I did not find any significant QPP.

3.2.4 Conclusions

I tested the data of five solar flares for the presence and significance of QPPs applying the method introduced by Vaughan (2005). First of all, this technique was validated and tested by applying it to raw data of the RHESSI satellite. Any RHESSI light curve has an inherent period caused by the rotation of the spacecraft about its axis. With the method adopted here, I successfully retrieved this well-known 4 s period. However, I was I unable to confirm the previously reported QPP of 40 s in the very same solar flare (Nakariakov et al., 2010a). An additional check was performed by applying the method to SPI-ACS data of the giant flare of the well-known SGR 1806-20. This magnetar has a rotation period of 7.56 s, which, together with several harmonics, could be recovered unambiguously with the procedure presented here. These two tests gave me confidence that the method is appropriate to test the significance of QPPs in red-noise-dominated solar-flare time series.

The routine was then applied to four solar flares observed by GBM. Although all of these solar flares displayed apparently clear quasi-periodic features in their detrended light curves, none of these were significant ($> 3\sigma$). Previous authors (e.g. Inglis et al., 2008; Inglis and Nakariakov, 2009; Zimovets and Struminsky, 2010; Nakariakov et al., 2010a) who claimed a

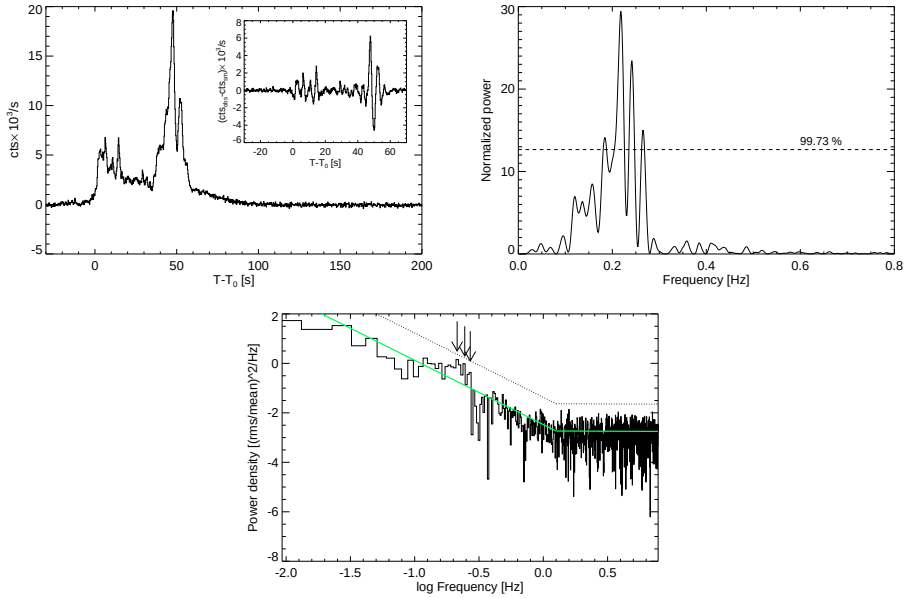

Figure 3.10 *Upper panel:* Same as Fig. 3.7 for the solar flare observed on 2011 March 15. *Middle panel:* Same as Fig. 3.7. *Lower panel:* Same as Fig. 3.7.

significant QPP detection, applied a standard Lomb-Scargle analysis to detrended solar-flare light curves. My investigation of this method suggests that the power in the low frequency range is being artificially suppressed, which can lead to misleading values of the significances of features in the PSD. A periodogram analysis should always be performed on the raw and undetrended light curve as done here.

I emphasize once again that not only solar flares but many astrophysical sources (X-ray binaries, Seyfert galaxies, GRBs) have steep power spectra in the low-frequency range. These power spectra ensure that a periodogram analysis is not trivial, the interpretation of a peak in a PSD is more complex than usual, and that the estimate of the peak's significance is important. Again I emphasize that red-noise is an intrinsic source property. In other words, having shown that the variations in the corresponding solar flares are not quasi-periodic at the 3σ level does not mean that these variations are not real. The corresponding flux changes are sometimes dramatic, reaching a factor of a few within a few tens of seconds. In addition, these variations occur in phase at different X-ray to γ-ray energies, and other flares have been observed to also occur in phase with microwave radio emission (e.g. Nakariakov et al., 2010a; Foullon et al., 2010).

While I consider it unnecessary to invoke oscillatory regimes of plasma instabilities (Nakariakov et al., 2010b; Reznikova and Shibasaki, 2011), I note that the physics of these variations is certainly interesting and worth further study.

3.3 The "Solar Background Employing Relative Rates" (SOBER^2) method

3.3.1 Introduction

In this section, I am going to present a new method to determine the BGO background count rate for solar flare observations. In order to show its advantages compared to the standard background subtraction routine, it is applied to real life observations of a solar flare. This section is organized as follows. In §3.3.2 I am going to present the GBM data of a very energetic X1.4 solar flare observed on 2012 March 7, in §3.3.3 I will highlight the issues with the default GBM background subtraction, in §3.3.4 I will present the new SOBER^2 method including the so obtained spectral results of the solar flare and finally, in §3.3.5 I am concluding this section.

3.3.2 Observations

GBM triggered and located a very bright and energetic X5.4 class solar flare on 2012 March 7th, at 00:30:32.13 (t_0) and triggered another 3 times on a subsequent X1 class solar flare at 01:00:57.53 UT, 01:10:58.20 UT and 02:06:09.93 UT. Most of the first solar flare was occulted by Earth so that only the last part of the prompt emission epoch is visible in GBM. The second solar flare, which followed only 30 min later, was visible until GBM entered the SAA during which the detectors were turned off. After exiting the SAA the solar flare was occulted by the Earth and only when it reappeared 1 h after the second trigger, GBM was able to observe the last minutes of this solar event. Fortunately, the Anti-Coincidence Shield (ACS) of the SPI instrument on board the INTEGRAL[b] satellite does not suffer from Earth occultation effects for this flare and therefore could observe both events without interruption.

3.3.3 Problems with the default GBM background estimation

Using the default GBM analysis (see § 1.2.1), the background fit and source selection is shown in Fig. 3.12 for the solar flare observed on 2012 March 7th. As is evident from this Figure, the background estimation works reasonably well for lower energy channels but breaks down at higher energy channels, i.e. the background model (i) does not follow the general background variation pattern of the data and, consequently, is (ii) consistently underestimating the observed background model rate in the region of interest (see Fig. 3.12). This leads to an over estimation of source rates at these high energies.

After (wrongly) fitting the background, the spectrum is then fitted using the sum of a simple power-law (PL), a power-law with exponential cutoff (COMP), a nuclear line template, 2 Gaussian functions (for the positron annihilation line at 511 keV and the neutron capture line at 2223 keV) and a pion decay template. For more details regarding these model terms, I refer to Ackermann et al. (2012). The resulting count and photon spectrum are shown in Fig. 3.13 and the fit results are shown in Table 3.2.

3.3.4 Working principle of SOBER^2

In sky-pointing mode one detector side, i.e. half of the detectors of GBM, are always pointed directly towards the Sun whereas the other half are shielded by the spacecraft. This specific detector configuration can be useful in determining the background rate of the sun-facing BGO 0

[b]For more information on INTEGRAL, SPI and SPI-ACS I refer to Winkler et al. (2003), Vedrenne et al. (2003) and Mereghetti et al. (2005)

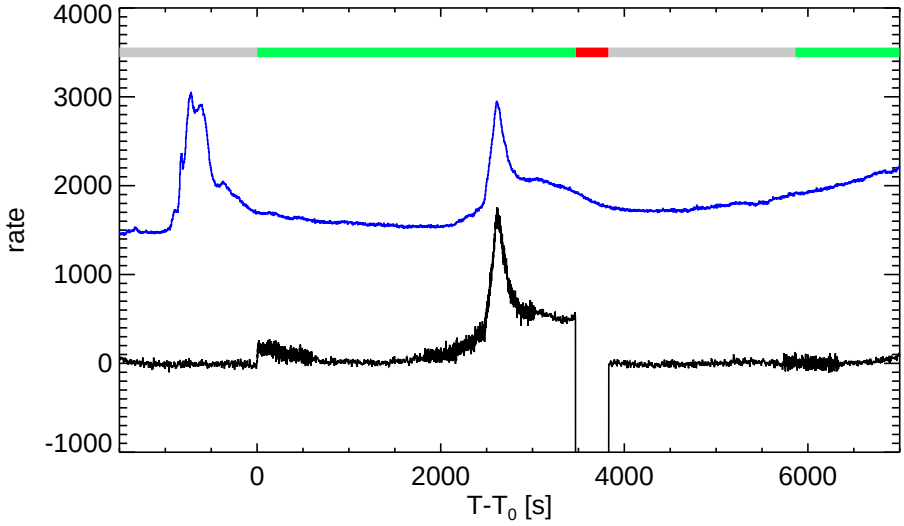

Figure 3.11 Light curve of the energetic X5.4 and X1.1 class solar flares observed by SPI-ACS (blue solid line) in the 80 keV < E < 10 MeV energy range and background subtracted GBM light curve (black solid line) in the 250 keV < E < 40 MeV energy range. The grey and green colored regions indicate when the Sun was occulted by the Earth and visible by GBM, respectively. The red region indicates the SAA transit of GBM.

detector using the observed count rate in BGO 1 as *a priori* information. In Fig. 3.14, I show the count rates of both BGO detectors in the energy range from 250 keV to 40 MeV. One can see that although the amplitude of the background variations can be quite different, the phase remains the same in both detectors. The peaks and valleys visible in the light curves are clearly due to the orbit of *Fermi* around the Earth. The goal now is to use the information of the Sun shaded detector BGO 1, to infer the background count rate in the Sun-facing BGO 0.

The idea of SOBER^2 is quite simple: The first step is to generate the relative count rates of the two detectors, i.e.

$$rr_i = \frac{R_{\mathrm{B0},\,i}}{R_{\mathrm{B1},\,i}}, \tag{3.1}$$

where rr are the relative rates and R the count rates of the two BGOs, for each and every energy channel, i, separately. As an example, such a relative rate light curve is shown in the upper panel of Fig. 3.15 (Please note that by way of exception and for illustrational purpose only, here I have used the *summed* count rates across all energy channels for a better signal-to-noise ratio). It is clearly evident that the relative rates have a periodical pattern. The next step is to again select *off* interval(s) (ideally before and after the *on* interval) which are then used to fit a simple sinusoid to the relative rates (or a more complex function e.g. to account for the long time trend in the data) which is then extrapolated across the *on* interval. By doing this, both the "relative rates" *model* (red solid line in Fig. 3.15) and the *observed* count rate of BGO 1, R_{B1}, are known and consequently, it is now straight forward to infer and estimate the background count rate for the *on* interval in BGO 0 (grey shaded region), i.e.

$$R_{bkg,\,\mathrm{B0},\,i} = rr_{on,\,i} \times R_{on,\,\mathrm{B1},\,i} \tag{3.2}$$

The major caveats of the SOBER^2 method are that

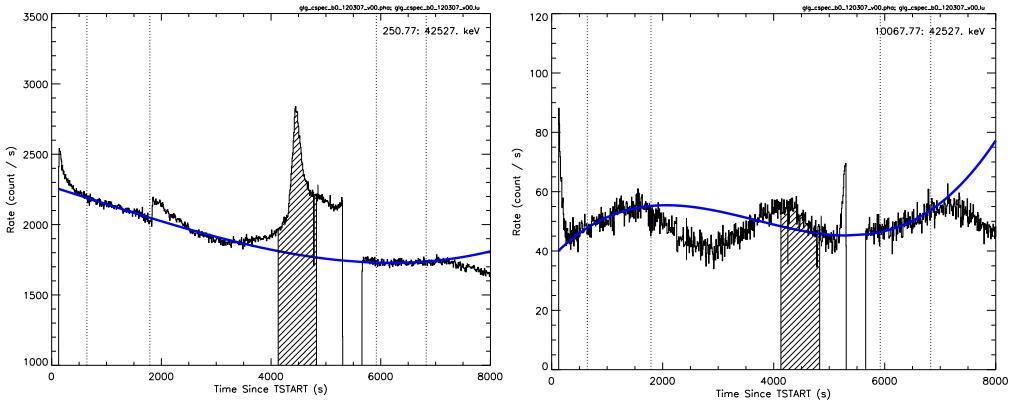

Figure 3.12 *Left panel:* Typical background fit in GBM CSPEC data showing the full energy range of the BGO (250 keV - 40 MeV). Two *off* intervals (denoted by the vertical dotted lines) are used to fit a polynomial of 4th order in all energy channels (blue solid line) across the *on* interval (filled, rectangular box from T0+$\sim$ 4000 s to T0+$\sim$ 5000 s). *Right panel:* Same as above, showing the CSPEC data only from 10 MeV to 40 MeV. While it works reasonably well at lower energies, it is evident that the *off* interval selection is not adequate to estimate the background at higher energies.

(i) it implicitly assumes that no signal from the source (the Sun in this specific case) is visible in the occulted BGO (BGO 1 in the case presented here). If there were indeed signal present in BGO 1, the inferred background count rate for BGO 0 will be larger than it is in reality. The future goals are to check this via simulations.

(ii) the variation of the relative rates is not a perfect sinusoid. Indeed, looking at the residuals in the lower panel of Fig. 3.15 it is quite obvious that there remain some additional fluctuations which are not properly accounted for by the simple sinusoid model. (However, please also note that this fluctuations are in the order of only $\sim$ 10% for the summed energy channels). Obviously, these fluctuations have been error propagated when calculating the background count rate for BGO 0.

The so obtained spectrum can be seen in Fig. 3.16. Although the general behavior at lower energies is similar to Fig. 3.13, the spectrum is significantly different at energies $>$ 10 MeV. Indeed, using the SOBER^2 method, it becomes obvious that the high-energy range of the BGO 0 is completely governed by upper limits. Contrary to what was observed using the polynomial background subtraction, the pion component is now completely unconstrained as there is no signal at $E > 10$ MeV (see Table 3.2).

3.3.5 Conclusions

In this section, I have presented a new method to estimate the background variations in the BGO detectors of the GBM instrument. The SOBER^2 method provides a more accurate way to account for the background in solar flares, especially if they are of long duration. It will provide better solar flare spectra in the future. Although I have shown some preliminary spectral fits , a more detailed analysis and interpretation of such spectra would go beyond the scope of this thesis and will be published in a future work. In conclusion, the SOBER^2 method is a viable solution for background estimation when a highly energetic astrophysical event illuminates one

Table 3.2 Best fitting spectral parameters for the three emission episodes in GRB 091024.

model		polynomial bkg	*rr* method
PL flux	[γ cm^{-2} s^{-1} keV^{-1}]	1.93 ± 0.11	1.17 ± 0.05
PL index		-4.62 ± 0.07	-4.22 ± 0.04
COMP flux	[γ cm^{-2} s^{-1} keV^{-1}]	$7.85 \pm 1.9 \times 10^{-3}$	$0.37 \pm 0.11 \times 10^{-3}$
COMP index		-1.35 ± 0.11	0.11 ± 0.14
COMP E_{peak}	[MeV]	3.71 ± 0.27 MeV	3.17 ± 0.09 MeV
Nuclear line flux	[γ cm^{-2} s^{-1} keV^{-1}]	0.41 ± 0.02	0.26 ± 0.02
Pion-decay flux	[γ cm^{-2} s^{-1} keV^{-1}]	0.11 ± 0.01	n.a
511 keV line flux	[γ cm^{-2} s^{-1}]	0.06 ± 0.06	0.05 ± 0.05
2223 keV line flux	[γ cm^{-2} s^{-1}]	0.132 ± 0.004	0.095 ± 0.004

BGO detector while the other is shielded from the spacecraft.

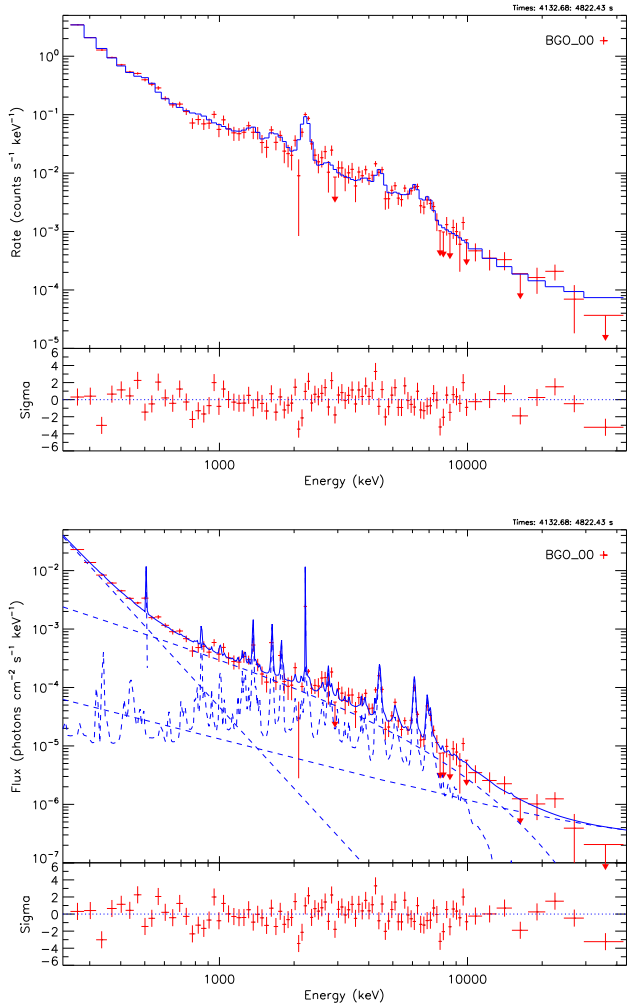

Figure 3.13 *Upper panel:* Count spectrum of the solar flare shown in Fig. 3.12 using the polynomial background subtraction. *Lower panel:* Photon spectrum of the solar flare, showing the individual model terms (dashed lines).

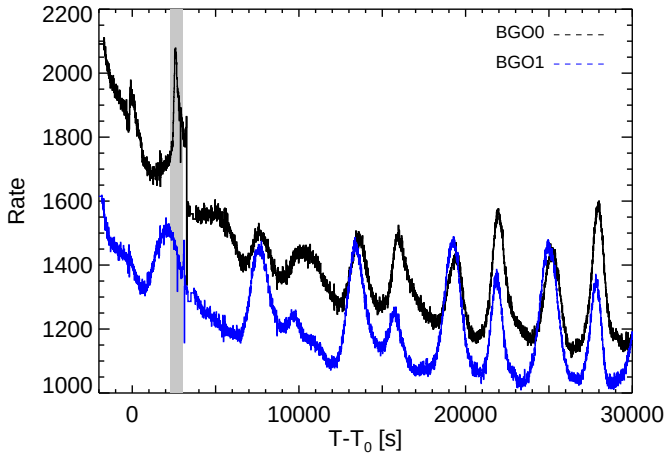

Figure 3.14 Count rates of detectors BGO 0 and BGO 1 integrated over the energy range from 250 keV to 40 MeV, together with the *on* interval (grey shaded region).

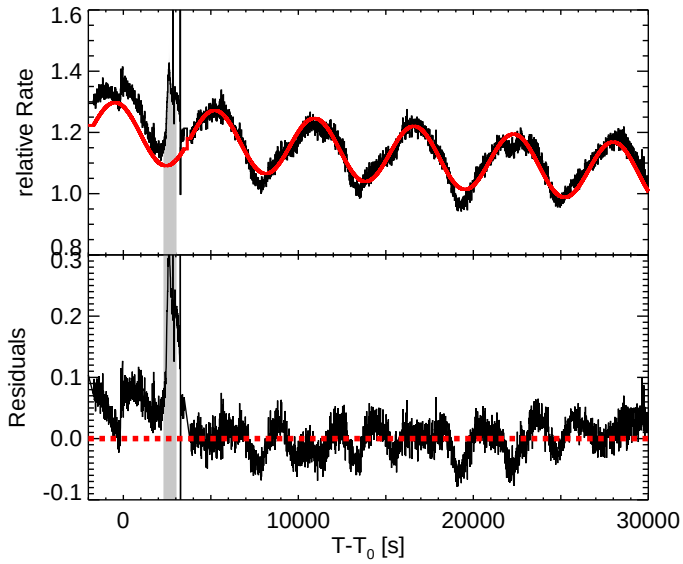

Figure 3.15 *Upper panel:* Relative count rates *rr* of the 2 BGO detectors using the full energy range from 250 keV to 40 MeV (black solid line) together with a simple model (superposition of a sinusoid and a linear function, red solid line). *Lower panel:* Residual rates after model subtraction. The grey-shaded region denotes the *on* interval.

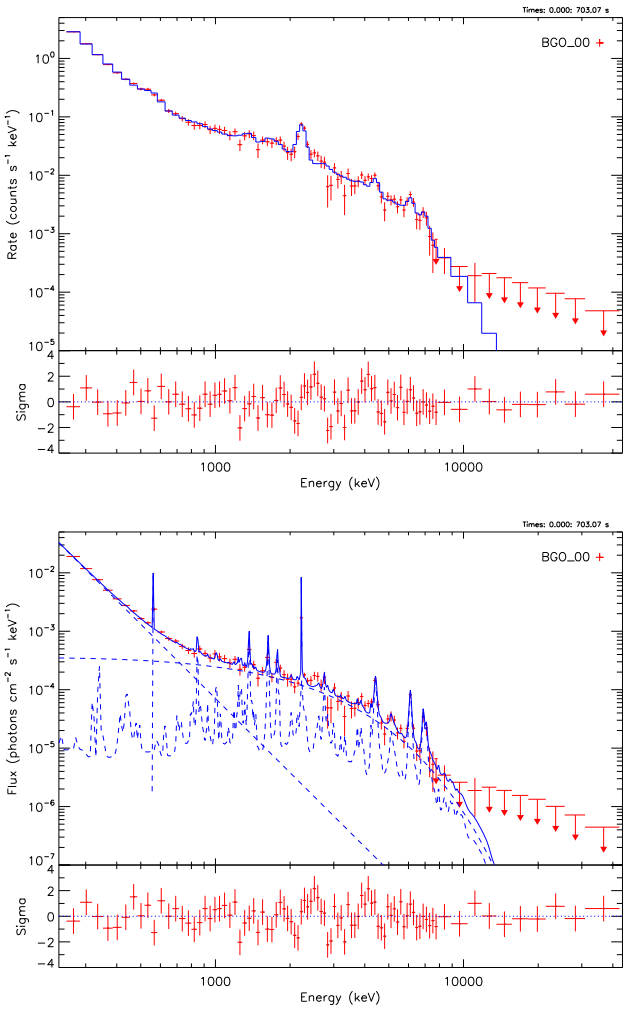

Figure 3.16 Same as in Fig. 3.13 for the SOBER^2 method. For details see the main body of this section.

Chapter 4

Soft Gamma Repeaters

4.1 Introduction

Soft Gamma Repeaters (SGRs) are a small, distinct group of isolated neutron stars characterized by peculiar observational features such as large X-ray luminosities and repeated bursts of soft γ-rays. They were discovered through the detection of short bursts in the hard X- and soft γ-ray range (Mazets et al., 1979). In fact, due to their nature it was initially believed that they form a subclass of GRBs (Laros et al., 1986; Atteia et al., 1987), strangely recurring from the same sky direction. Thus, they were labeled "Repeaters". Thanks to deep optical/IR/radio counterpart searches, it was discovered that these sources are rotating, having a narrow period distribution, long-term spin-down rate and a soft spectrum in their persistent emission (Mereghetti and Stella, 1995). SGRs undergo active bursting episodes, emitting many bursts over a timescale of hours to days with typical SGR bursts lasting ~ 0.1 s with peak luminosities of $L_p \leq 10^{41}$ erg/s. It was found that the X-ray luminosity of these astrophysical objects, contrary to other known pulsars, was larger than their spin-down power could provide. The most successful model in explaining the emission from SGRs is the magnetar model which requires immense magnetic fields in the magnetosphere that powers the emission of SGRs (Thompson and Duncan, 1995, 1996). Magnetars have periods (P) ranging between 2 s and 12 s and period derivatives ($\dot{P}$) between 10^{-13} ss^{-1} and 10^{-10} ss^{-1}. Using the magnetic spin down formula one can infer the magnetic field strength of these objects to be of the order of 10^{14} to 10^{15} G, orders of magnitude higher compared to the 10^{12} G of a canonical neutron star.

Spectral energy distribution

The observed spectral energy distribution (SED) of SGR bursts is curved and broadly peaked, and extends from the hard X-rays to the soft γ-ray band. In recent years, several physical models have been adopted to describe their spectral shape. Thus, the SGR radiation can be interpreted in terms of either an optically thin gas, emitting via thermal bremsstrahlung (OTTB) with temperatures in the range $kT \sim 30 - 40$ keV, a thermal Comptonization model (COMP), generally described as a power-law with an exponential cutoff, or alternatively as a combination of single (BB) or double blackbody (2BB) models, where the hot component is attributed to a hot spot at the footprint of a magnetic loop and the cool component to deep crustal heating (Mereghetti, 2008). In particular, the superposition of two blackbody components with temperatures $kT_1 \sim 2 - 4$ keV and $kT_2 \sim 8 - 12$ keV provides an accurate description of the SGR burst radiation, thus making it the most adopted model (Feroci et al.,

2004; Olive et al., 2004; Nakagawa et al., 2007; Esposito et al., 2007; van der Horst et al., 2012; Lin et al., 2012).

In this chapter, I present an alternative physical model to describe the SGR burst emission: the log-parabolic function (LP) i.e. a curved, parabolic shape in a log-log space. Adopting the LP model, the SGR SEDs are described in terms of 3 parameters: (1) the peak energy, $E_{\rm peak}$ (in νF_ν space), (2) the maximum height of the SED, $S_{\rm peak}$, evaluated at $E_{\rm peak}$, (proportional to the flux at $E_{\rm peak}$), and (3) the spectral curvature, b, around $E_{\rm peak}$ (Massaro et al., 2006; Tramacere et al., 2007; Massaro et al., 2008). Moreover, the LP model has also a strong physical background because log-parabolic particle energy distributions (PEDs) are obtained as solutions of the Fokker-Planck equation from a mono-energetic electron injection when both systematic and stochastic acceleration terms are considered (Kardashev, 1962; Massaro et al., 2006; Stawarz and Petrosian, 2008; Paggi et al., 2009). In particular, the origin of the spectral curvature is directly related to the presence of the stochastic acceleration term (Tramacere et al., 2007, 2009, 2011; Massaro et al., 2011). Including radiative losses as well as the "disappearance" of fast particles escaping from the acceleration region, the numerical solution for the kinetic equation yields a spectral shape well described by an LP function (Tramacere et al., 2009; Paggi et al., 2009).

The LP model has also been recently used to describe the SEDs of different classes of both Galactic and extragalactic sources, such as plerions (Campana et al., 2009), high frequency peaked (HFPs) radio sources (Maselli and Massaro, 2009), solar flares (Grigis and Benz, 2008) and GRBs (Massaro et al., 2010; Massaro and Grindlay, 2011).

Here, I apply the LP model to describe the SED of SGR J1550-5418 (see Kaneko et al., 2010; van der Horst et al., 2012, and references therein). I aim at describing the spectral properties of SGR J1550-5418 during three emission episodes of γ-ray activity occurred in

I 2008 October 3 by emitting 22 SGR bursts within 7 days (von Kienlin et al., 2012)

II 2009 January 22, in which SGR J1550-5418 showed a second period of extremely high bursting activity which lasted for another 7 days (see Mereghetti et al., 2009; Kaneko et al., 2010; van der Horst et al., 2012)

III 2009 March 22, which is the tail end of the major source outburst during 2009 January (see II), with another 15 bursting events that lasted until 2009 April 17 (von Kienlin et al., 2012).

The chapter is organized as follows: in §4.2.1, I present my observations and data reduction procedures and in §4.2.2, I briefly review the main properties of the LP function, also showing the results of the spectral analysis for several bursts of SGR J1550-5418 and illustrating the statistical analysis performed on the spectral parameters.

4.2 Stochastic particle acceleration within SGR bursts: A case study with SGR J1550-5418 using *Fermi*/GBM data:[a]

4.2.1 Observations and data reduction procedures

I used time-tagged event (TTE) data with a fine time resolution of 32 ms. Since the SGR bursts emit in the soft γ-ray regime, only NaI data in the energy range from 8 keV to 200 keV were used for the spectral analysis. An additional requirement is the use of detectors which had source angles $\leq 60^{\circ}$ and were not occulted by the spacecraft and the LAT at any time.

My sample includes 17 and 14 bursts from the 2008 October (hereafter referred to as emission episode I) and 2009 March/April period (hereafter, emission episode III), respectively. Because GBM observed more than 500 burst events during the 2009 January emission epoch (hereafter, emission episode II), a randomly selected subsample of 55 bursts was analyzed excluding those that have saturated the High Speed Science Data Bus of GBM. This effect occurs when the total TTE count rate of all detectors exceeds a limit of 375,000 counts/s. To ensure that none of the bursts in my sample is affected by saturation and/or pile-up effects, I made sure that no SGR bursts with count rates $> 1.5 \times 10^5$ cts/s were included in my sample. The final sample consists of 86 burst spectra of SGR J1550-5418,

4.2.2 Methods & Results

The log-parabolic spectral shape

I adopted the LP spectral shape (Massaro et al., 2008) to describe the broad band SED of the SGR burst emission for the following spectral analysis. I used the following representation of the LP model

$$F(E) = S_{\rm p}\, E^{-2}\, 10^{-b \log^2(E/E_{\rm p})}. \tag{4.1}$$

expressed in terms of the spectral curvature (b) the peak energy ($E_{\rm peak}$) and the maximum flux of the SED ($S_{\rm peak}$).

With eq. 4.1, the three parameters: $E_{\rm peak}$, $S_{\rm peak}$ and b, can be evaluated independently in the fitting procedure, thus allowing to investigate the presence of possible correlations among them without introducing any functional biases (Tramacere et al., 2007).

The results of the LP fits are reported in the following subsection. All the statistical uncertainties quoted in this paper refer to the 68% confidence level (one Gaussian standard deviation).

Spectral analysis

I used the RMFIT[b] software package (version 4.0rc1). The Castor C-Statistic has been adopted in the fitting procedure as a figure of merit to be minimized (C-Stat; Ackermann et al., 2011). Unfortunately, this method does not provide an estimate of the goodness-of-fit. Therefore, I also adopted the χ^2 statistic to compare how different models describe the SGR spectral shape. Following Goldstein et al. (2012), I calculated χ^2 by fixing the spectral parameters obtained through C-Stat minimization to assess the goodness-of-fit, even though χ^2 itself was not minimized.

[a] The work presented here has been submitted to *Astronomy & Astrophysics*

[b] RMFIT for GBM and LAT analysis was developed by the GBM Team and is publicly available at `fermi.gsfc.nasa.gov/ssc/data/analysis/`.

All 86 SGR bursts have been fitted separately with all the current SGR models BB, 2BB, OTTB, COMP and the LP one, respectively.

I show an example of the goodness of the fitting procedure for the spectrum of an example SGR J1550-5418 burst which was observed on 2009 January 22, fitted with the 2BB and the LP, respectively in Fig. 4.1. The former yields a C-STAT= 352 (χ^2 = 310) for 199 DOF and the latter a C-STAT= 308 (χ^2 = 261) for 200 DOF. It is evident that the residuals of the LP are at least consistent with if not better than the residuals of the 2BB.

The results of the spectral fits to my sample, such as the distributions of b and $E_{\rm peak}$ subdivided for the three respective emission episodes are presented in Fig. 4.2. The bursts from emission episode I are, in general, very weak with a low signal-to-noise ratio. As discussed in von Kienlin et al. (2012) the first emission epoch is best fit by a single BB function. Indeed, the LP fits to the October events give reduced χ^2 values which are very similar to the single BB fits (see also Fig. 4.3). Additionally, the curvature, b, of the LP has very large values, compared to the other emission epochs (see Fig. 4.2). The conclusion therefore is that the LP simply mimics the behavior of a single BB over the energy range that is probed by the data. Since the LP is the more complex model in terms of free fitting parameters, the single BB is the favored model for emission episode I.

The spectral analysis of episode II is discussed in great detail in van der Horst et al. (2012). Here, I am going to expand on their results by adding the LP to the selection of the spectral models for 55 bursts. The spectral analysis of emission episode III on the other hand, is again presented in von Kienlin et al. (2012). The mean $E_{\rm peak}$ value of the January and March/April episodes is 38 keV which is consistent with the $E_{\rm peak}$ values obtained via the OTTB and COMP model fits found by van der Horst et al. (2012) which cluster around $\sim$ 40 keV.

Looking at Fig. 4.3, I want to emphasize the following aspects:

(i) the 2BB and the LP give similar good fits in terms of the differences in C-STAT (ΔC-STAT), clustering normally around $\mu \approx 2.5$ with a standard deviation of $\sigma \approx 12$. Considering that the 2BB uses one model parameter more with respect to the LP model, the LP model generally seems to be a statistically better description of the SGR burst spectra than the 2BB function.

(ii) The ΔC-STAT is not a function of burst luminosity, as there is no evident correlation with the energy flux (obtained in the energy range from 8 keV to 200 keV). In other words, the burst intensity does not influence the selection of the best fit model.

(iii) The goodness-of-fit (expressed in terms of reduced χ^2) is roughly the same for the LP and 2BB model, as the two distributions of red. χ^2 are consistent within all emission episodes.

Swift/XRT and GBM joint fits

Following Lin et al. (2012), I performed a spectral analysis of 19 SGR bursts which were observed simultaneously by both GBM and the *Swift*/XRT telescope (Burrows et al., 2005). The XRT is an X-ray imaging spectrometer sensitive to photons in the 0.3-10 keV energy range and it is operated either in Photon Counting (PC) mode or in Windowed Timing (WT) mode. Due to the too coarse temporal resolution for SGRs of the PC mode only observations performed in WT mode were used for the subsequent analyses. For more details on the data reduction and analysis procedures, I refer to Lin et al. (2012). For my spectral analyses a constant factor was multiplied to the normalization of the model to take into account the calibration uncertainty among the two different instruments.

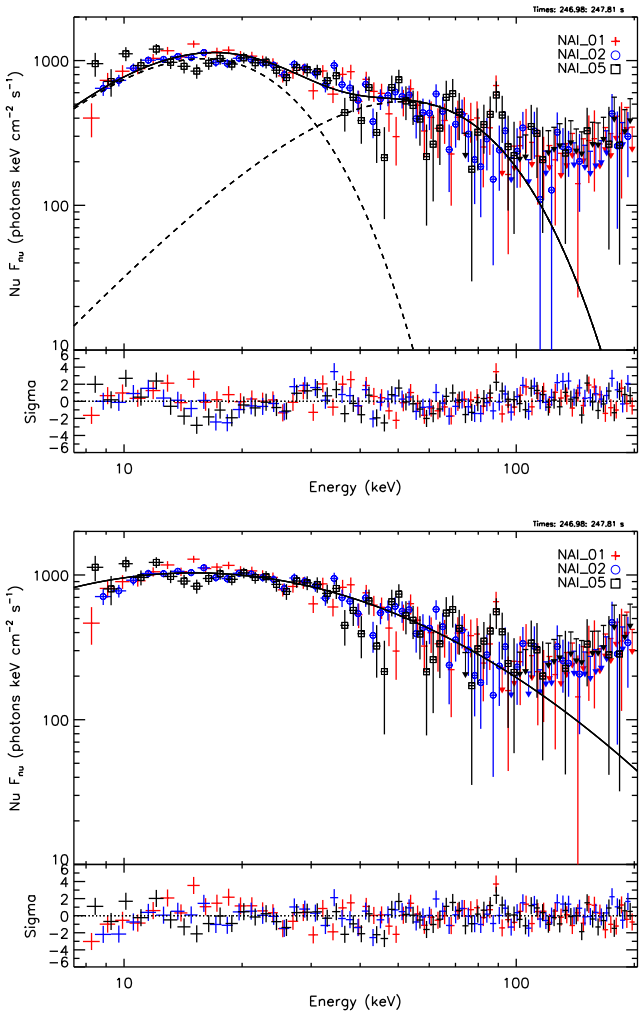

Figure 4.1 *Upper panel:* νF_ν plot showing the double blackbody fit to an SGR burst of the January 2009 emission epoch. *Lower panel:* The same as above showing the LP fit to the data.

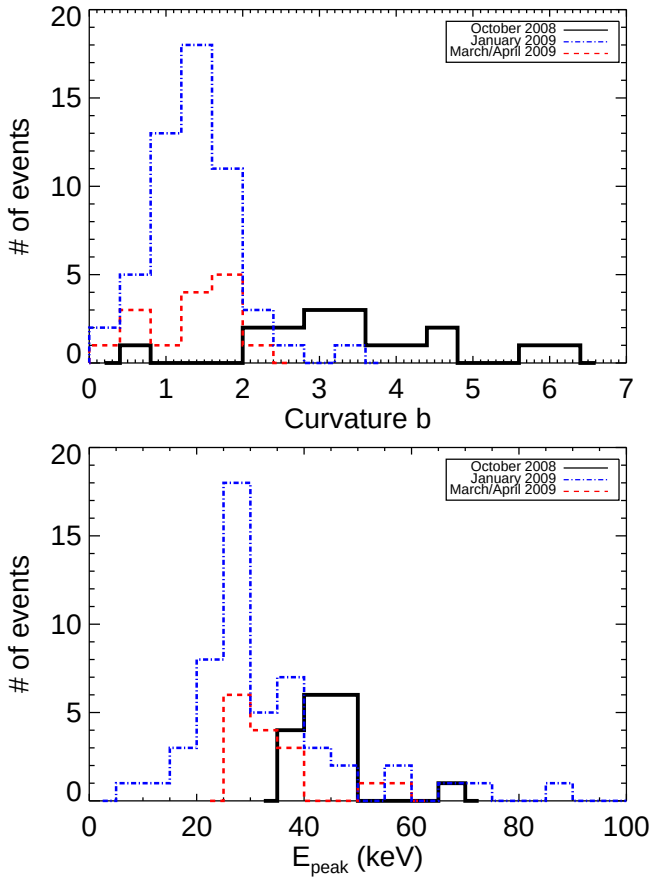

Figure 4.2 Results of LP fits. *Upper panel:* Distribution of the curvature. *Lower panel:* Distribution of $E_{\rm peak}$

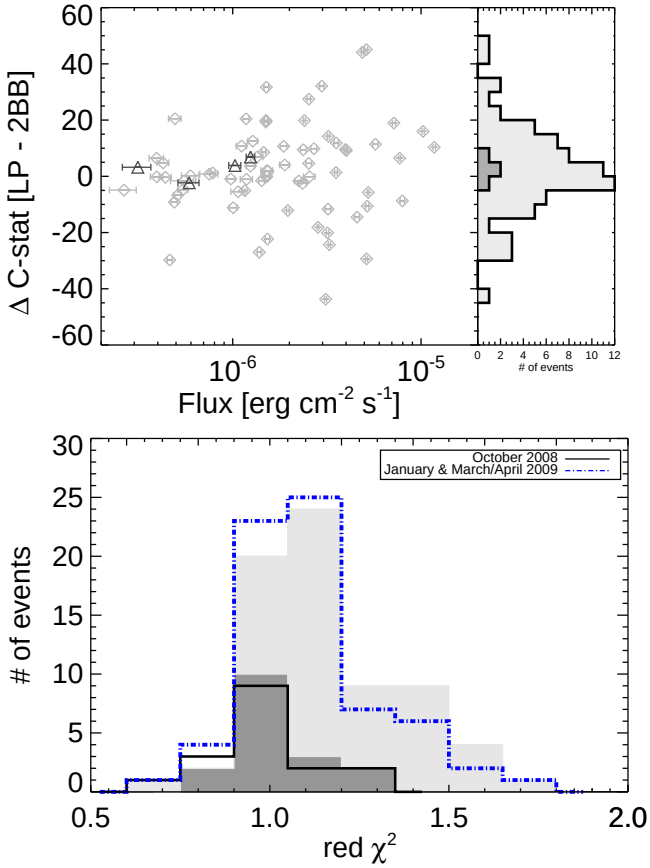

Figure 4.3 *Upper panel:* Difference in C-STAT between the LP and 2BB as a function of the energy flux (8 keV - 200 keV) for episode I (dark-grey triangles and histogram) and episodes II and III (light-grey diamonds and histogram). *Lower panel:* Reduced χ^2 of the LP (solid black, dot-dashed blue histogram) compared to the reduced χ^2 of a single blackbody obtained for episode I (filled dark grey histogram) and a double-blackbody for emission episodes II and III (light grey histogram).

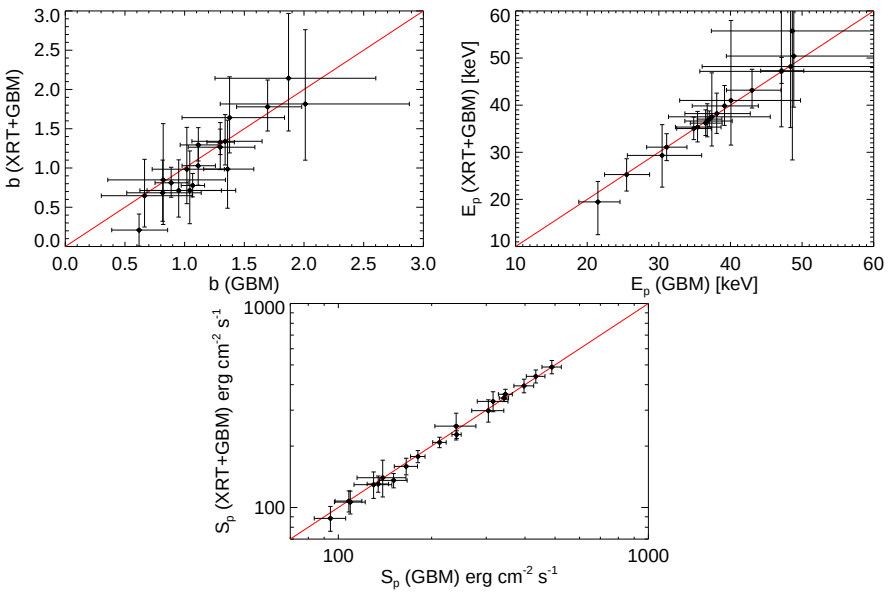

Figure 4.4 Comparison between GBM-only and GBM+XRT joint fits for the curvature b (upper panel), the peak energy $E_{\rm peak}$ (middle panel) and the maximum flux of the SED $S_{\rm peak}$ (lower panel).

First, I checked whether the inclusion of the XRT for the spectral fits would fundamentally change the spectral parameters of the LP obtained from GBM-only fits. To this end, I performed both GBM-only and GBM+XRT joint fits with XSPEC v12.7.0 (Arnaud et al., 2011) and compared the spectral parameters of the LP to one another. As can be seen in Fig. 4.4, the parameters agree very well within their respective 1σ error bars. I conclude that the LP also works very well in the softer energy range of the XRT (see also §4.2.2).

Similarly to what has been shown in Fig. 4.3, the reduced χ^2 for the LP and 2BB model are shown in Fig. 4.5 for the joint XRT and GBM spectral fits. It can be seen that the distributions are indeed quite similar (KS significance level of 0.2% that the distributions are statistically different to one another), concluding that both the 2BB and LP fit the data equally well.

Comparison to previous results

The 2BB function was originally introduced by Feroci et al. (2004) who applied it to 10 bursts which were observed by BeppoSAX. (For more information on SGR 1900+14, I refer to Feroci et al., 2004; Göğüş et al., 2011, and references therein.) I adopted the same spectral analysis described in Feroci et al. to compare the LP model with the 2BB scenario. Using XSPEC, I applied the 2BB and the LP to the summed spectra of 9 bursts observed by the MECS and PDS instruments onboard BeppoSAX, binning the data such as to have at least 20 counts per energy bin. Similar to XRT, the advantage of the latter instruments compared to GBM is the extension to energies down to 2 keV. Thus, similar to XRT, they provide a good way to test the behavior of the LP on even at lower γ-ray energies. Even though only nine out of the ten bursts of Feroci et al. (2004) were analyzed, the results of the 2BB fit are in good agreement and consistent with Feroci et al. except for the reduced χ^2 which is quite a bit larger in my case ($\chi^2_r = 1.26$). Thereafter, the LP was used to fit the data. I found that the reduced χ^2 ($\chi^2_r = 1.12$) is smaller

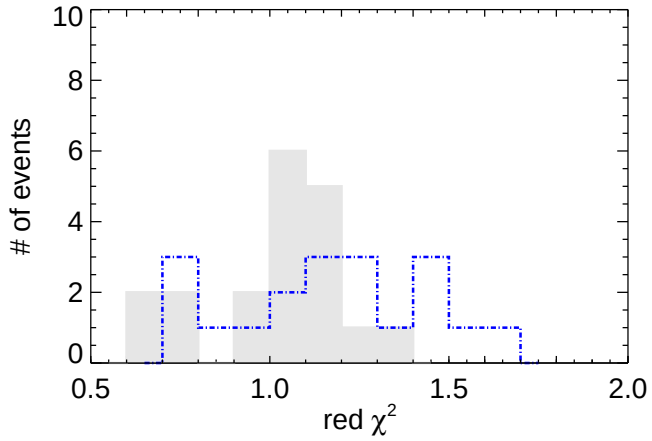

Figure 4.5 Reduced χ^2 of the LP (dot-dashed blue histogram) compared to the reduced χ^2 of the 2BB (light grey histogram) obtained from the joint XRT and GBM spectral fits.

compared to the 2BB function. In addition, I found a reasonable value for the equivalent neutral hydrogen absorption column, N_H, perfectly consistent with the one obtained from the 2BB fit and the value reported in Mereghetti et al. (2006). The fit parameters b and $E_{\rm peak}$ are consistent with the spectral parameters obtained for SGR J1550-5418. The detailed results are reported in Table 1.

Table 4.1 Best-fit parameters of SGR 1900+14 applying a 2BB and LP.

#	$N_{\rm H}$ ($10^{22}{\rm cm}^{-2}$)	kT_1 (keV)	kT_2 (keV)	b –	$E_{\rm peak}$ (keV)	χ^2/dof –
Feroci et al. 2004	2.0	$3.34^{+0.13}_{-0.14}$	$9.47^{+0.38}_{-0.39}$	–	–	1.02/255
this work	$2.17^{+0.39}_{-0.36}$	$3.23^{+0.08}_{-0.08}$	$9.33^{+0.23}_{-0.22}$	–	–	1.24/135
LP fit varying $N_{\rm H}$	$2.51^{+0.54}_{-0.50}$	–	–	$1.53^{+0.05}_{-0.05}$	$20.1^{+0.30}_{-0.30}$	1.11/136
LP fit fixed $N_{\rm H}$	2.0	–	–	$1.56^{+0.06}_{-0.06}$	$20.2^{+0.49}_{-0.47}$	1.11/137
LP fit w/o $N_{\rm H}$	–	–	–	$1.75^{+0.04}_{-0.04}$	$20.4^{+0.29}_{-0.28}$	1.33/137

Statistical analysis

I investigated possible correlations between the spectral parameters. For the emission episodes II and III, I find a strong correlation between b and $S_{\rm peak}$. The Spearman rank correlation coefficient is 0.761 with a chance probability of $P \sim 3.4 \times 10^{-15}$. The bursts from the October episode clearly fall outside this correlation. My results are shown in Figs. 4.7 and 4.8, respectively.

Similarly to what has been observed for SGR J0501+4516 and SGR J1550-5418 (see Lin et al., 2011; van der Horst et al., 2012, respectively), a significant anti-correlation between $E_{\rm peak}$

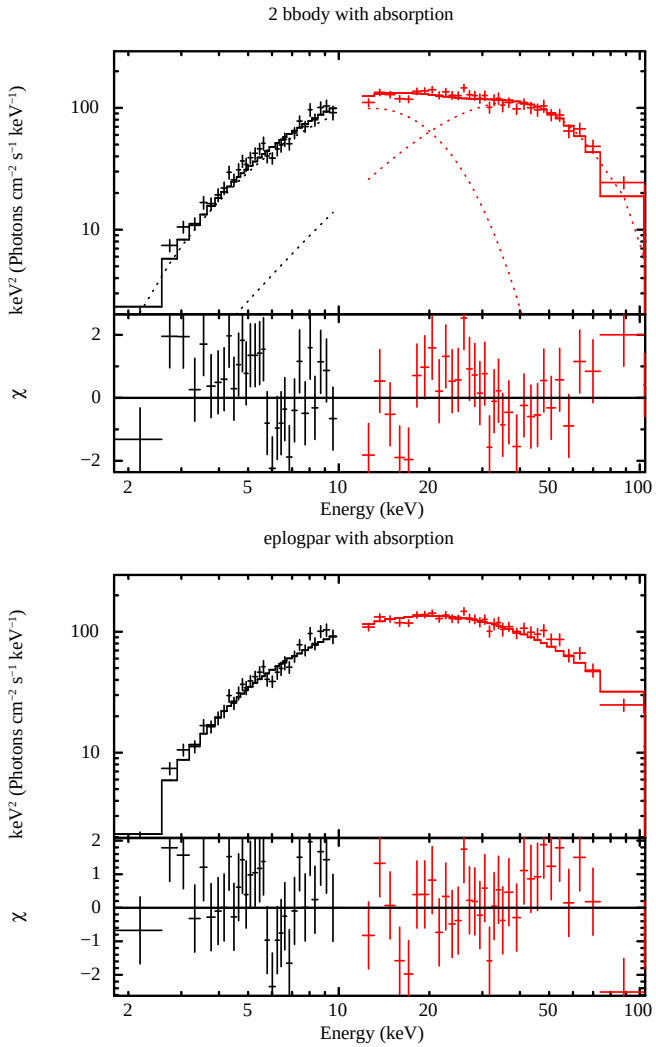

Figure 4.6 νF_ν spectra of SGR 1900+14 observed by the BeppoSAX instruments MECS and PDS (Feroci et al., 2004) fitted an LP model (lower panel).

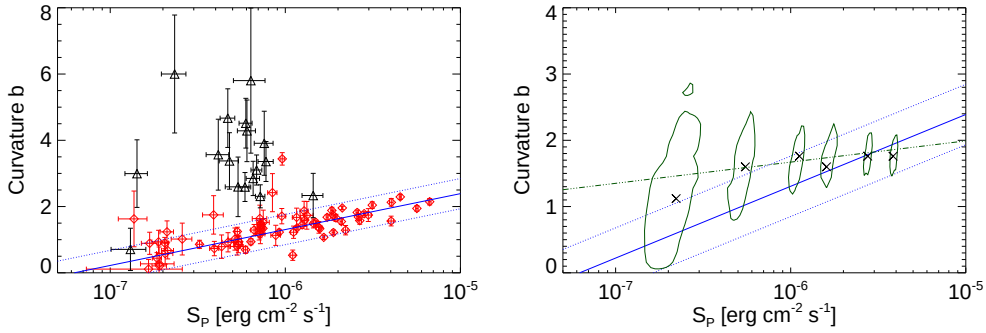

Figure 4.7 *Upper panel:* Curvature, b, vs. flux at $E_{\rm peak}$, $S_{\rm peak}$ for SGR bursts from the October (black triangles) and January, March and April period (red diamonds). A exponential fit to the latter data points (blue solid line) together with the 1σ uncertainties (blue dotted line) is indicated. *Lower panel:* The same as above without data points. The black x and green contour lines represent the reconstructed fit parameters of the simulations. The best-fit (green dash-dot-dotted line) through the reconstructed parameters is also shown. See text for details.

and $S_{\rm peak}$ is found at low $S_{\rm peak}$ values (see Fig. 4.8). Fitting the data with a single power law resulted in a power law index of -0.28. A Spearman rank correlation test results in a correlation coefficient of $\rho = -0.5$ and a chance probability of $\sim 10^{-5}$. Fitting the events with a broken power-law yielded a break at $S_{\rm p} \sim 4 \times 10^{-7}$ erg cm^{-2} s^{-1} and $E_{\rm peak} \sim 27$ keV. The power-law index before (after) the break is -2.76 (0.006). I note that this index is steeper than the one reported by van der Horst et al. (2012). However, in the analysis presented here $S_{\rm peak}$ has been used whereas the integrated average model flux was used in van der Horst et al. Performing two Spearman rank correlation tests, one before and one after the break, gives $\rho = -0.32$ and $\rho = -0.31$ with a chance probability of $P = 0.29$ and $P = 0.02$, respectively.

To rule out the possibility that the observed correlations between b and $S_{\rm peak}$ is due to instrumental effects, I performed several Monte Carlo simulations as described in the following: I used 6 different spectral models $E_{\rm peak} = 39$ keV and $b = 1.93$ but with varying $S_{\rm peak}$ values of 0.23, 0.58, 1.17, 1.75, 2.92 and 4.08 $\times 10^{-6}$ erg cm^{-2} s^{-1}, respectively. For each model, I created 1000 SGR bursts to account for Poissonian noise. This results in 6000 spectra, each of which was then fitted with the LP. The contour lines in the lower panel of Fig. 4.7 represent the 1σ area of reconstructed fit parameters of all the 6 input spectra used for the simulation. As can be seen, the lower the flux the higher the uncertainty in reproducing the input spectral parameters. The general trend is that the value of the curvature gets smaller for lower fluxes in the reconstructed events. This is also expressed and best seen by the best fit through the reconstructed fit parameters (see Fig. 4.7).

I showed that the instrumental effects can indeed affect the observed correlation between b and $S_{\rm peak}$. However, they cannot fully account for the observed trend because they are considerably shallower than the correlation of the actual data.

4.2.3 Conclusions

In this chapter, I have shown that the LP model, except for emission episode I, can fit SGR spectra over 2 decades of energy at least as good as the typical 2BB model. Even though second order Fermi acceleration acts as the underlying physical mechanism to explain its spectral shape it is, currently, only a *phenomenological* description of the SGR bursts observed by GBM. At

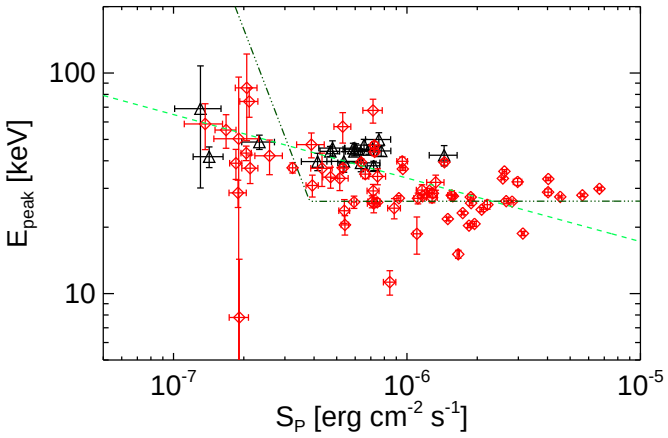

Figure 4.8 $E_{\rm peak}$ vs. $S_{\rm peak}$ for SGR bursts from the October (black triangles) and January, March and April period (red diamonds). A (broken) power-law fit to the full data sample is indicated as (dash-dot-dotted) dashed line.

the moment, it is unclear how the aforementioned physical process can arise in the classical "magnetar" framework proposed by Thompson and Duncan. However, the statistical results of the analysis presented here and the observed correlation between the curvature and $S_{\rm peak}$ is certainly intriguing and motivates a more dedicated theoretical analysis of the observational results presented in this chapter.

Chapter 5

Summary

Since its launch in 2008, the GBM collected an enormous amount of data of many astrophysical sources, such as GRBs, solar flares, SGRs, TGFs, etc. In this thesis, I have given a small overview on the capabilities of GBM, highlighting several results I obtained during my time as PhD student at MPE. I am confident that the GBM will play an important role in high-energy astrophysics in the years still to come. Together with the LAT and its broad range in energy coverage, there is no doubt that it will help us increase our understanding of the "violent Universe".

5.1 Gamma-Ray Bursts

a) The GBM is a key instrument to study the temporal and spectral properties of GRBs. One of the many interesting GRBs that have been observed by GBM was GRB 0910124, a very long burst where optical data was acquired well during its active phase by several telescopes. Using these data from the literature, I observed the optical flash due to the reverse shock. I determined the Lorentz factor to be $\Gamma_0 \approx 120$ which is perfectly consistent with Lorentz factors of other long bursts.

b) The GBM is a perfect tool to study the physical properties of GRBs in their rest-frame. I presented such a study for 47 GBM observed GRBs, focusing on both the temporal and spectral properties, as well as on intra-parameter relations within these quantities. In addition, I investigated for possible biases in the $E_{\rm peak}$ distribution of the full GBM-GRB sample, finding that (i) GBM can reliably measure $E_{\rm peak}$ down to ~ 15 keV, (ii) there is no population of high-$E_{\rm peak}$ GRBs and (iii) the width of the $E_{\rm p,rest}$ distribution is not zero. Moreover, I showed the distributions of $E_{\rm p,rest}$ and $T_{90,\rm rest}$, together with their dependence on redshift. While there is no clear trend visible for a $T_{90,\rm rest}$ evolution, there might be a positive correlation for the $E_{\rm p,rest}$ of long GRBs with redshift. However, selection and instrumental effects might play an important role for the latter correlation.

   The Amati and Yonetoku relation were confirmed. For the former, however, I find that the extrinsic scatter around the best fit is considerably larger than what is observed in the literature.

c) I found 17 untriggered *Swift* GRBs in the continuous GBM data. A spectral analysis of all these long GRBs was performed which does not reveal fundamental differences or peculiarities compared to the full GBM-GRB sample. The identified GRBs are soft, i.e.

they have low $E_{\rm peak}$ values, and are located at the lower end of the photon flux distribution. A rule-of-thumb estimate shows that the GBM on-board trigger algorithm misses ~ 1.6 GRBs per month.

Outlook

Although predicted by the GRB fireball model, GRBs with an optical flash are rare events. GBM, in joint collaboration with ground-based telescopes, offers a great potential to discover more of these elusive events. Currently, major efforts are underway to improve the GBM localization and to send them out even faster so that afterglow observations can begin as early as possible. More recently, GBM observed GRB 120711A which is yet another burst where optical observations started within 37 s after the GBM trigger. Similarly to GRB 091024A, this GRB has a precursor and shows compelling signatures of an optical flash and will be analyzed in much detail in the forthcoming months. A provocative, but yet unproven, idea was brought forward regarding GRB 091024A: the first optical peak in the light curve might actually have been induced by the forward shock of the precursor, arguing against the reverse shock scenario. This claim, however, needs more GRBs with precursors and optical observations to be verified or falsified.

Furthermore, with the increasing number of GRBs with measured redshifts we will get a better chance to identify whether GRBs are harder, i.e. have a larger intrinsic $E_{\rm p,rest}$, than GRBs at lower redshifts. If the $E_{\rm p,rest}$-z correlation would be indeed confirmed it would provide significant insights on the progenitors, the emission mechanisms and radiation properties of the prompt γ-ray emission.

The untriggered search algorithm which has only been applied to known *Swift* GRBs so far, will be used to look for the postulated population of low-luminosity (LL) GRBs. If such LL-GRBs are indeed found, their fundamental properties will be identified and compared to the general sample of the canonical long and short GRBs. In addition, the untriggered search might be helpful identifying potential γ-ray counterparts to future, however not yet observed, non-electromagnetic signals, such as e.g. gravitational waves in LIGO or neutrinos in IceCube.

5.2 Solar flares

a) In Chapter 3, I have analyzed light curves of five solar flares observed by both GBM and RHESSI, testing the data for the presence and significance of QPPs accounting for the overall shape of the PSD by applying the method introduced by Vaughan (2005). Applying this latter method to four solar flares observed by GBM and one solar flare observed by RHESSI where QPPs have been claimed in the literature, I found no statistically significant ($> 3\sigma$) results.

b) In addition, I presented a new method, called SOBER^2 (Solar Background Employing Relative Rates), for background estimation in GBM in Chapter 3.3. This new procedure is especially useful when the observed astrophysical event is of long duration and/or difficult to discern from the background. The SOBER^2 method uses the count rate of the source-occulted BGO detector as an *a priori* information which is in turn used to get a background model for the source-facing BGO detector. I have applied this method in estimating the background rate for an X1 class solar flare observed by GBM on March 2012.

Outlook

The thorough red-noise analysis of solar flare light curves in this thesis has shown that the complex physical mechanisms which have been put forward to explain the QPP behavior are not needed for most solar flares as they are, simply put, an artifact of a statistically poor data analysis. Whether or not some solar flares do indeed show significant (quasi periodic) pulsations needs to be verified using the proper statistical tools. GBM observed hundreds of solar flares whose light curves provide an immense wealth of data which can and should be tested for intriguing periodic signals.

The newly developed SOBER^2 background estimation method will be tested and applied to energetic solar flares visible in the GBM BGO detectors to identify its advantages but also potential drawbacks compared to the standard background subtraction routine.

5.3 Soft Gamma Repeaters

In Chapter 4, I proposed an alternative model to describe the γ-ray spectra of SGR bursts: the log-parabolic function. This model has two main advantages, being statistically preferred over the more complex double-blackbody which currently is the preferred function in modeling SGR burst spectra. The log-parabolic function yields fits which are at least as good as the double-blackbody fits but it has one free parameter less. Second, similarly to the double-blackbody model, it has a strong underlying physical interpretation as this model is directly related to the solution of the kinetic equation for the particles accelerated by Fermi mechanisms when the random acceleration is also taken into account with all the other terms.

I applied the log-parabolic function to busts from SGR J1550-5418 as observed by GBM and to SGR 1900+14 as observed by BeppoSAX and showed that this model fits γ-ray SGR burst SEDs at least as well as the other models which are currently applied to such data. In addition, I found a strong correlation between $S_{\rm peak}$ and b for two emission epochs of SGR J1550-5418.

Outlook

While the LP model itself is motivated by a physical mechanism, it still needs to be put into context with respect to the known properties of SGRs and magnetars to explain how the log-parabolic spectral shape can arise at the surface or magnetosphere of the SGRs. Together with the GBM "magnetar team", I am currently investigating how the LP model and its physical rationale can fit in the "magnetar" framework. This work will be published in a forthcoming paper.

Bibliography

Abdo, A. A., Ackermann, M., Ajello, M., et al.: 2009a, *ApJL* **706**, L138

Abdo, A. A., Ackermann, M., Arimoto, M., et al.: 2009b, *Science* **323**, 1688

Ackermann, M., Ajello, M., Allafort, A., et al.: 2012, *ApJ* **745**, 144

Ackermann, M., Ajello, M., Asano, K., et al.: 2011, *ApJ* **729**, 114

Ackermann, M., Asano, K., Atwood, W. B., et al.: 2010, *ApJ* **716**, 1178

Akerlof, C., Balsano, R., Barthelmy, S., et al.: 1999, *Nature* **398**, 400

Amati, L.: 2010, *arXiv 1002.2232*

Amati, L., Frontera, F., Tavani, M., et al.: 2002, *A&A* **390**, 81

Amati, L., Guidorzi, C., Frontera, F., et al.: 2008, *MNRAS* **391**, 577

Arnaud, K., Smith, R., and Siemiginowska, A.: 2011, *Handbook of X-ray Astronomy*, Cambridge University Press

Atteia, J.-L., Boer, M., Hurley, K., et al.: 1987, *ApJL* **320**, L105

Atwood, W. B., Abdo, A. A., Ackermann, M., et al.: 2009, *ApJ* **697**, 1071

Band, D., Matteson, J., Ford, L., et al.: 1993, *ApJ* **413**, 281

Barraud, C., Olive, J., Lestrade, J. P., et al.: 2003, *A&A* **400**, 1021

Bennett, C. L., Hill, R. S., Hinshaw, G., et al.: 2003, *ApJS* **148**, 97

Benz, A. (ed.): 2002, *Plasma Astrophysics, second edition*, Vol. 279 of *Astrophysics and Space Science Library*

Beuermann, K., Hessman, F. V., Reinsch, K., et al.: 1999, *A&A* **352**, L26

Bissaldi, E. and Connaughton, V.: 2009, *GCN* **70**, 1

Bissaldi, E., von Kienlin, A., Kouveliotou, C., et al.: 2011, *arXiv 1101.3325*

Bissaldi, E., von Kienlin, A., Lichti, G., et al.: 2009, *Experimental Astronomy* **24**, 47

Boella, G., Butler, R. C., Perola, G. C., et al.: 1997, *A&AS* **122**, 299

Bouvier, A., McEnery, J., Chiang, J., et al.: 2009, *GCN* **114**, 1

Brainerd, J. J., Pendleton, G. N., Mallozzi, R. S., et al.: 2000, in R. M. Kippen, R. S. Mallozzi, & G. J. Fishman (ed.), *Gamma-ray Bursts, 5th Huntsville Symposium*, Vol. 526 of *American Institute of Physics Conference Series*, pp 150–154

Briggs, M. S., Connaughton, V., Wilson-Hodge, C., et al.: 2011, *GeoRL* **38**, 2808

Browning, R., Ramsden, D., and Wright, P. J.: 1971, in *International Cosmic Ray Conference*, Vol. 1 of *International Cosmic Ray Conference*, p. 63

Burlon, D., Ghirlanda, G., Ghisellini, G., et al.: 2008, *ApJL* **685**, L19

Burrows, D. N., Hill, J. E., Nousek, J. A., et al.: 2005, *Space Sci. Rev.* **120**, 165

Butler, N. R., Bloom, J. S., and Poznanski, D.: 2010, *ApJ* **711**, 495

Butler, N. R., Kocevski, D., Bloom, J. S., and Curtis, J. L.: 2007, *ApJ* **671**, 656

Campana, R., Massaro, E., Mineo, T., and Cusumano, G.: 2009, *A&A* **499**, 847

Campana, S., Mangano, V., Blustin, A. J., et al.: 2006, *Nature* **442**, 1008

Cano, Z., Guidorzi, C., Mundell, C. G., et al.: 2009, *GCN* **66**, 1

Carrington, R. C.: 1859, *MNRAS* **20**, 13

Cenko, S. B., Butler, N. R., Ofek, E. O., et al.: 2010, *AJ* **140**, 224

Cenko, S. B., Kasliwal, M. M., and Kulkarni, S. R.: 2009, *GCN* **93**, 1

Chupp, E. L., Forrest, D. J., Higbie, P. R., et al.: 1973, *Nature* **241**, 333

Collazzi, A. C., Schaefer, B. E., and Moree, J. A.: 2011, *ApJ* **729**, 89

Crider, A., Liang, E. P., Smith, I. A., et al.: 1997, *ApJL* **479**, L39+

Cucchiara, A., Fox, D., and Tanvir, N.: 2009, *GCN* **65**, 1

Daigne, F., Rossi, E. M., and Mochkovitch, R.: 2006, *MNRAS* **372**, 1034

de Luca, A., Esposito, P., Israel, G. L., et al.: 2010, *MNRAS* **402**, 1870

Deeter, J. E. and Boynton, P. E.: 1982, *ApJ* **261**, 337

Dellinger, J. H.: 1935, *Physical Review* **48**, 705

Eichler, D., Livio, M., Piran, T., and Schramm, D. N.: 1989, *Nature* **340**, 126

Esposito, P., Mereghetti, S., Tiengo, A., et al.: 2007, *A&A* **476**, 321

Evans, P. A., Beardmore, A. P., Page, K. L., et al.: 2007, *A&A* **469**, 379

Evans, P. A., Beardmore, A. P., Page, K. L., et al.: 2009, *MNRAS* **397**, 1177

Fenimore, E. E. and Ramirez-Ruiz, E.: 2000

Feroci, M., Caliandro, G. A., Massaro, E., et al.: 2004, *ApJ* **612**, 408

Firmani, C., Avila-Reese, V., Ghisellini, G., and Ghirlanda, G.: 2006, *MNRAS* **372**, L28

Fishman, G. J., Bhat, P. N., Mallozzi, R., et al.: 1994, *Science* **264**, 1313

Fitzpatrick, G., Connaughton, V., McBreen, S., and Tierney, D.: 2011, *arXiv 1111.3779*

Foley, S., McGlynn, S., Hanlon, L., McBreen, S., and McBreen, B.: 2008, *A&A* **484**, 143

Ford, L. A., Band, D. L., Matteson, J. L., et al.: 1995, *ApJ* **439**, 307

Foullon, C., Fletcher, L., Hannah, I. G., et al.: 2010, *ApJ* **719**, 151

Foullon, C., Verwichte, E., Nakariakov, V. M., and Fletcher, L.: 2005, *A&A* **440**, L59

Friedman, H., Lichtman, S. W., and Byram, E. T.: 1951, *Physical Review* **83**, 1025

Galama, T. J., Vreeswijk, P. M., van Paradijs, J., et al.: 1998, *Nature* **395**, 670

Gehrels, N., Chincarini, G., Giommi, P., et al.: 2004, *ApJ* **611**, 1005

Ghirlanda, G., Ghisellini, G., and Lazzati, D.: 2004, *ApJ* **616**, 331

Ghirlanda, G., Nava, L., and Ghisellini, G.: 2010, *A&A* **511**, A43+

Ghirlanda, G., Nava, L., Ghisellini, G., Celotti, A., and Firmani, C.: 2009, *A&A* **496**, 585

Giblin, T. W., Connaughton, V., van Paradijs, J., et al.: 2002, *ApJ* **570**, 573

Goldstein, A., Burgess, J. M., Preece, R. D., et al.: 2012, *ApJS* **199**, 19

Golenetskii, S., Aptekar, R., Mazets, E., et al.: 2009, *GCN* **83**, 1

Goodman, J.: 1986, *ApJL* **308**, L47

Götz, D., Mereghetti, S., von Kienlin, A., and Beck, M.: 2009, *GCN* **9649**, 1

Göğüş, E., Güver, T., Özel, F., et al.: 2011, *ApJ* **728**, 160

Greiner, J.: 2011, *arXiv 1102.0472*

Grigis, P. C. and Benz, A. O.: 2008, *ApJ* **683**, 1180

Groth, E. J.: 1975, *ApJS* **29**, 453

Gruber, D. and for the Fermi/GBM collaboration: 2012a, *arXiv 1207.4620*

Gruber, D. and for the Fermi/GBM collaboration: 2012b, *arXiv 1207.4622*

Gruber, D., Greiner, J., von Kienlin, A., et al.: 2011a, *A&A* **531**, A20

Gruber, D., Krühler, T., Foley, S., et al.: 2011b, *A&A* **528**, A15+

Gruber, D., Lachowicz, P., Bissaldi, E., et al.: 2011c, *A&A* **533**, A61

Hafizi, M. and Mochkovitch, R.: 2007, *A&A* **465**, 67

Hakkila, J., Giblin, T. W., Norris, J. P., and others.: 2008, *ApJL* **677**, L81

Hakkila, J., Giblin, T. W., Young, K. C., et al.: 2007, *ApJS* **169**, 62

Heise, J. and in 't Zand, J.: 2001, *arXiv 0112353*

Henden, A., Gross, J., Denny, B., Terrell, D., and Cooney, W.: 2009, *GCN* **73**, 1

Hey, J. S., Parsons, S. J., and Phillips, J. W.: 1948, *MNRAS* **108**, 354

Inglis, A. R. and Nakariakov, V. M.: 2009, *A&A* **493**, 259

Inglis, A. R., Nakariakov, V. M., and Melnikov, V. F.: 2008, *A&A* **487**, 1147

Ioka, K. and Nakamura, T.: 2001, *ApJL* **554**, L163

Israel, G. L. and Stella, L.: 1996, *ApJ* **468**, 369

Iwakiri, W., Ohno, M., Kamae, T., et al.: 2010, in N. Kawai & S. Nagataki (ed.), *American Institute of Physics Conference Series*, Vol. 1279 of *American Institute of Physics Conference Series*, pp 89–92

Kaneko, Y., Göğüş, E., Kouveliotou, C., et al.: 2010, *ApJ* **710**, 1335

Kaneko, Y., Preece, R. D., Briggs, M. S., et al.: 2006, *ApJS* **166**, 298

Kardashev, N. S.: 1962, *Soviet Astronomy* **6**, 317

Kippen, R. M., in't Zand, J. J. M., Woods, P. M., et al.: 2004, in E. Fenimore & M. Galassi (ed.), *Gamma-Ray Bursts: 30 Years of Discovery*, Vol. 727 of *American Institute of Physics Conference Series*, pp 119–122

Klebesadel, R. W., Strong, I. B., and Olson, R. A.: 1973, *ApJL* **182**, L85+

Kliem, B., Karlický, M., and Benz, A. O.: 2000, *A&A* **360**, 715

Kniffen, D. A. and Fichtel, C. E.: 1970, *ApJL* **161**, L157

Kobayashi, S.: 2000, *ApJ* **545**, 807

Kocevski, D. and Liang, E.: 2003, *ApJ* **594**, 385

Kocevski, D. and Petrosian, V.: 2011, *arXiv 1110.6175*

Kodama, Y., Yonetoku, D., Murakami, T., et al.: 2008, *MNRAS* **391**, L1

Kouveliotou, C., Dieters, S., Strohmayer, T., et al.: 1998, *Nature* **393**, 235

Kouveliotou, C., Meegan, C. A., Fishman, G. J., et al.: 1993, *ApJL* **413**, L101

Kraushaar, W. L., Clark, G. W., Garmire, G. P., et al.: 1972, *ApJ* **177**, 341

Krühler, T., Greiner, J., Afonso, P., et al.: 2009a, *A&A* **508**, 593

Krühler, T., Greiner, J., McBreen, S., et al.: 2009b, *ApJ* **697**, 758

Kumar, P. and Piran, T.: 2000, *ApJ* **535**, 152

Lachowicz, P., Gupta, A. C., Gaur, H., and Wiita, P. J.: 2009, *A&A* **506**, L17

Laros, J. G., Fenimore, E. E., Fikani, M. M., et al.: 1986, *Nature* **322**, 152

Lawrence, A., Watson, M. G., Pounds, K. A., and Elvis, M.: 1987, *Nature* **325**, 694

Li, Y. P. and Gan, W. Q.: 2008, *Solar Physics* **247**, 77

Lin, L., Gogus, E., Baring, M. G., et al.: 2012, *arXiv 1207.1434*

Lin, L., Kouveliotou, C., Baring, M. G., et al.: 2011, *ApJ* **739**, 87

Lin, R. P., Dennis, B. R., Hurford, G. J., et al.: 2002, *Solar Physics* **210**, 3

Lithwick, Y. and Sari, R.: 2001, *ApJ* **555**, 540

Lloyd, N. M. and Petrosian, V.: 2000, *ApJ* **543**, 722

Lloyd-Ronning, N. M. and Petrosian, V.: 2002, *ApJ* **565**, 182

Lomb, N. R.: 1976, *Astrophysics and Space Science* **39**, 447

MacFadyen, A. I. and Woosley, S. E.: 1999, *ApJ* **524**, 262

Malesani, D., Tagliaferri, G., Chincarini, G., and others.: 2004, *ApJL* **609**, L5

Mandelbrot, B. B. and Wallis, J. R.: 1969, *Water Resources Research 5* **1**, 228

Markowitz, A., Edelson, R., Vaughan, S., et al.: 2003, *ApJ* **593**, 96

Markwardt, C. B., Barthelmy, S. D., Baumgartner, W. H., et al.: 2010, *GCN* 1111

Markwardt, C. B., Gavriil, F. P., Palmer, D. M., et al.: 2009, *GCN* **9645**, 1

Marshall, F. E., Baumgartner, W. H., Beardmore, A. P., and others.: 2009, *GCN* **62**, 1

Maselli, A. and Massaro, E.: 2009, *Astronomische Nachrichten* **330**, 295

Massaro, E., Tramacere, A., Perri, M., et al.: 2006, *A&A* **448**, 861

Massaro, F. and Grindlay, J. E.: 2011, *ApJL* **727**, L1

Massaro, F., Grindlay, J. E., and Paggi, A.: 2010, *ApJL* **714**, L299

Massaro, F., Paggi, A., Elvis, M., and Cavaliere, A.: 2011, *ApJ* **739**, 73

Massaro, F., Tramacere, A., Cavaliere, A., et al.: 2008, *A&A* **478**, 395

Mazets, E. P., Golentskii, S. V., Ilinskii, V. N., et al.: 1979, *Nature* **282**, 587

Medvedev, M. V. and Loeb, A.: 1999, *ApJ* **526**, 697

Meegan, C., Lichti, G., Bhat, P. N., et al.: 2009, *ApJ* **702**, 791

Meegan, C. A., Fishman, G. J., Wilson, R. B., et al.: 1992, *Nature* **355**, 143

Mereghetti, S.: 2008, *A&AR* **15**, 225

Mereghetti, S., Esposito, P., Tiengo, A., et al.: 2006, *ApJ* **653**, 1423

Mereghetti, S., Götz, D., von Kienlin, A., et al.: 2005, *ApJL* **624**, L105

Mereghetti, S., Götz, D., Weidenspointner, G., et al.: 2009, *ApJL* **696**, L74

Mereghetti, S. and Stella, L.: 1995, *ApJL* **442**, L17

Mészáros, P.: 2006, *Rep. Prog. Phys.* **69**, 2259

Meszaros, P., Laguna, P., and Rees, M. J.: 1993, *ApJ* **415**, 181

Meszaros, P. and Rees, M. J.: 1992, *ApJ* **397**, 570

Meszaros, P. and Rees, M. J.: 1993, *ApJ* **405**, 278

Meszaros, P. and Rees, M. J.: 1997, *ApJL* **482**, L29+

Mochkovitch, R., Hafizi, M., and Boci, S.: 2008, in M. Galassi, D. Palmer, & E. Fenimore (ed.), *American Institute of Physics Conference Series*, Vol. 1000 of *American Institute of Physics Conference Series*, pp 365–368

Molinari, E., Vergani, S. D., Malesani, D., et al.: 2007, *A&A* **469**, L13

Morris, D. C., Beardmore, A. P., Evans, P. A., et al.: 2009, *GCN* **9625**, 1

Nakagawa, Y. E., Yoshida, A., Hurley, K., et al.: 2007, *PASJ* **59**, 653

Nakariakov, V. M., Foullon, C., Myagkova, I. N., and Inglis, A. R.: 2010a, *ApJL* **708**, L47

Nakariakov, V. M., Foullon, C., Verwichte, E., and Young, N. P.: 2006, *A&A* **452**, 343

Nakariakov, V. M., Inglis, A. R., Zimovets, I. V., et al.: 2010b, *Plasma Physics and Controlled Fusion* **52(12)**, 124009

Nakariakov, V. M. and Melnikov, V. F.: 2009, *Space Science Reviews* **149**, 119

Nava, L., Ghirlanda, G., Ghisellini, G., and Celotti, A.: 2010, *arXiv 1012.3968*

Nicastro, L., in't Zand, J. J. M., Amati, L., et al.: 2004, *A&A* **427**, 445

Norris, J. P. and Bonnell, J. T.: 2006, *ApJ* **643**, 266

Norris, J. P., Marani, G. F., and Bonnell, J. T.: 2000, *ApJ* **534**, 248

Oates, S. R., Page, M. J., Schady, P., et al.: 2009, *MNRAS* **395**, 490

Ofman, L. and Sui, L.: 2006, *ApJL* **644**, L149

Ohno, M., Iwakiri, W., Suzuki, M., et al.: 2009, *GCN* **9653**, 1

Olive, J.-F., Hurley, K., Sakamoto, T., et al.: 2004, *ApJ* **616**, 1148

Paciesas, W. S., Meegan, C. A., von Kienlin, A., et al.: 2012, *ApJS* **199**, 18

Page, K. L. and Marshall, F. E.: 2009, *GCN* **69**, 1

Page, K. L., Willingale, R., Osborne, J. P., et al.: 2007, *ApJ* **663**, 1125

Paggi, A., Massaro, F., Vittorini, V., et al.: 2009, *A&A* **504**, 821

Pal'Shin, V., Aptekar, R., Frederiks, D., et al.: 2008, in M. Galassi, D. Palmer, & E. Fenimore (ed.), *American Institute of Physics Conference Series*, Vol. 1000 of *American Institute of Physics Conference Series*, pp 117–120

Panaitescu, A. and Kumar, P.: 2000, *ApJ* **543**, 66

Panaitescu, A. and Vestrand, W. T.: 2008, *MNRAS* **387**, 497

Parks, G. K. and Winckler, J. R.: 1969, *ApJL* **155**, L117+

Pélangeon, A., Atteia, J., Nakagawa, Y. E., et al.: 2008, *A&A* **491**, 157

Peterson, L. E. and Winckler, J. R.: 1959, *Journal of Geophysical Research* **64**, 697

Piran, T.: 1999, *Physics Reports* **314**, 575

Preece, R. D., Briggs, M. S., Mallozzi, R. S., et al.: 1998, *ApJL* **506**, L23

Press, W. H.: 1978, *Comments on Astrophysics* **7**, 103

Press, W. H. and Rybicki, G. B.: 1989, *ApJ* **338**, 277

Racusin, J. L., Karpov, S. V., Sokolowski, M., et al.: 2008, *Nature* **455**, 183

Rees, M. J. and Meszaros, P.: 1992, *MNRAS* **258**, 41P

Rees, M. J. and Meszaros, P.: 1998, *ApJL* **496**, L1+

Reznikova, V. E. and Shibasaki, K.: 2011, *A&A* **525**, A112+

Rowlinson, A., Wiersema, K., Levan, A. J., et al.: 2010, *MNRAS* **408**, 383

Sakamoto, T., Lamb, D. Q., Kawai, N., et al.: 2005, *ApJ* **629**, 311

Sakamoto, T., Sato, G., Barbier, L., et al.: 2009, *ApJ* **693**, 922

Salmonson, J. D.: 2000, *ApJL* **544**, L115

Salvaterra, R. and Chincarini, G.: 2007, *ApJL* **656**, L49

Salvaterra, R., Guidorzi, C., Campana, S., et al.: 2009, *MNRAS* **396**, 299

Sari, R. and Piran, T.: 1999a, *ApJL* **517**, L109

Sari, R. and Piran, T.: 1999b, *ApJ* **520**, 641

Scargle, J. D.: 1982, *ApJ* **263**, 835

Schaefer, B. E.: 2003, *ApJL* **583**, L71

Schuster, A.: 1898, *Journal of Geophysical Research* **3**, 13

Schwartz, R. A., Dennis, B. R., Fishman, G. J., et al.: 1992, in C. R. Shrader, N. Gehrels, and B. Dennis (eds.), *NASA Conference Publication*, Vol. 3137 of *NASA Conference Publication*, pp 457–468

Shao, L. and Dai, Z. G.: 2005, *ApJ* **633**, 1027

Spergel, D. N., Verde, L., Peiris, H. V., et al.: 2003, *ApJS* **148**, 175

Stawarz, Ł. and Petrosian, V.: 2008, *ApJ* **681**, 1725

Tavani, M., Barbiellini, G., Argan, A., et al.: 2008, *Nuclear Instruments and Methods in Physics Research A* **588**, 52

Thompson, C. and Duncan, R. C.: 1995, *MNRAS* **275**, 255

Thompson, C. and Duncan, R. C.: 1996, *ApJ* **473**, 322

Timmer, J. and Koenig, M.: 1995, *A&A* **300**, 707

Tramacere, A., Giommi, P., Massaro, E., et al.: 2007, *A&A* **467**, 501

Tramacere, A., Giommi, P., Perri, M., et al.: 2009, *A&A* **501**, 879

Tramacere, A., Massaro, E., and Taylor, A. M.: 2011, *ApJ* **739**, 66

Ukwatta, T. N., Dhuga, K. S., Parke, W. C., et al.: 2009, *arXiv 0906.3193*

Ukwatta, T. N., Stamatikos, M., Dhuga, K. S., et al.: 2010, *ApJ* **711**, 1073

Updike, A. C., Hartmann, D. H., Milne, P. A., et al.: 2009, *GCN* **74**, 1

van der Horst, A. J., Kouveliotou, C., Gorgone, N. M., et al.: 2012, *arXiv 1202.3157*

van Paradijs, J., Groot, P. J., Galama, T., et al.: 1997, *Nature* **386**, 686

Vaughan, S.: 2005, *A&A* **431**, 391

Vedrenne, G., Roques, J.-P., Schönfelder, V., et al.: 2003, *A&A* **411**, L63

Vestrand, W. T., Wozniak, P. R., Wren, J. A., et al.: 2005, *Nature* **435**, 178

Virgili, F., Qin, Y., Zhang, B., and Liang, E.: 2011, *arXiv 1112.4363*

Vogel, M.: 2012, *Contemporary Physics* **53**, 71

von Kienlin, A., Gruber, D., Kouveliotou, C., et al.: 2012, *arXiv 1206.4915*

Wang, F. Y. and Dai, Z. G.: 2011, *ApJL* **727**, L34+

Waxman, E.: 1997, *ApJL* **489**, L33+

Wilson-Hodge, C. A., Case, G. L., Cherry, M. L., et al.: 2012, *arXiv 1201.3585*

Winkler, C., Courvoisier, T. J.-L., Di Cocco, G., and others.: 2003, *A&A* **411**, L1

Yonetoku, D., Murakami, T., Nakamura, T., et al.: 2004, *ApJ* **609**, 935

Zaitsev, V. V. and Stepanov, A. V.: 1982, *Soviet Astronomy Letters* **8**, 132

Zhang, B., Fan, Y. Z., Dyks, J., Kobayashi, S., et al.: 2006, *ApJ* **642**, 354

Zhang, B. and Mészáros, P.: 2002, *ApJ* **581**, 1236

Zhang, B., Zhang, B., Virgili, F. J., et al.: 2009, *ApJ* **703**, 1696

Zimovets, I. V. and Struminsky, A. B.: 2010, *Solar Physics* **263**, 163

Acknowledgments

At the end of this fantastic PhD journey, I need to thank several people who contributed, be it directly or indirectly, to the completion of this work and my education.

First and foremost, I'd like to express my gratitude to my supervisor Jochen, for without him I wouldn't be the astrophysicist I am now. I thank you for the opportunity you have given me working at this institute, for your infinite patience and for always having an open ear for me. I'd also like to thank Andreas who, with his great humor and serenity, guided me through times of peril and frustration. I wish to thank both my former office colleagues, Elisabetta and Davide, for the laughs, discussions and good times we shared together in X1.3.05. It also goes without saying that the fun didn't stop in my office but was spread all across the "gamma group" floor at MPE where I shared several jokes and laughs together with Robert, Marco, Vlad, Johnny, Thomas, Karsten, Sandra and Eugenio.

As everybody knows, it is only the (lunch) breaks which make work bearable. Thank you, Sotiria, Gilles, Emmanuel, Felicia, Tomek and Rob who shared more than a few hundreds of meals with me at the IPP canteen. I am sure that every time the clock strikes 12:20 I'll be thinking about you guys.

Believe it or not, I also had a live outside work which I loved to share with my closest friends Daniel, Roland, Maria, Christoph, Boris, Kasia, Manuel, Sara and Guido. You all helped me get through these last three years. Thank you for all the fun times we shared together. I hope there are many more yet to come.

Moreover, I would like to express my sincere gratitude to my family, in particular to my parents. Thank you Monika and Eduard for always being there for me, your guidance and your financial support which you offered me throughout my life. I can never pay back what you have given me and, more importantly, made me. I am eternally grateful for having parents such as you. Thanks also to my sister, Claudia, for being there when I needed you and for fully accepting me for who I am. Lastly, I'd like to thank my uncle Klaus, aunt Renate and two grandmothers Johanna and Maria, for your encouragement, help and support.

The last but most important words go to my fiancée, Andrea, who followed me to Munich, thereby setting aside her own plans. She was always there for me when I needed her the most. Andrea, you are the joy of my life. I don't really know how to express my eternal gratitude to you in words but I thank you with all my heart! I love you.